

## **INFORMATION TO USERS**

This manuscript has been reproduced from the microfilm master. UMI films the text directly from the original or copy submitted. Thus, some thesis and dissertation copies are in typewriter face, while others may be from any type of computer printer.

**The quality of this reproduction is dependent upon the quality of the copy submitted.** Broken or indistinct print, colored or poor quality illustrations and photographs, print bleedthrough, substandard margins, and improper alignment can adversely affect reproduction.

In the unlikely event that the author did not send UMI a complete manuscript and there are missing pages, these will be noted. Also, if unauthorized copyright material had to be removed, a note will indicate the deletion.

Oversize materials (e.g., maps, drawings, charts) are reproduced by sectioning the original, beginning at the upper left-hand corner and continuing from left to right in equal sections with small overlaps.

Photographs included in the original manuscript have been reproduced xerographically in this copy. Higher quality 6" x 9" black and white photographic prints are available for any photographs or illustrations appearing in this copy for an additional charge. Contact UMI directly to order.

ProQuest Information and Learning  
300 North Zeeb Road, Ann Arbor, MI 48106-1346 USA  
800-521-0600

**UMI<sup>®</sup>**



# Space-Time-Frequency Processing for OFDM Systems in Time-Varying Channel

## DISSERTATION

Submitted in Partial Fulfillment

of the Requirements for the

Degree of

DOCTOR OF PHILOSOPHY (Electrical Engineering)

at the


POLYTECHNIC UNIVERSITY

by

BYUNG-CHUL KIM

September 2001

Approved:

  
Department Head

1/2 2002

Copy No. \_\_\_\_\_

UMI Number: 3030208

**UMI<sup>®</sup>**

---

UMI Microform 3030208

Copyright 2002 by Bell & Howell Information and Learning Company.

All rights reserved. This microform edition is protected against  
unauthorized copying under Title 17, United States Code.

---

Bell & Howell Information and Learning Company

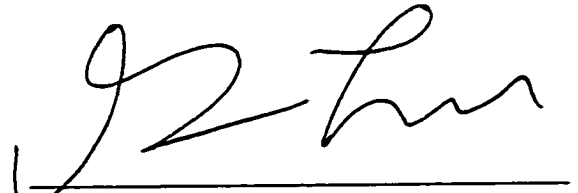
300 North Zeeb Road

P.O. Box 1346

Ann Arbor, MI 48106-1346

Approved by the Guidance Committee:

Major: Electrical Engineering



---

I-Tai Lu

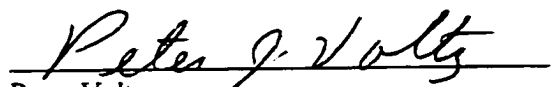
Professor of  
Electrical Engineering



---

Frank A. Cassara

Professor of  
Electrical Engineering



---

Peter Voltz

Associate Professor of  
Electrical Engineering

Minor: Computer Science

Microfilm or other copies of this dissertation are obtainable from

UNIVERSITY MICROFILMS  
300 N. Zeeb Road  
Ann Arbor, Michigan 48106

## VITA

Byung-Chul Kim was born in Taegu, Korea on March 28, 1962. He received B.E. Degree from Kyungpook National University in 1985 and M.E. Degree from Ajou University in 1987. Since 1996, he has been pursuing the Ph.D degree in Electrical Engineering at Polytechnic University, Brooklyn, New York.

From 1987 to 1996, he was a researcher, then a senior researcher in Agency for Defense Development in Chinhae, Korea, where his research efforts focused on underwater acoustic signal processing and sonar systems design. His research interests include signal processing in communications and sonar systems.

To my mother,  
my wife, my daughters,  
and  
to the memory of my father.



# Acknowledgements

First, I wish to express my deepest appreciation to my thesis advisor, Prof. I-Tai Lu, for his guidance, support and valuable advices during my graduate studies at Poly. His continued support and encouragement made this work possible. In addition, special thanks must be given to Prof. Henry L. Bertoni for his encouragement, support, and giving me the chance to assist his publication. His encouragement was the biggest help through out my study. I would like to show my appreciation to Prof. Frank A. Cassara and Prof. Peter Voltz for their useful comments on thesis work while serving on the Guidance Committee. I also wish to thank Prof. S. U. Pillai, who supported me to study the array signal processing, and introduced the systems theory.

A debt of gratitude is owed to all members of KSA, and many colleagues at Poly, who shared the grief and joy with me during my school days at Poly. I particularly thank Dr. Jeff Wang for helping me to complete this thesis. I would like to show my sincere gratitude to Dr. Jeong-Dong Ryoo who has been my best friends for more than 20 years, and introduced Polytechnic University at the first time. He never hesitated to make advice and help whenever I needed it.

Finally, my deepest thanks go to my mother, to my lovely wife and two daughters. Without their love, encouragement and constant support, this work could not be done.

## AN ABSTRACT

SPACE-TIME-FREQUENCY PROCESSING FOR  
OFDM SYSTEMS IN TIME-VARYING CHANNEL

by

Byung-Chul Kim

Advisor: I-Tai Lu

Submitted in Partial Fulfillment of the Requirements for the  
Degree of doctor of Philosophy (Electrical Engineering)

September 2001

This dissertation concerns performance improvement for OFDM communications in time-varying channel.

A signal propagating through the wireless channel usually arrives at receiver along a number of different paths, referred to as multipaths. Fast fading results from the geometry changes from transmitter to receiver in time, which is mainly due to the movement of mobile unit. Multipath propagation and fast fading result in the spreading of the signal in different dimensions. They are delay spread, Doppler spread and angular spread. These spreads have significant effects on the signal, and in most cases, they degrade the performance of conventional receivers

However, exploiting space, time and frequency dimensions simultaneously, the new

receiver processing schemes enable lower BER for communications in highly time-varying channel. The proposed schemes, so-called single summation space-time-frequency processing (STFP) and double summation STFP are introduced and their properties are analyzed and compared.

As a special case of STFP, Doppler diversity schemes are discussed especially for OFDM communications. Doppler diversity for OFDM systems can be realized in both frequency and time domain. Frequency domain approach requires less complexity than time domain approach. However, it requires accurate information on the channel. Time domain approach utilizes pilot subsymbols to estimate required signal correlations. From the correlations, optimum weights for diversity combining are computed.

Underwater acoustic (UWA) communications channel is highly time-varying. Because of the low sound velocity, the inhomogeneity of medium, reflections from surface in motion, and so on, UWA channel shows high temporal and spectral variations. Therefore, the communications in underwater is quite challenging.

In this thesis, UWA channel is modeled as a time-varying filter composed of minimum-phase systems and all-pass systems. Then, a new channel simulator based on this model is designed, and it enables realistic simulations of UWA channels. The results are compared with real data recorded at sea.

An OFDM receiver processing is developed for UWA communications. In order to combat Doppler shift and spreads, it employs Doppler estimator and compensator, and time-frequency channel estimation and equalization. Its performance is demonstrated through the sea trials.

# Contents

<b>List of Figures</b> .....	<b>xi</b>
<b>List of Tables</b> .....	<b>xiii</b>
<b>1. Channel simulation for wireless communications</b>	
1.1.Introduction .....	1
1.2.Channel Modeling .....	2
1.3.Channel Simulator .....	5
1.4.Channel Simulations for OFDM Systems .....	6
References .....	8
<b>2. A Frequency Domain Doppler Diversity for OFDM Wireless Mobile Communications</b>	
2.1.Introduction .....	9
2.2.Formulation .....	12
2.3.Simulation .....	22
2.4.Conclusions .....	25
References .....	26
<b>3. Space-Time-Frequency Processing</b>	
3.1.Introduction .....	27
3.2.Space-Time-Frequency Processing (STFP) .....	28
3.3.Simulation .....	35
3.4.Time Domain Doppler Diversity .....	46
3.5.Conclusions .....	49
References .....	50
<b>4. Underwater Acoustic Channel Simulator for Broadband Communications Systems</b>	
4.1.Introduction .....	51
4.2.Underwater Acoustic Channel Model .....	54
4.3.Implementation of Channel Response .....	59
4.4.Simulation Results .....	67
4.5.Conclusions .....	79
Appendix A Mean Doppler Frequency and RMS Doppler Spread --	80
Appendix B Instantaneous Frequency Spectrum Estimation using MVSE	82
References .....	84
<b>5. OFDM Underwater Communications Systems</b>	
5.1.Introduction .....	86
5.2.Underwater Acoustic Communications (UWA) .....	88
5.3.OFDM Systems for Underwater Communications .....	90
5.4.Simulation .....	94

5.5.Conclusions ----- 99  
References ----- 100

**6. Field Trials of OFDM Underwater Communications in Signal Ex-C and  
Signal Ex-D**

6.1.Introduction ----- 101  
6.2.Signal Ex-C ----- 103  
6.3.Signal Ex-D ----- 119  
6.4.Conclusions ----- 128  
References ----- 129

## List of Figures

1.1	Multipath environment and antenna geometry -----	2
1.2	Mean-squared error of simulator versus $F_D T$ for various FIR filter length -	7
2.1	Time varying channel responses for Doppler branches -----	10
2.2	OFDM transmitter and receiver with Doppler diversity -----	14
2.3	Power level of interference and signal component for $f_x$ -----	17
2.4	Signal to interference ratio vs $F_D T$ for 4 different $f_x$ 's -----	18
2.5	Correlation coefficients of channels and interferences -----	19
2.6	BER vs $\Delta f_x T$ for 3 branch Doppler diversity -----	20
2.7	Histograms for the center branch with $f_x = 0$ -----	23
2.8	BER versus $F_D T$ for noise-free and 15dB SNR -----	24
3.1	Block diagrams of the single-summation space-time-frequency processor-	29
3.2	Block diagrams of the double-summation space-time-frequency processor	30
3.3	OFDM symbol structure in time and frequency domain -----	35
3.4	BER versus $\Delta f_x$ for various $F_D T$ -----	37
3.5	BER for 6 STFP configurations -----	40
3.6	BER for 3 different processors at 15 dB SNR -----	41
3.7	Simulation for deriving signal to ICI power ratio -----	43
3.8	BER for 3 different double summation STFP at 15 dB SNR -----	44
3.9	BER performances for different angular spreads -----	45
3.10	Histograms for output of time domain Doppler diversity -----	47
3.11	Histograms for the desired signal and noise plus ICI for case with ( $Q=3$ ) and without ( $Q=1$ ) Doppler diversity -----	48
4.1	Underwater acoustic channel configuration -----	54
4.2	A simplified isospeed channel model -----	55
4.3	Absorption coefficient vs. frequency -----	58
4.4	Signal processing model for the channel transfer function -----	60
4.5	Observation of Doppler effects in real data -----	64
4.6	Generation of random fluctuation of time delay for the $k^{\text{th}}$ eigenray -----	65
4.7	Comparison of frequency responses between the theoretical model and the designed filter -----	66
4.8	Frequency domain representation of OFDM signal used for the sample simulation -----	68
4.9	Simulated frequency fluctuation of 4 sinusoidal components -----	69
4.10	Comparison between the random process $f_0 \xi_0(n)/c$ and the estimate of instantaneous Doppler shift $f_D$ -----	71
4.11	Power spectral densities of experimental and simulated narrowband signals	73
4.12	Comparison between theoretical values and simulation results for mean Doppler Frequency $f_{DM}$ and rms Doppler spread $B_D$ -----	74
4.13	Power spectral densities of experimental and simulated broadband signals -	75
4.14	Path delay estimation for simulated signal -----	76
4.15	PSD for 3 different sets of $\tilde{a}_k$ and $a_k$ -----	78

5.1	Block diagram of a OFDM system for underwater communications -----	89
5.2	Doppler shift estimation for simulated signal -----	96
5.3	Channel Impulse Response for Simulation -----	97
5.4	BER versus signal to noise ratio -----	98
6.1	Symbol sequence on time axis -----	104
6.2	Pilot-Subsymbol Grid -----	106
6.3	Symbols and reference tones -----	107
6.4	Source and received signal at various distances -----	108
6.5	Symbol by symbol estimation of Doppler shift for signal received at 3 km	110
6.6	Channel frequency response for 3 km -----	111
6.7	Delay profile for 3 km -----	111
6.8	Channel frequency response for 7 km -----	112
6.9	Delay profile for 7 km -----	112
6.10	Constellation of subsymbols after equalization: 3 km, $S/N \approx 20\text{dB}$ -----	114
6.11	Constellation of subsymbols after equalization: 5 km, about 15 dB -----	114
6.12	Constellation of subsymbols after equalization: 7km, about 12 dB -----	115
6.13	BER of symbols for the 3 km data -----	116
6.14	BER of symbols for the 5 km data -----	117
6.15	BER of symbols for the 7 km data -----	118
6.16	Source and received waveforms -----	120
6.17	Doppler shift estimation and compensation: $\text{SNR} = 12.3 \text{ dB}$ -----	121
6.18	Doppler shift estimation and compensation: $\text{SNR} = 14.6 \text{ dB}$ -----	122
6.19	Channel frequency response: $\text{SNR}=12.3\text{dB}$ -----	123
6.20	Delay profile corresponding to Figure 6.18 -----	123
6.21	Channel frequency response: $\text{SNR} = 14.6 \text{ dB}$ -----	124
6.22	Delay profile corresponding to Figure 6.21 -----	124
6.23	Constellation of subsymbols after equalization: 12.3 dB -----	126
6.24	Constellation of subsymbols after equalization: 14.6 dB -----	126
6.25	BER for undecoded bits for SignalEx-D -----	127

## List of Tables

2.1	Simulation setup -----	23
3.1	Simulation parameters for deriving the results in Figure 3.4 -----	36
3.2	Simulation parameters for deriving the results in Figure 3.5 -----	40
3.3	Simulation parameters for deriving the results in Figure 3.8 -----	44
3.4	Simulation parameters for deriving the results in Figure 3.10 -----	47
4.1	Simulation parameters -----	68
5.1	System specification -----	95
6.1	Signal Specifications for Signal Ex-C -----	104
6.2	Signal Specifications for SignalEx-D -----	119



# Chapter 1

## Channel Simulation for Wireless Communications

### 1.1. Introduction

In the study of communication systems, modeling of the channel is one of the most important procedures because the performance of the receiver highly depends on the characteristics of the channel. In this chapter, we will define our communication channel model and its simulation method for their usage in chapters 2 and 3 of this thesis.

The wireless communication channel model is based on the propagation of radio waves in the environment. Radio propagation in the land mobile channel is usually following multipath trajectories due to the presence of buildings, hills, automobiles and so on. Each multipath arrival is characterized by multiple reflections, diffractions, scattering and energy attenuations. In addition, when a signal is transmitted from or received by mobile in motion, the time variation of transmitter-receiver geometry causes significant fluctuations on signal strength and spectrum.

Many of channel models have been studied based on stochastic properties of the channel behavior because the environments are highly irregular and inhomogeneous with respect to the wavelength scale. A wide-sense stationary uncorrelated scattering (WSSUS) model was introduced by Bello [1] and similar stochastic models and simulation methods have been actively developed [2-4]. In the WSSUS model, scatterers are grouped into clusters in space. The delay differences within each cluster are not resolvable within the signal bandwidth. However, if there are multiple clusters and the corresponding time delays are resolvable, multipath fading occurs. This model can be simulated by a so-called fading simulator. A fading simulator can be constructed by a FIR filter whose tap gains vary in time.

A recent approach in channel modeling, referred as the basis expansion model [5], has been

developed for blind channel estimation. In this model, time varying tap-gain in fading channel model is decomposed into multiple time-varying exponential basis functions weighted with proper time-invariant coefficients. There are many other channel models. For examples, two spatial channel models have been developed for simulation purpose in GSM (Global System of Mobile communication) standard [6] [7]. The Typical Urban (TU) model is designed to have path-delay properties appropriate for large town in flat environments, while the Bad Urban (BU) model was developed to model large delay spread representing environments with large reflectors not in vicinity of the mobile.

In this chapter, we will derive a channel model similar to the GSM simulation models. Each path has its own statistically independent random amplitude, time delay, arrival angle and Doppler spread. In most cases, we consider more than 100 paths so that the resulting signal properties are similar to those of a popular fading simulator.

## 1.2. Channel Modeling

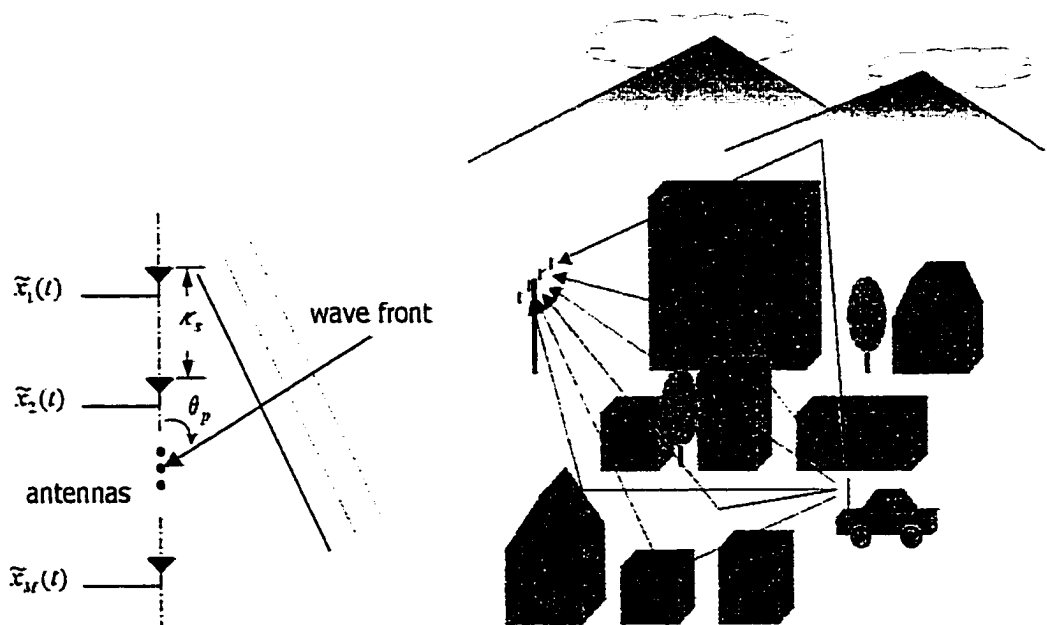


**Figure 1.1** Multipath environment and antenna geometry

A typical multipath communication environment is depicted in Figure 1.1. Multiple waves propagate independently from the transmitter to the receiver, while each of them experiences multiple reflections, diffractions, and scatterings. As mobile unit moves, each path length and the corresponding delay and phase are continuously changing. These changes cause variations of the channel response in time.

The time-varying channel impulse response for the  $m^{\text{th}}$  antenna  $\tilde{h}_m(t, \tau)$  is represented as

$$\tilde{h}_m(t, \tau) = \frac{1}{\sqrt{N_p}} \sum_{p=1}^{N_p} \tilde{a}_p \delta(\tau - \tilde{\tau}_p(t) - \xi_{p,m}) \quad (1.1)$$

where

$N_p$ : number of paths

$M$ : number of antennas

$\tilde{a}_p$ : complex path gain for the  $p^{\text{th}}$  path

$\tilde{\tau}_p(t)$ : the  $p^{\text{th}}$  time-varying path delay at the first antenna

$\xi_{p,m}$ :  $p^{\text{th}}$  path delay increment at the  $m^{\text{th}}$  antenna (with respect to the first antenna)

$\delta(\cdot)$ : Dirac delta function.

In practice, the complex path gain  $\tilde{a}_p$  is a stochastic process, since scatterers are altering as the mobile unit moves. However, since our observation interval is shorter than several symbol lengths, we may regard it as a random variable. Within a short observation time interval, the time-varying path delay  $\tilde{\tau}_p(t)$  can be described by the following linear model:

$$\tilde{\tau}_p(t) = \tau_p - \Delta_p(t - t_1) + \varepsilon_p(t) \quad (1.2)$$

where

$\tau_p$ : the  $p^{\text{th}}$  path delay at time  $t_1$

$\Delta_p$ : variation slope

$\varepsilon_p(t)$ : error in linear approximation

Time delay difference between the first antenna and the  $m^{\text{th}}$  antenna  $\xi_{p,m}$  for the  $p^{\text{th}}$  path can be expressed as

$$\xi_{p,m} = (m-1) \frac{r_1}{C} \cos \theta_p \quad (1.3)$$

where

- $\kappa_s$ : antenna spacing
- $C$ : speed of light
- $\theta_p$ : arriving angle for the  $p^{\text{th}}$  path.

We will now derive a baseband channel model suitable for wideband communications technique such as OFDM. Let  $\tilde{s}(t)$  denote the signal in transmission band with the carrier frequency  $f_c$  and  $s(t)$  be the band-limited baseband signal. Then

$$\tilde{s}(t) = e^{j2\pi f_c t} s(t) \quad (1.4)$$

$$s(t) = \sum_{k=-\infty}^{\infty} s_0(k) h_T(t - kT_s) \quad (1.5)$$

where  $h_T(t)$  is the impulse response of the bandpass filter in the transmitter, and  $s_0(k)$  is the baseband signal in the discrete time domain. If  $h_T(t)$  is an ideal band pass filter, it can be represented as

$$h_T(t) = \frac{\sin \pi t / T_s}{\pi t / T_s}. \quad (1.6)$$

where  $T_s$  is the sampling interval.

The received signal in transmission band  $\tilde{x}_m(t)$  can be expressed as the sum of thermal noise  $\tilde{v}_m(t)$  and the convolution of the transmitted signal  $\tilde{s}(t)$  with the channel impulse response:  $\tilde{h}_m(t, \tau)$

$$\begin{aligned} \tilde{x}_m(t) &= \tilde{s}(t) * \tilde{h}_m(t, \tau) + \tilde{v}_m(t) \\ &= \frac{1}{\sqrt{N_p}} \sum_{p=1}^{N_p} \tilde{\alpha}_p \tilde{s}(t - \tilde{\tau}_p(t) - \xi_{p,m}) + \tilde{v}_m(t) \\ &= \frac{1}{\sqrt{N_p}} \sum_{p=1}^{N_p} \tilde{\alpha}_p s(t - \tilde{\tau}_p(t) - \xi_{p,m}) e^{j2\pi f_c (t - \tilde{\tau}_p(t) - \xi_{p,m})} + \tilde{v}_m(t) \\ &\approx \frac{1}{\sqrt{N_p}} \sum_{p=1}^{N_p} \tilde{\alpha}_p s(t - \tau_p) e^{j2\pi f_c (t - \tau_p + \Delta_p t - \Delta_p t - \xi_{p,m})} + \tilde{v}_m(t) \\ &= \frac{1}{\sqrt{N_p}} \sum_{p=1}^{N_p} a_p s(t - \tau_p) e^{j2\pi f_c (t + \Delta_p t - \xi_{p,m})} + \tilde{v}_m(t) \end{aligned} \quad (1.7)$$

where  $a_p$  is the baseband complex path gain for the  $p^{\text{th}}$  path (including phase shift caused by

the path delay):

$$a_p = \tilde{a}_p e^{-j2\pi f_c(\tau_p + \Delta_p t)}. \quad (1.8)$$

Note that the approximation  $s(t - \tau_p + \Delta_p(t - t_1) - \varepsilon(t) - \xi_{p,m}) \approx s(t - \tau_p)$  in (1.7) is valid because delay variations are small with respect to the inverse of the bandwidth of  $s(t)$ . Moreover, for short observation intervals,  $\varepsilon(t) \ll \Delta_p(t - t_1)$  and can be neglected.

From (1.7), the received signal in baseband  $x_m(t)$  can be represented by

$$\begin{aligned} x_m(t) &= \tilde{x}_m(t) e^{-j2\pi f_c t} \\ &= \frac{1}{\sqrt{N_p}} \sum_{p=1}^{N_p} a_p s(t - \tau_p) e^{j2\pi f_c(\Delta_p t - \xi_{p,m})} + v_m(t) \\ &= \frac{1}{\sqrt{N_p}} \sum_{p=1}^{N_p} a_p s(t - \tau_p) e^{j2\pi f_c \Delta_p t} e^{-j2\pi(m-1)\frac{\kappa_x}{\lambda_c} \cos \theta_p} + v_m(t) \end{aligned} \quad (1.9)$$

where

- $\lambda_c$ : wave length of the carrier;  $\lambda_c = C / f_c$
- $f_{D_p}$ : Doppler shift for the  $p^{\text{th}}$  path;  $f_{D_p} = f_c \Delta_p$
- $v_m(t)$ : baseband additive noise at the  $m^{\text{th}}$  antenna; i.e.,  $\tilde{v}_m(t) e^{-j2\pi f_c t}$ .

Therefore, the baseband channel impulse response with respect to the  $m^{\text{th}}$  antenna  $h_m(t, \tau)$  can be expressed as

$$h_m(t, \tau) = \frac{1}{\sqrt{N_p}} \sum_{p=1}^{N_p} a_p \delta(\tau - \tau_p) e^{j2\pi f_c \Delta_p t} e^{-j2\pi(m-1)\frac{\kappa_x}{\lambda_c} \cos \theta_p}. \quad (1.10)$$

### 1.3. Channel Simulator

The continuous channel model expressed in (1.10) can be simulated in the discrete time domain to realize continuous path delays. From (1.5), (1.6) and (1.9), the baseband signal sampled at  $nT_s$ ,  $x_m(nT_s)$  is

$$\begin{aligned}
x_m(nT_s) &= \frac{1}{\sqrt{N_p}} \sum_{p=1}^{N_p} a_p s(nT_s - \tau_p) e^{j2\pi f_{Dp} nT_s} e^{-j2\pi(m-1)\frac{\kappa_s}{\lambda_c} \cos\theta_p} + v_m(nT_s) \\
&= \frac{1}{\sqrt{N_p}} \sum_{p=1}^{N_p} a_p \sum_{k=-\infty}^{\infty} s_0(k) h_T(nT_s - \tau_p - kT_s) e^{j2\pi f_{Dp} nT_s} e^{-j2\pi(m-1)\frac{\kappa_s}{\lambda_c} \cos\theta_p} + v_m(nT_s). \\
&= \frac{1}{\sqrt{N_p}} \sum_{p=1}^{N_p} a_p \sum_{k=-\infty}^{\infty} s_0(k) \frac{\sin \pi \left( n - \frac{\tau_p}{T_s} - k \right)}{\pi \left( n - \frac{\tau_p}{T_s} - k \right)} e^{j2\pi f_{Dp} nT_s} e^{-j2\pi(m-1)\frac{\kappa_s}{\lambda_c} \cos\theta_p} + v_m(nT_s)
\end{aligned} \tag{1.11}$$

The ideal lowpass filter  $h_T(t)$  of infinite length can be approximated by FIR filter with time domain windowing. Let the windowing function  $\Psi(n)$ , of which size is  $L_\Psi$ , then  $x_m(t)$  can be approximated as

$$\begin{aligned}
x_m(nT_s) &= \frac{1}{\sqrt{N_p}} \sum_{p=1}^{N_p} a_p \sum_{k=-L_\Psi/2}^{L_\Psi/2-1} s_0(k) \Psi \left( n - \frac{\tau_p}{T_s} - k \right) \frac{\sin \pi \left( n - \frac{\tau_p}{T_s} - k \right)}{\pi \left( n - \frac{\tau_p}{T_s} - k \right)} e^{j2\pi \left( f_{Dp} nT_s - (m-1)\frac{\kappa_s}{\lambda_c} \cos\theta_p \right)} \\
&\quad + v_m(nT_s)
\end{aligned} \tag{1.12}$$

The simulator derived in (1.12) is used for all wireless channel simulations in this thesis. A Hamming window of length 128 is selected for the windowing function  $\Psi(n)$ . By choosing proper distributions for complex path gains, path delays, Doppler shift and arrival angle, (1.12) can simulate most of stochastic channel models such as WSSUS models for a short duration. The required channel parameters can be obtained from either experimental data or site-specific propagation models [8].

#### 1.4. Channel Simulations for OFDM Systems

An OFDM signal is applied to the discrete channel simulator in (1.12). For three different

sizes of window functions, the mean squared errors of the frequency response of the discrete channel simulator in (1.12) versus  $F_D T$  are shown in Figure 1.2. Here, the continuous channel model in (1.10) serves as the reference.

In Figure 1.2, the mean squared error  $MSE_H$  is calculated by

$$MSE_H = \frac{1}{N_T} \sum_{i=1}^{N_T} \sum_{k=1}^N \frac{|\tilde{H}_i(k) - H_i(k)|^2}{|H_i(k)|^2} \quad (1.13)$$

where  $\tilde{H}_i(k)$  is the frequency response for the  $k^{\text{th}}$  subcarrier during the  $i^{\text{th}}$  trial,  $H_i(k)$  is the frequency response for the continuous channel model in (1.10),  $N$  is the number of subcarriers and  $N_T$  is the number of trials. In this simulation, Hamming window is selected as window function and  $N=128$ . When the window size  $L_\psi$  is 128, which is used for all simulations in this thesis, the error is well below  $10^{-5}$ .

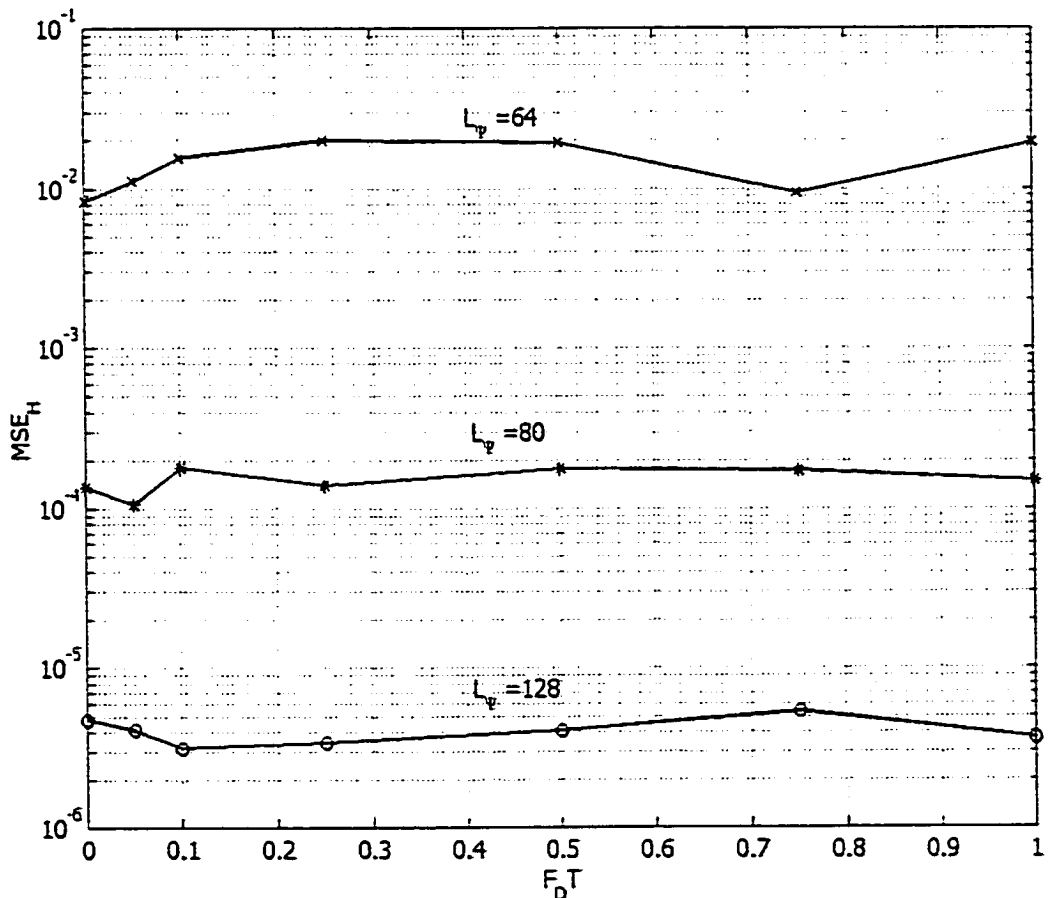


**Figure 1.2** Mean-squared error versus  $F_D T$  for various FIR filter length

## References

- [1] Philips A. Bello, "Characterization of randomly time-variant linear channels," *IEEE Trans. on Communications*, vol. COM-11, No.12, pp.360-393, December 1963.
- [2] W. C. Jakes, Jr., *Microwave Mobile Communications*, Piscataway, NJ: IEEE Press, 1974.
- [3] P. Hoehner, "A statistical discrete-time model for SWWUS multipath channels," *IEEE Trans. on Vehicular Technology*, vol. 41, pp. 461-468, November 1992.
- [4] K.W. Yip and T.S. Ng, "Efficient simulation of digital transmission over WSSUS channels," *IEEE Trans. on Communications*, vol. 43, pp.2907-2912, Dec., 1995.
- [5] Georgios B. Giannakia and Cihan Tepedelenlioglu, "Basis expansion models and diversity techniques for blind identification and equalization of time-varying channels," *Proceedings of IEEE*, vol. 86, no. 10, October 1998.
- [6] ANSI, "Personal communications services air interface specification," *J-STD-007*, 1995.
- [7] Joseph C. Liberti, Jr., and Theodore S. Rappaport, *Smart Antennas for Wireless Communications*, Upper Saddle River, NJ: Prentice Hall Inc., 1999.
- [8] Henry L. Bertoni, *Radio Propagation for Modern Wireless Systems*, Upper Saddle River, NJ: Prentice Hall Inc., 1999.



## Chapter 2

# A Frequency Domain Doppler Diversity for OFDM Wireless Mobile Communications

### 2.1. Introduction

Orthogonal frequency-division multiplexing (OFDM) is a multicarrier (MC) technique where the subcarriers are orthogonal to one another. Due to its effectiveness, efficiency and simplicity, OFDM is likely to be adopted as the 4<sup>th</sup> generation wireless communication technology. Firstly, it is an effective technique for mitigating frequency selective fading because the bandwidth of each subcarrier can be made so narrow that each subcarrier experiences only flat fading. Secondly, it is spectral efficient because the subcarrier spacing is minimized to enhance the overall bandwidth efficiency. Finally, it can be easily realized because the signal processing architectures for transmitter and receiver need only IFFT, FFT and frequency domain equalization. However, there is a potential barrier for OFDM to become truly practical for mobile communications. When the channel response varies rapidly in time, orthogonality between subcarriers is destroyed and inter-carrier interference (ICI) arises, which will degrade the system performance severely. Therefore, techniques for combating Doppler effects are desperately needed in OFDM technologies.

Recently a joint multipath-Doppler diversity technique for DS-CDMA systems is introduced [1]. The RAKE technique is extended to exploit joint multipath-Doppler diversity.

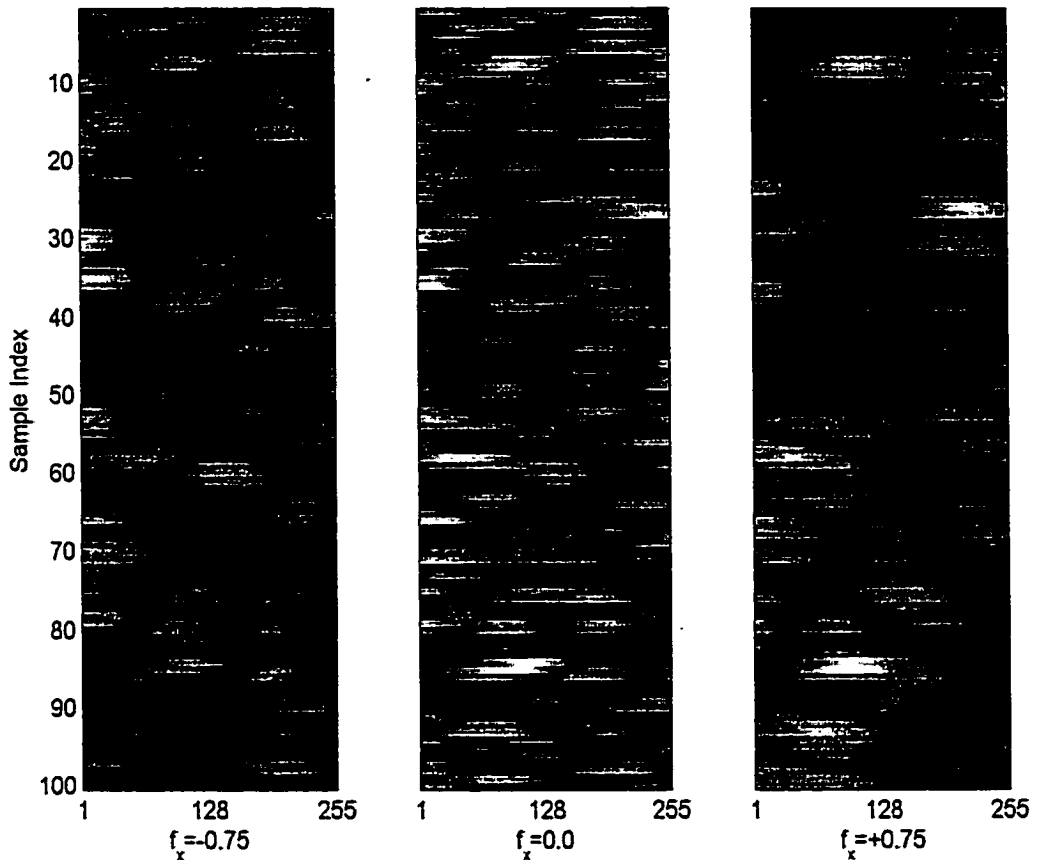


**Figure 2.1** The time varying channel responses for subcarriers for three Doppler branches when  $F_D T = 0.25$ . The x-axis of each plot represents the index of subcarrier and y-axis the index of time frame.  $f_x$  represents the shifting frequency for corresponding Doppler branch.

It improves performance of the DS-CDMA system when the fading rate of the channel increases. Other works on Doppler diversities are reported for single carrier systems in frequency selective fading [2] or flat fading channels [3]. In this paper, we propose a new frequency-domain processing scheme to exploit Doppler diversity for OFDM multicarrier systems in frequency selective channel.

A general idea of achieving Doppler diversity is to generate Doppler branches from the received signal by artificial frequency shifts. These frequencies are in the order of the

reciprocal of symbol duration. Doppler diversity takes advantage of incoherency of channel responses for the Doppler branches. Figure 2.1 illustrates incoherent time-varying channel responses for three Doppler branches. The output of every Doppler branch is composed of same set of signal components arriving from different paths. However, the relative weights and phases for every component in a branch is different from those in other branches when the received signal is Doppler spread. Therefore, the time-varying channel response for each branch is incoherent with each other. If the outputs of such branches are combined properly, the fading can be mitigated.

Since Doppler spread causes ICI in OFDM systems but not in single carrier systems (including DS-CDMA), the principle of Doppler diversity for OFDM systems is very different from that for the single carrier systems. For example, in DS-CDMA communications as shown in [1], Doppler diversity can be easily realized since the frequency selective fading of signal components at different Doppler branches becomes less correlated as fading rate increases. With the aid of RAKE receiver, the signals from different Doppler branches of the entire spectrum are combined. While signal to noise ratio (SNR) at some specific frequencies may degrade, the overall SNR will improve as fading rate increases. However, OFDM faces a different and much more difficult situation. Firstly, Doppler diversity cannot preserve or recover orthogonality between subcarriers in OFDM systems. Secondly, ICI increases and desired signal component decreases as fading rate increases. Thirdly, ICI increases and desired signal component decreases as the artificial frequency in a Doppler branch increases. Finally, improvement of SINR at some subcarriers but degradation of SINR at others is not desirable. Therefore, the Doppler diversity technique employed in DS-CDMA or other single carrier systems cannot be applied to OFDM systems.

Here, we propose a new frequency domain Doppler diversity scheme for OFDM. Without using time-domain equalizers, which is usually expensive, the distribution of the Doppler combined signal is changed to improve BER while the averaged SINR remains more or less in the same level as that without Doppler diversity.

## 2.2. Formulation

### 2.2.1. Channel and Signal Models

Using the channel model in (1.10) with single antenna the multipath, time-varying channel impulse response  $h(t, \tau)$  is represented as

$$h(t, \tau) = \frac{1}{\sqrt{N_p}} \sum_{p=1}^{N_p} a_p \delta(\tau - \tau_p) e^{j2\pi f_{D_p} t} \quad (2.1)$$

where  $a_p$ ,  $\tau_p$ , and  $f_{D_p}$  are the complex amplitude, time delay, and Doppler shift of the  $p^{\text{th}}$  multipath arrival. Though  $a_p$ ,  $\tau_p$ , and  $f_{D_p}$  are stochastic random processes, their variations are, in practice, so small during our observation interval of several symbol durations that they can be regarded as random variables. Thus, we assume that complex path gain  $\{a_p\}$  are i.i.d. Gaussian random variables with zero mean and variance  $\sigma_a^2$ , and  $\{\tau_p; 0 < \tau_p < \tau_{\max}\}$  and  $\{f_{D_p}; -F_D < f_{D_p} < F_D\}$  are i.i.d. random variables with uniform distributions.

Consider an OFDM signal containing  $N$  sub-carriers

$$s(t) = \frac{1}{\sqrt{N}} \sum_{r=0}^{N-1} \alpha_r e^{j\frac{2\pi}{N} r t} \xi(t) \quad (2.2)$$

where  $d_i$  is the  $i^{\text{th}}$  BPSK-modulated subsymbol to be transmitted,  $T$  is the symbol duration,  $g(t)$  is symbol window such that

$$g(t) = \begin{cases} 1, & -T_g \leq t < T \\ 0, & \text{otherwise} \end{cases}, \quad (2.3)$$

and  $T_g$  is the duration of cyclic-prefix which is equal to or greater than the maximum delay spread of channel.

From the convolution of input and impulse response of the channel, the received sample sequence for a symbol after removing cyclic-prefix can then be represented as

$$\begin{aligned} x(nT_s) &= \frac{1}{\sqrt{N_p}} \sum_{p=1}^{N_p} a_p s(nT_s - \tau_p) e^{j2\pi f_{c,p} nT_s} + v(nT_s) \\ &= \frac{1}{\sqrt{N_p N}} \sum_{p=1}^{N_p} a_p e^{j2\pi f_{c,p} nT_s} \sum_{i=0}^{N-1} d_i e^{j\frac{2\pi}{N} i(nT_s - \tau_p)} + v(nT_s) \end{aligned} \quad (2.4)$$

where  $T_s$  is the sampling interval,  $v(kT_s)$  denotes the additive white Gaussian noise with variance  $\sigma_n^2$ . Note that the symbol duration  $T = NT_s$  to make subcarriers orthogonal to each other, and  $T_g = N_g T_s$ . For convenience and without loss of generality,  $T_s$  will be set to be one throughout this paper.

### 2.2.2. Doppler Branches

The proposed frequency domain Doppler diversity scheme with  $Q$  branches is shown in Figure 2.2. For the  $q^{\text{th}}$  Doppler branch, the received signal  $x(k)$  is first shifted by a predetermined frequency  $f_x$ , and then matched-filtered using DFT. Each output of matched filter is scaled to maintain equal level of interference-and-noise power to other branches. The scaled outputs are multiplied by the corresponding complex conjugate of channel gain

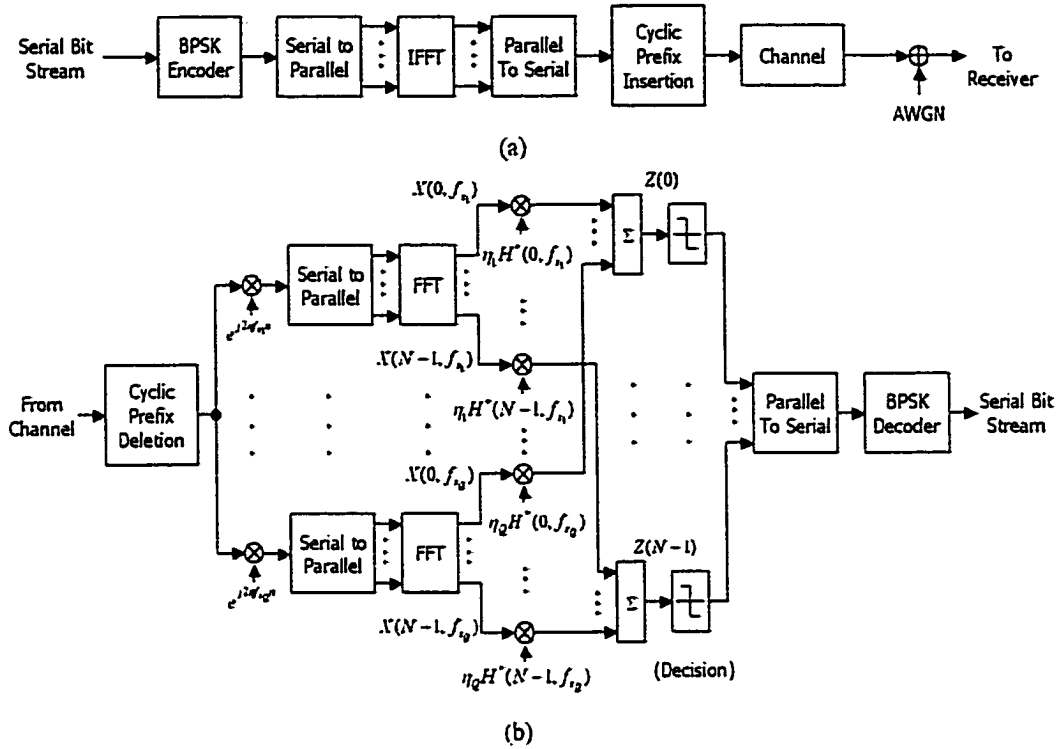


Figure 2.2 OFDM transmitter (a) and receiver with Doppler diversity (b)

$H(i, f_x)$  before combining. The  $i^{\text{th}}$  matched filter output of the branch with shifting frequency  $f_x$ ,  $X(i, f_x)$ , can be represented by

$$X(i, f_x) = \frac{1}{\sqrt{N}} \sum_{k=0}^{N-1} x(k) e^{-j2\pi f_x k} e^{-j2\pi \frac{f_x}{N} k} \equiv X_s(i, f_x) + X_i(i, f_x) + N(i, f_x) \quad (2.5)$$

The signal term  $X_s(i, f_x)$  is

$$X_s(i, f_x) = \frac{d_i}{N\sqrt{N_p}} \sum_{p=1}^{N_p} a_p e^{-j2\pi \frac{f_x}{N} \tau_p} e^{j\pi(N-1)(f_{D_p} - f_x)} \frac{\sin N\pi(f_{D_p} - f_x)}{\sin \pi(f_{D_p} - f_x)}, \quad (2.6)$$

the interference term  $X_i(i, f_x)$  is

$$X_i(i, f_x) = \frac{1}{N\sqrt{N_p}} \sum_{p=1}^{N_p} a_p \sum_{l=0}^{N-1} d_l e^{-j2\pi\frac{l}{N}r_p} e^{j\pi(N-1)\left(\frac{l-i}{N} + f_{D_p} - f_x\right)} \frac{\sin N\pi\left(\frac{l-i}{N} + f_{D_p} - f_x\right)}{\sin \pi\left(\frac{l-i}{N} + f_{D_p} - f_x\right)}, \quad (2.7)$$

and the noise term  $N(i, f_x)$  is

$$N(i, f_x) = \frac{1}{\sqrt{N}} \sum_{k=0}^{N-1} v(k) e^{-j2\pi\frac{l}{N}k}. \quad (2.8)$$

The channel gain for the  $i^{\text{th}}$  subcarrier at the branch with frequency shift  $f_x$ ,  $H(i, f_x)$ , can be obtained from (2.5). That is

$$H(i, f_x) = \frac{X_s(i, f_x)}{S(i)} = \frac{1}{N\sqrt{N_p}} \sum_{p=1}^{N_p} a_p e^{-j2\pi\frac{l}{N}r_p} e^{j\pi(N-1)(f_{D_p} - f_x)} \frac{\sin N\pi(f_{D_p} - f_x)}{\sin \pi(f_{D_p} - f_x)} \quad (2.9)$$

where  $S(i) = d_i$  is the  $i^{\text{th}}$  subsymbol. From (2.9), we can see that  $H(i, f_x)$  is a linear combination of  $N_p$  complex exponentials with frequency  $f_{D_p} - f_x$ . Since  $f_{D_p}$  is spread in the interval  $[-F_D, F_D]$  along the frequency axis, the combination varies for different values of frequency shift  $f_x$ . Therefore, various  $H(i, f_x)$ 's at different Doppler branches are not coherent. That implies frequency selective fading at different Doppler branches are uncorrelated or partially correlated. That is the key idea for Doppler diversity. The crosscorrelation between two branches with frequency shift  $f_{x_1}$  and  $f_{x_2}$  can be represented by

$$\begin{aligned} R_{HH}^{(i)}(f_{x_1}, f_{x_2}) &= E\{H(i, f_{x_1})H^*(i, f_{x_2})\} \\ &= \frac{1}{N^2 N_p} E \left\{ \sum_{p=1}^{N_p} a_p e^{-j2\pi\frac{l}{N}r_p} e^{j\pi(N-1)(f_{D_p} - f_{x_1})} \frac{\sin N\pi(f_{D_p} - f_{x_1})}{\sin \pi(f_{D_p} - f_{x_1})} \right. \\ &\quad \times \left. \left( \sum_{p=1}^{N_p} \rho_p e^{-j2\pi\frac{l}{N}r_p} e^{j\pi(N-1)(f_{D_p} - f_{x_2})} \frac{\sin N\pi(f_{D_p} - f_{x_2})}{\sin \pi(f_{D_p} - f_{x_2})} \right)^* \right\} \\ &= \frac{1}{N^2 N_p} E \left\{ \sum_{p=1}^{N_p} |a_p|^2 e^{j\pi(N-1)(f_{x_2} - f_{x_1})} \frac{\sin N\pi(f_{D_p} - f_{x_1})}{\sin \pi(f_{D_p} - f_{x_1})} \frac{\sin N\pi(f_{D_p} - f_{x_2})}{\sin \pi(f_{D_p} - f_{x_2})} \right\} \end{aligned}$$

$$= \frac{\sigma_a^2}{N^2 N_p} \sum_{n=1}^{N_p} E \left\{ e^{j\pi(N-1)(f_{r_2} - f_{r_1})} \frac{\sin N\pi(f_{D_p} - f_{x_1}) \sin N\pi(f_{D_p} - f_{x_2})}{\sin \pi(f_{D_p} - f_{x_1}) \sin \pi(f_{D_p} - f_{x_2})} \right\}. \quad (2.10)$$

Note that the crosscorrelation in (2.10) of channel gains between branches are independent of the subcarrier index  $i$ .

Interference  $X_i(i, f_x)$  is a random variable which is uncorrelated with signal component  $X_s(i, f_x)$  since all subsymbols  $\{d_i\}$  are mutually independent. Furthermore, its distribution must be close to zero-mean Gaussian by the central limit theorem, because it is a sum of a large number of i.i.d. zero-mean random variables (assuming the number of subcarriers  $N$  is large enough). The crosscorrelation between the interference components of two Doppler branches is

$$\begin{aligned} R_{ii}^{(i)}(f_{x_1}, f_{x_2}) &= E \{ X_i(i, f_{x_1}) X_i^*(i, f_{x_2}) \} \\ &= \frac{1}{N^2 N_p} E \left\{ \sum_{n=1}^{N_p} a_n \sum_{\substack{l=1 \\ l \neq i}}^N d_l e^{-j2\pi \frac{l}{N} \tau_n} e^{j\pi(N-1) \left( \frac{l-i}{N} f_{D_n} - f_{x_1} \right)} \frac{\sin N\pi \left( \frac{l-i}{N} + f_{D_n} - f_{x_1} \right)}{\sin \pi \left( \frac{l-i}{N} f_{D_n} - f_{x_1} \right)} \right. \\ &\quad \times \left. \left( \sum_{n=1}^{N_p} a_n \sum_{\substack{l=1 \\ l \neq i}}^N d_l e^{-j2\pi \frac{l}{N} \tau_n} e^{j\pi(N-1) \left( \frac{l-i}{N} f_{D_n} - f_{x_2} \right)} \frac{\sin N\pi \left( \frac{l-i}{N} + f_{D_n} - f_{x_2} \right)}{\sin \pi \left( \frac{l-i}{N} f_{D_n} - f_{x_2} \right)} \right)^* \right\} \\ &= \frac{1}{N^2 N_p} \sum_{n=1}^{N_p} \left[ E \{ |a_n|^2 \} \sum_{\substack{l=1 \\ l \neq i}}^N E \{ |d_l|^2 \} e^{j\pi(N-1)(f_{r_2} - f_{r_1})} \right. \\ &\quad \times \left. E \left\{ \frac{\sin N\pi \left( \frac{l-i}{N} + f_{D_n} - f_{x_2} \right) \sin N\pi \left( \frac{l-i}{N} + f_{D_n} - f_{x_1} \right)}{\sin \pi \left( \frac{l-i}{N} f_{D_n} - f_{x_2} \right) \sin \pi \left( \frac{l-i}{N} f_{D_n} - f_{x_1} \right)} \right\} \right] \end{aligned}$$



$$= \frac{\sigma_a^2 \sigma_d^2}{N^2} e^{j\pi(N-1)(f_{x_2} - f_{x_1})} \sum_{l=1}^N E \left\{ \frac{\sin N\pi \left( \frac{l-i}{N} + f_{D_n} - f_{x_2} \right) \sin N\pi \left( \frac{l-i}{N} + f_{D_n} - f_{x_1} \right)}{\sin \pi \left( \frac{l-i}{N} f_{D_n} - f_{x_2} \right) \sin \pi \left( \frac{l-i}{N} f_{D_n} - f_{x_1} \right)} \right\} \quad (2.11).$$

From (2.10) signal power can be represented by

$$P_s(f_x) = R_s(f_x, f_x) = R_{HH}(f_x, f_x) \quad (2.12)$$

and from (2.11), the interference power can be expressed as

$$P_i(f_x) = R_{ii}^{(i)}(f_x, f_x) \quad (2.13)$$

Figure 2.3 shows the signal power and interference power as a function of artificial frequency shift  $f_x$  for three values of  $F_D T$ 's. Note that the signal power decreases, while the

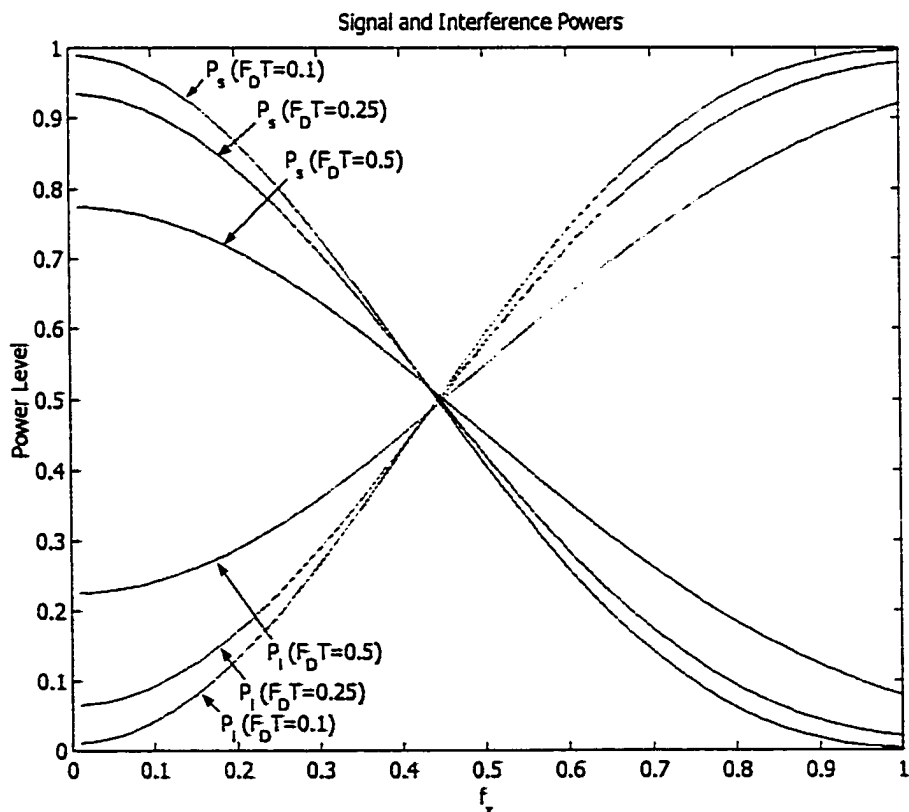


**Figure 2.3** Power level of interference and signal component for  $f_x$  ranging from 0 to 1.0.

interference power increases, as  $f_x$  or  $F_D T$  decreases. This distinct OFDM feature makes Doppler diversity very difficult to implement for OFDM systems.

Figure 2.4 shows signal power to interference power ratio ( $SIR$ ) versus  $F_D T$  for four  $f_x T$ 's when total number of subcarrier  $N$  is 256. Generally,  $SIR$  decrease as  $f_x T$  increases or  $F_D T$  increases (except at large  $f_x T$ ). It is interesting to see that  $SIR$ , though less than 0, increases as  $F_D T$  increases at large  $f_x T$  (e.g., 0.75). This implies that one could obtain a larger Doppler diversity gain (if it can be achieved) when fading rate is faster ( $F_D T$  is larger).

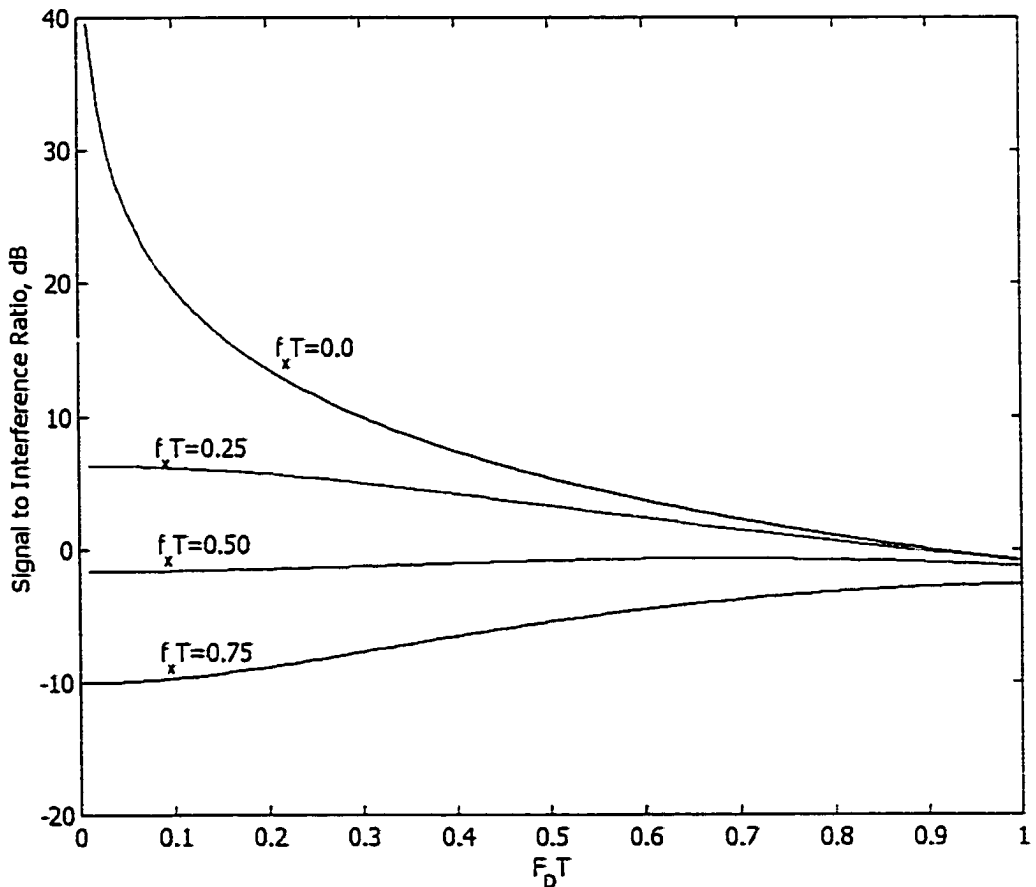


**Figure 2.4** Signal to interference ratio ( $SIR$ ) vs  $F_D T$  for 4 different  $f_x$ 's

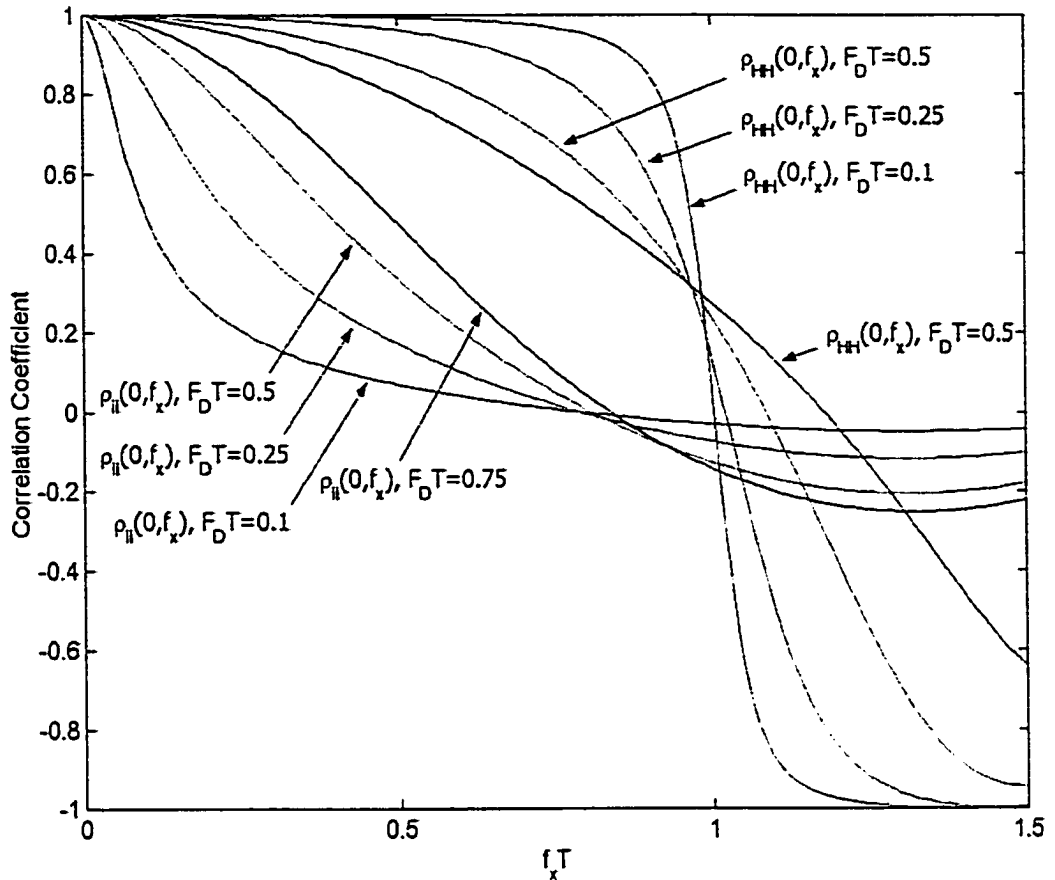


**Figure 2.5** Correlation coefficients of channels and interferences for  $F_D T$  of 0.1, 0.25, 0.5 and 0.75

### 2.2.3. Frequency Shifts for Doppler Branches

Doppler branches are formed by complex frequency shifting of received signal. Selection of these frequencies is important, since the statistical property of branches depends on  $f_x$ . As shown previously that interference power increases and signal power decreases as  $f_x$  increases.

Let us examine correlation coefficients for channel gains between two branches with frequency shift  $f_{x_1}$ , and  $f_{x_2}$ ,  $\rho_{iH}(f_{x_1}, f_{x_2})$ , and that for interference:

$$\rho_{\text{HH}}(f_{x_1}, f_{x_2}) = \frac{R_{\text{HH}}(f_{x_1}, f_{x_2})}{\sqrt{R_{\text{HH}}(f_{x_1}, f_{x_1})R_{\text{HH}}(f_{x_2}, f_{x_2})}} \quad (2.14)$$

$$\rho_{\text{ii}}(f_{x_1}, f_{x_2}) = \frac{R_{\text{ii}}(f_{x_1}, f_{x_2})}{\sqrt{R_{\text{ii}}(f_{x_1}, f_{x_1})R_{\text{ii}}(f_{x_2}, f_{x_2})}} \quad (2.15)$$

In Figure 2.5, correlation coefficients between a branch with frequency shift  $f_{x_1} = 0$  and a second branch with shift  $f_{x_2} = f_x$  is plotted for different  $F_D T$ s. It is interesting to see that the correlations of interferences for various cases are almost zero for  $f_x$  is near 0.75.

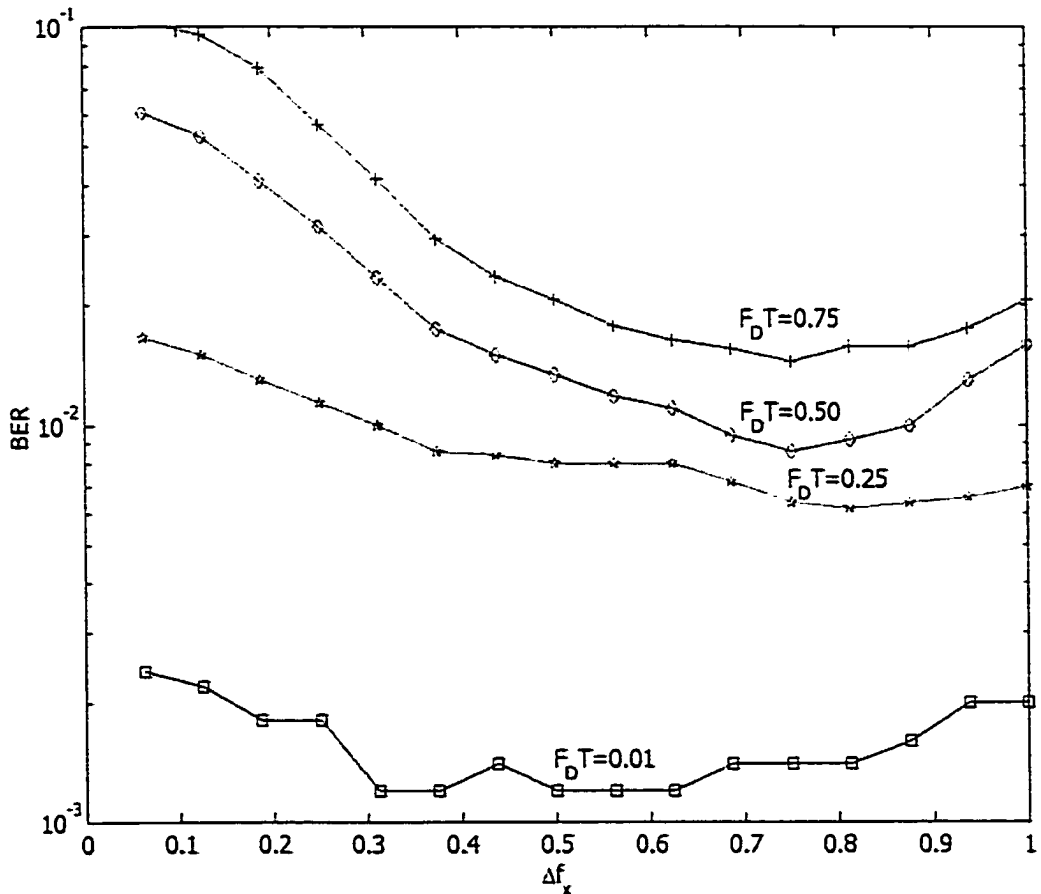


Figure 2.6 BER vs  $\Delta f_x T$  for 3 branch Doppler diversity

If the frequency spacing between these two branches  $\Delta f_x$  is too small, fading will be very much correlated and there is no diversity gain by combining these two branches. On the other hand, if the spacing of  $\Delta f_x$  is too large, signal power is too small and interference power is too high at the second branch, combining these two branches does more harm than good. Therefore, selecting these artificial frequency shifts is not a simple problem.

We used extensive simulations to find the “best” frequency shifts for each branches. Only some selective results are shown in Figure 2.6. In Figure 2.6, the number of branches  $Q$  is 3 where there is no frequency shift for the center branch and frequency shifts for two other branches are  $\pm\Delta f_x$ . It is shown that  $\Delta f_x = 0.75/T$  to  $0.8/T$  show the best results disregarding the value of  $F_D$ . At this frequency, as shown in Figure 2.5, the correlation coefficients of interferences are close to 0 (uncorrelated).

#### 2.2.4. Combining Weights

By selecting  $f_x = 0.75$  to  $0.8$ , channel gains for branches are partially correlated, and interferences are uncorrelated. Since the interference levels for all Doppler branches are not the same, the received signal level is scaled by  $\eta_q$ ,

$$\eta_q(f_x) = \sqrt{\frac{P_i(0)}{P_i(f_x)}}, \quad (2.16)$$

to make all interference levels equal. In (2.16), interference powers can be obtained by (2.12-13). Here, channel information is assumed known.

Using maximal ratio combining [4], each branch is multiplied by complex conjugate of the corresponding channel gain. By doing so, phases are corrected and branches are combined coherently with other branches, and branch weights are proportional to  $SIR$ . The

output of the combiner  $Z(i)$  can be represented by

$$Z(i) = \sum_{q=1}^Q \eta_q H^*(i, f_{x_q}) X(i) \quad (2.17)$$

### 2.3. Simulation

Simulation setup is shown in Table 2.1. In order to investigate the effect of Doppler diversity on signal and interference precisely, every simulation was performed for signal components and interferences separately, but with same channel parameters. Signal is a single carrier waveform separated from an OFDM symbol, and interference is the sum of all other subcarriers. Signal and interference sequences are passed through the simulated channel with identical parameters. Simulations were performed for 5000 symbols with independent channel parameters. In Figure 2.7, the histograms of normalized outputs (i.e., outputs divided by the source symbol  $d_i$ ) of the center branch alone and of the diversity combiner are shown. Here, the center branch corresponds to the conventional receiver without diversity. The areas below zero correspond to the symbol error. Since the channel response is complex Gaussian, outputs of branches multiplied by conjugate of channel gain have chi-square distribution. If the branches are mutually uncorrelated and they have the same  $SIR$ , the diversity combining would increase the degrees of freedom for its output distribution by the number of branches. However, as shown in Figure 2.5, branches are correlated and therefore the order of diversity did not increase as the number of branches increases. However, we can see changes in shapes of histogram (i.e., changes of probability distribution) for the combined output. Such changes become obvious as Doppler spread increases above  $F_D T = 0.25$ .

Table 2.1 Simulation setup

	PARAMETER	ABBREV.	VALUE
Channel	Number of Paths	$N_p$	128
	Maximum Delay Spread	$D_{max}$	$32T_s$
	Type of Delay Spread		Uniform (i.i.d) $0 < \tau_p < T_g$
	Type of Doppler Spectral Density		Uniform (i.i.d) $-F_D T < f_{D_p} < F_D T$
	Type of Path Gain Distribution		Complex Gaussian zero mean, (i.i.d)
	Signal to Noise Ratio	$SNR$	$\infty / 15\text{dB}$
Receiver	Number of Subcarriers Per Symbol	$N$	256 (248 active)
	Length of Cyclic Prefix	$N_g$	32 ( $= D_{max}$ )
	Number of Doppler Channels	$Q$	3
	Freq. Shifts for Doppler Branches	$\{f_x\}$	$\{-0.75T, 0, 0.75T\}$

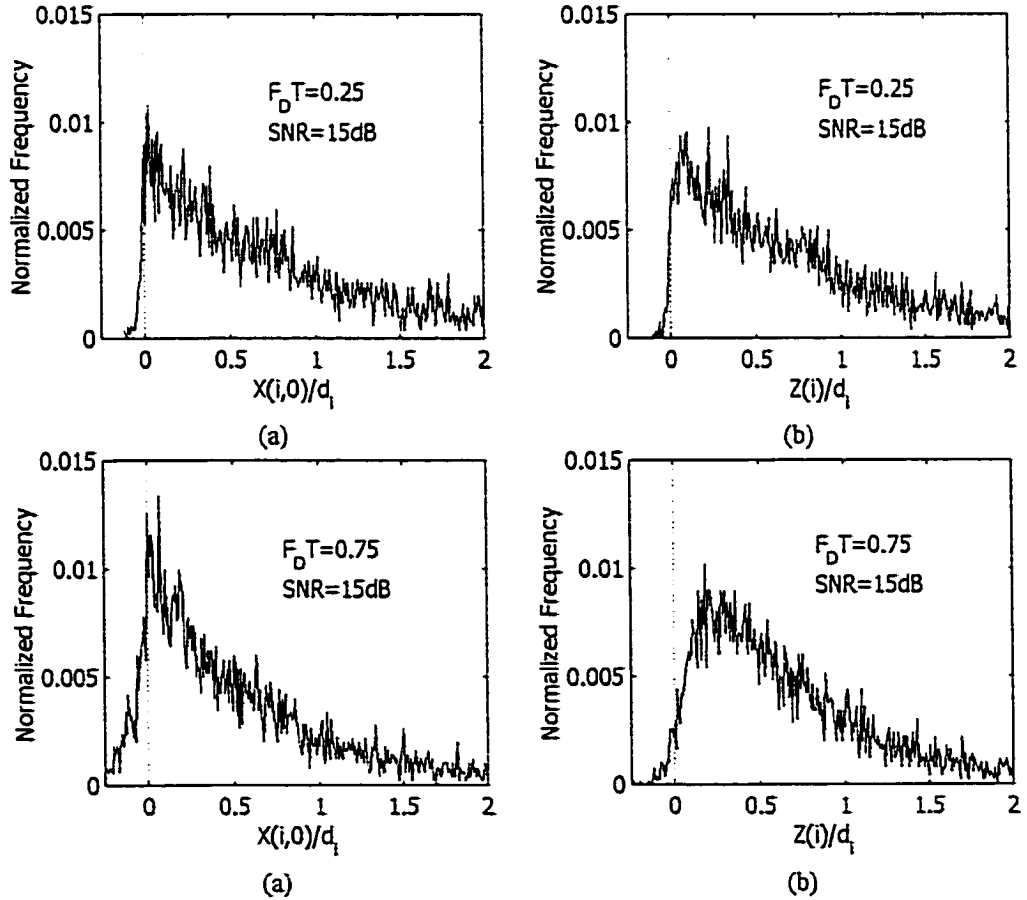


**Figure 2.7** Histograms for the center branch with  $f_x = 0$  (subfigures a & c) and histograms for the combined output (subfigures b & d). Areas below zero correspond to symbol error.

The BER performances in noise-free conditions and 15dB SNR are shown in Figure 2.8. In noise free case, the BER decreases even at  $F_D T = 0.05$ . For SNR=15 dB case, when noise is dominant (up to  $F_D T \approx 0.2$ ), the improvement is small. However, as  $F_D T$  increases, the improvements become significant. These results agree with the observation on the histograms in Figure 2.7.

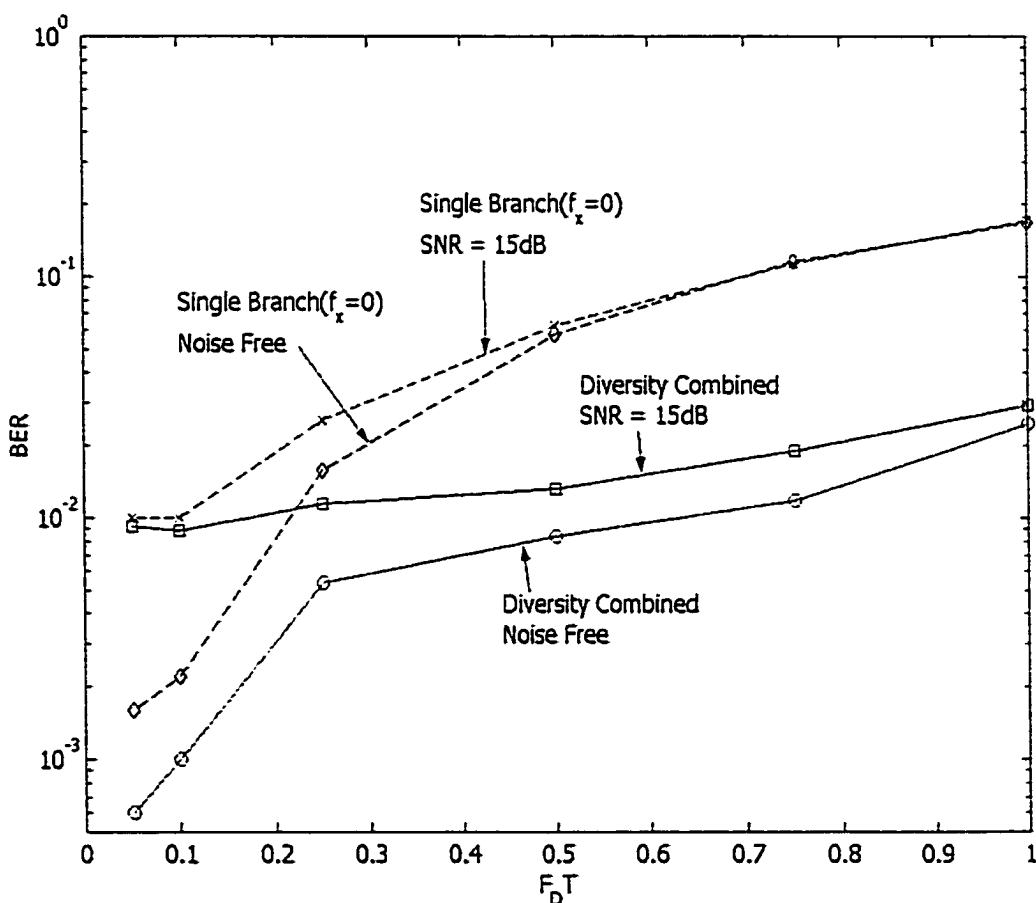


**Figure 2.8** BER versus FDT for noise-free and 15dB SNR. Two dashed lines correspond to BER for the system without diversity.



## 2.4. Conclusions

Doppler spread in time-varying channel causes severe performance degradation in OFDM, but at the same time, it provides diversity sources. The proposed frequency-domain Doppler diversity scheme uses only functional blocks in a standard OFDM receiver and does not require time-domain equalizer. Maximal ratio combining of only three Doppler branches (generated by artificial frequency shifts of the received signal) improves BER performance significantly (reduced by a factor of 8 with  $F_D T > 0.5$ ). By using pilot subsymbols or symbols and combining them with some type of decision feed back schemes, the required channel information can be obtained.

## References

- [1] Akbar M. Sayeed and Behnaam Aazhang, "Joint Multipath-Doppler Diversity in Mobile Wireless communications," *IEEE Trans. Commun.*, vol. 47, No.1, pp.123-131, January 1999.
- [2] Timothy A. Thomas and Fredrick W. Vook, "Multi-user frequency-domain channel identification, interference suppression, and equalization for time-varying broadband wireless communications," *Proc. Sensor Array and Multichannel Signal Processing Workshop. 2000*, pp. 444 –448, March 2000.
- [3] Boudreau, R, Chouinard, J.-Y. and Yongacoglu, A., "Exploiting Doppler-diversity in flat, fast fading channels," *Canadian Conference on Electrical and Computer engineering 2000*, vol. 1, pp. 270-274, March 2000.
- [4] John G. Proakis, *Digital Communications*, New York: McGraw-Hill, 3rd ed., pp.777-795, 1995.

## Chapter 3

### Space-Time-Frequency Processing

#### 3.1. Introduction

A signal propagating through the wireless channel arrives at receiver along a number of different paths, so-called multipaths. This is mainly due to scattering, reflection and diffraction of the radiating wave by buildings, hills and other structures near the mobile unit or base station. In addition, fast fading results from the geometry changes from transmitter to receiver in time, that is mainly due to the movement of mobile unit. Multipath propagation and fast fading cause the spreading of the signal in different dimensions. They are the delay (or time) spread, Doppler (or frequency) spread and angular spread. These spreads have significant effects on the signal, and in most cases, they degrade the performance of conventional receivers. However, on the other hand, if all these extra dimensions are exploited, not only such degradation is mitigated but also the capacity can be augmented. For example, though the angular spreads widen the Doppler spreads, they provide spatial selectivity for wave fronts.

In the previous chapter, a frequency domain Doppler diversity scheme for OFDM receivers was discussed, where equalization and weighting are carried out for every subcarrier individually after matched filtering. It employs Doppler diversity (using the effect of Doppler spreads) to mitigate frequency selectivity of the channel (caused by temporal spreads). In this chapter, two alternative space-time-frequency processing (STFP) approaches will be investigated. These approaches exploit spatial, temporal, and spectral dimensions to mitigate multipath and time varying (fast fading) effects.

Three existing and three new processing schemes can be considered as special cases of the proposed STFP scheme. At first, consider the three one-dimensional approaches. If both the

number of antennas,  $M$ , and the number of Doppler branches,  $Q$ , are 1, the STFP scheme becomes a conventional MMSE linear equalizer with  $L$  taps [2]. This time processing only scheme is denoted as TP. If both the number of antennas,  $M$ , and the number of taps,  $L$ , are 1, the STFP scheme becomes the new frequency domain Doppler diversity scheme with  $Q$  branches. This frequency processing only scheme is denoted as FP. If both the number of taps,  $L$ , and the number of Doppler branches,  $Q$ , are 1, the STFP scheme becomes a conventional beamformer with  $M$  antennas. This space processing only scheme is denoted as SP. Secondly, consider the other three two-dimensional approaches. If the number of antennas  $M$  is 1, the STFP scheme becomes a new time-domain Doppler diversity scheme with  $L$  taps and  $Q$  branches. This time-frequency processing scheme, denoted as TFP. If the number of taps  $L$  is 1, the single-summation STFP scheme becomes a space domain Doppler diversity scheme with  $M$  antennas and  $Q$  branches. If the number of Doppler branches,  $Q$  is 1, the single-summation STFP scheme becomes a conventional space-time processor [1] (denoted as STP) with  $M$  antennas and  $L$  tapes. Among the three new processing schemes, FP has been presented in Chapter 2, TFP is going to be discussed in Section 3.3.5, and SFP will be developed in future studies.

### 3.2. Space-Time-Frequency Processing (STFP)

The new receiver schemes for space-time-frequency processing (STFP) are shown in Figure 3.1 and Figure 3.2. These schemes are extensions of the conventional minimum mean squared error (MMSE) space-time processing. In addition to angular spread and delay spread, the new schemes make use of Doppler spreads as an additional diversity source.

The first scheme (Figure 3.1), single-summation STFP, signals having different path delays, Doppler spreads and/or arriving angles are combined with proper weights in one process to minimize the mean squared error between the recovered waveforms and the transmitted ones. The optimum  $MQL$  weights are determined by solving Wiener-Hopf equations. They are obtained from the product of the inverse of a  $MQL \times MQL$  autocorrelation matrix and the corresponding  $MQL \times 1$  crosscorrelation vector. Here,  $M$  is the number of antennas,  $Q$  is the number of Doppler branches and  $L$  is the number of time-taps.

The second scheme in Figure 3.2, double-summation STFP, is simpler in terms of

computational complexity than the first one. It, however, still exploits all three dimensions of diversities mentioned above. To simplify the computational burden, this processing scheme computes weights for each Doppler branch separately from other Doppler branches, though they are highly correlated. It is less complex since the optimum  $Q(ML+1)$  weights are computed in two sequential phases. In the first phase, the  $ML$  time-space weights for each Doppler branch are obtained from the product of the inverse of a  $ML \times ML$  autocorrelation

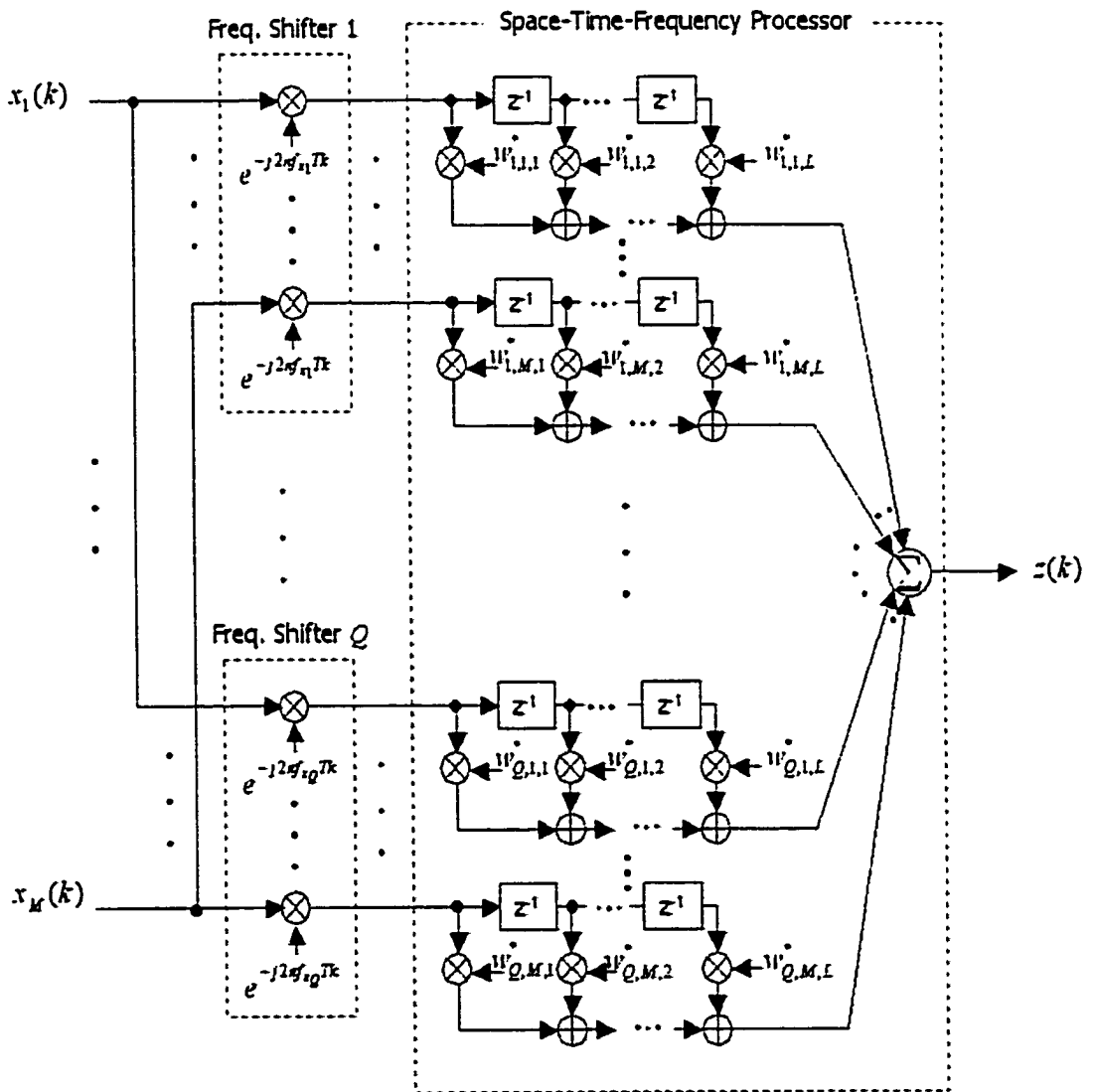


**Figure 3.1** Block diagrams of the single-summation space-time-frequency processor

matrix and the corresponding  $ML \times 1$  cross correlation vector. This process is done  $Q$  times for  $Q$  Doppler branches. In the second phase, the  $Q$  Doppler diversity weights are obtained from the product of the inverse of  $Q \times Q$  autocorrelation matrix and the  $Q \times 1$  cross correlation vector. In both schemes, the optimum weights suppress the waveforms that have low correlation with the transmitted ones, such as interferences or noise, and coherently combine others to make its output as close to the transmitted one as possible.

It is obviously that there are other types of two-phase double-summation and three-phase triple-summation approaches. These approaches will be developed in future studies.

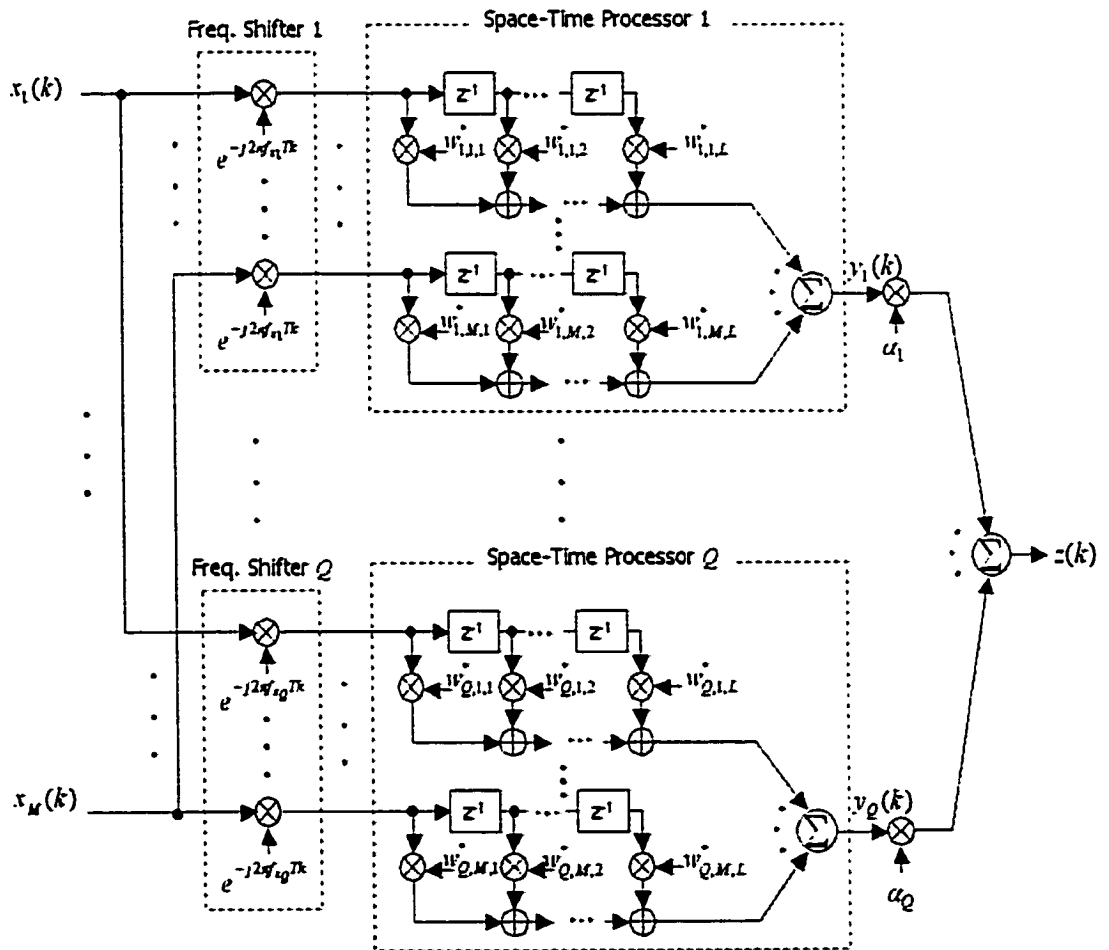


Figure 3.2 Block diagrams of the double-summation space-time-frequency processor

### 3.2.1. Single-Summation STF Processing

In order to take advantage of angle spreads, Doppler spreads and delay spreads, samples from different locations in spatial, temporal and spectral dimensions should be first obtained. Then, STFP combines these samples with optimum weights satisfying MMSE criteria. Sampling in spatial dimension can be made by array antenna; sampling in frequency dimension can be obtained by Doppler branches; and sampling in temporal dimension can be carried out by usual sampling of continuous waveforms.

Let the  $k^{\text{th}}$  time sample from the  $m^{\text{th}}$  antenna be  $x_m(k)$ . Then, the frequency-shifted version of  $x_m(k)$  for the  $q^{\text{th}}$  Doppler branch can be represented by

$$x_{q,m}(k) = x_m(k)e^{-j2\pi f_{r_q}k} \quad (3.1)$$

where  $f_{r_q}$  is the frequency shift for the  $q^{\text{th}}$  Doppler branch.

The  $L \times 1$  time sample vector from the  $m^{\text{th}}$  antenna for the  $q^{\text{th}}$  Doppler branch  $\mathbf{x}_{q,m}(k)$  is expressed as

$$\begin{aligned} \mathbf{x}_{q,m}(k) &= [x_{q,m}(k-L/2+1) \quad \Lambda \quad x_{q,m}(k+L/2)]^T \\ &= [x_m(k-L/2+1)e^{-j2\pi f_{r_q}(k-L/2+1)} \quad \Lambda \quad x_m(k+L/2)e^{-j2\pi f_{r_q}(k+L/2)}]^T, \end{aligned} \quad (3.2)$$

The  $ML$  space-time sample for the  $q^{\text{th}}$  Doppler branch  $X_q(k)$  can be expressed as

$$X_q(k) = [\mathbf{x}_{q,1}^T(k) \quad \Lambda \quad \mathbf{x}_{q,M}^T(k)]^T. \quad (3.3)$$

where the superscript  $T$  denotes transpose.

For the first scheme in Figure 3.1, the sample vector input to STFP should be composed of the samples from all three dimensions. Therefore,  $MLQ \times 1$  sample vector  $X(k)$  for STFP in Figure 3.1 becomes

$$X(k) = [X_1^T(k) \quad \Lambda \quad X_Q^T(k)]^T. \quad (3.4)$$

The weight vector corresponding to  $\mathbf{x}_{q,m}(k)$ ,  $\mathbf{w}_{q,m}$ , can be represented by

$$\mathbf{w}_{q,m} = [w_{q,m,1} \quad \Lambda \quad w_{q,m,L}]^T \quad (3.5)$$

where  $w_{q,m,l}$  is the weight for the  $l^{\text{th}}$  tap, the  $q^{\text{th}}$  Doppler branch and the  $m^{\text{th}}$  antenna.

The  $M \times L$  weight vector for sample vector of the  $q^{\text{th}}$  Doppler branch  $X_q(k)$ ,  $W_q$ , can be expressed by

$$W_q = \begin{bmatrix} \mathbf{w}_{q,1}^T & \Lambda & \mathbf{w}_{q,M}^T \end{bmatrix}^T \quad (3.6)$$

Finally, the  $MLQ \times 1$  weight vector  $W$  corresponding to the sample vector  $X(k)$  is

$$W = \begin{bmatrix} W_1^T & \Lambda & W_Q^T \end{bmatrix}^T. \quad (3.7)$$

Therefore, the output of STFP  $z(k)$  at observation time  $k$ , which is the weighted sum of samples from the spatial, temporal and frequency dimensions, can be represented as

$$z(k) = W^H X(k). \quad (3.8)$$

The MMSE optimum weight vector  $W_{\text{opt}}$  is achieved by solving

$$W_{\text{opt}} = \arg \min_W E \left\{ |z(k) - s(k)|^2 \right\} \quad (3.9)$$

where  $s(k)$  is defined as the  $k^{\text{th}}$  sample of transmitted signal.

From the projection theorem, the MMSE optimum solution satisfies

$$E \left[ X(k) (X(k)^H W_{\text{opt}} - s^*(k)) \right] = \mathbf{0}, \quad (3.10)$$

or equivalently, the Weiner Hopf equation is resulted as

$$\mathbf{R}_{XX} W_{\text{opt}} = \mathbf{r}_{Xs}, \quad (3.11)$$

where the superscript  $*$  denotes complex conjugate, and the  $MLQ \times MLQ$  autocorrelation matrix and  $MLQ \times 1$  crosscorrelation vector of the received signal samples are represented as

$$\mathbf{R}_{XX} = E \left\{ X(k) X^H(k) \right\} \quad (3.12)$$

and

$$\mathbf{r}_{Xs} = E \left\{ X(k) s^*(k) \right\} \quad (3.13)$$

respectively.

Solving the above Weiner Hopf equation, the optimum weight vector  $W_{\text{opt}}$  is

$$W_{\text{opt}} = \mathbf{R}_{XX}^{-1} \mathbf{r}_{Xs}. \quad (3.14)$$

### 3.2.2. Double-Summation Space-Time-Frequency Processing

The second receiver scheme shown in Figure 3.2 processes the space-time (ST) signal for each Doppler branch individually, then sum up its outputs with the proper weights. In the



first phase, the input vector to the ST processor of the  $q^{\text{th}}$  Doppler branch is  $X_q(k)$  represented in (3.3) and the corresponding weight vector is  $W_q$  in (3.6).

The output of the  $q^{\text{th}}$  ST processor can be represented by

$$y_q(k) = W_q^H X_q(k), \quad (3.15)$$

and, the optimum MMSE weight vector  $W_q^{\text{opt}}(k)$  can be derived to be

$$W_q^{\text{opt}} = [\mathbf{R}_{XX}^{(q)}]^{-1} \mathbf{r}_{Xs}^{(q)} \quad (3.16)$$

where the  $ML \times ML$  autocorrelation matrix and  $ML \times 1$  crosscorrelation vector of the  $q^{\text{th}}$  Doppler branch are represented by

$$\mathbf{R}_{XX}^{(q)} = E\{X_q(k)X_q^H(k)\} \quad (3.17)$$

and

$$\mathbf{r}_{Xs}^{(q)} = E\{X_q(k)s^*(k)\} \quad (3.18)$$

respectively.

In the second phase, the  $Q$  Doppler branches are combined to generate the STFP result  $z(k)$ , which can be represented as

$$z(k) = \alpha^H \mathbf{y}(k) \quad (3.19)$$

where the  $Q \times 1$  input vector  $\mathbf{y}(k)$ , of which elements are the outputs of ST processors, is

$$\mathbf{y}(k) = [y_1(k) \dots y_Q(k)]^T, \quad (3.20)$$

and  $\alpha$  is a  $Q \times 1$  branch weight vector. The optimum MMSE branch weight vector can be derived using the same technique used for obtaining the ST weight vector as

$$\alpha_{\text{opt}} = \mathbf{R}_{YY}^{-1} \mathbf{r}_{Ys} \quad (3.21)$$

where the  $Q \times Q$  autocorrelation matrix and  $Q \times 1$  crosscorrelation vector for Doppler diversity are represented as

$$\mathbf{R}_{YY} = E\{\mathbf{y}(k)\mathbf{y}^H(k)\} \quad (3.22)$$

and

$$\mathbf{r}_{Ys} = E\{\mathbf{y}(k)s^*(k)\} \quad (3.23)$$

respectively.

### 3.2.3. Estimation of Crosscorrelation using Pilot Subsymbols

As shown in (3.14), (3.16) and (3.21), the optimum MMSE weights are computed from the inverse of the autocorrelation matrix and the crosscorrelation vector. For a time varying channel, correlation of the received signal is also time varying. Therefore, it is necessary to obtain instantaneous correlation to calculate the optimum weights, and the weights become instantaneous for optimum processing. However, calculating weights for every sample requires high complexity of computation. Instead of updating weights for every sample, we consider computing them for every symbol-duration.

MMSE weights are computed using training or pilot signals. If the channel is time invariant, the weights can be computed once using training symbols and applied for the following successive data symbols. However, in time varying channel, since the weights need to be updated periodically, pilot symbols or subsymbols also need to be transmitted periodically. For the simulation of STFP in this thesis, the pilot subsymbols are inserted in every symbol with a constant pilot rate. The pilot rate  $\gamma_p$  is defined as

$$\gamma_p = \frac{\text{number of pilot subsymbols}}{\text{number of total subsymbols}} \quad (3.24)$$

For the single-summation STFP scheme, the sample correlation matrix and crosscorrelation vector for pilot subsymbols can be represented by

$$\hat{\mathbf{R}}_{xx} = \frac{1}{K} \sum_{k=0}^{K-1} X^{(p)}(k) X^{(p)H}(k) \quad (3.25)$$

and

$$\hat{\mathbf{r}}_{xs} = \frac{1}{K} \sum_{k=0}^{K-1} X^{(p)}(k) s_p^*(k). \quad (3.26)$$

where  $X^{(p)}(k)$  is the sample vector corresponding to  $X(k)$  which is filtered for pilot subsymbols, and  $s_p(k)$  is the  $k^{\text{th}}$  sample of pilot symbol.

Similarly, for the double-summation STFP scheme,

$$\hat{\mathbf{R}}_{yy} = \frac{1}{K} \sum_{k=0}^{K-1} \mathbf{y}^{(p)}(k) \mathbf{y}^{(p)H}(k) \quad (3.27)$$

and

$$\hat{\mathbf{r}}_{yx} = \frac{1}{K} \sum_{k=0}^{K-1} \mathbf{y}^{(p)}(k) s_p^*(k) \quad (3.28)$$

where  $\mathbf{y}^{(p)}(k)$  is the sample vector corresponding to  $\mathbf{y}(k)$  which is filtered for pilot subsymbols.

Finally, those for (3.23) is

$$\hat{\mathbf{R}}_{XX}^{(q)} = \frac{1}{K} \sum_{k=0}^{K-1} X_q^{(p)}(k) X_q^{(p)H}(k) \quad (3.29)$$

and

$$\hat{\mathbf{r}}_{Xx}^{(q)} = \frac{1}{K} \sum_{k=0}^{K-1} X_q^{(p)}(k) s_p^*(k). \quad (3.30)$$

where  $X_q^{(p)}(k)$  is the filtered sample vector corresponding to  $X_q(k)$ .

### 3.3. Simulation

Using the channel simulator introduced in chapter 1, the performances of two STFP's are compared and examined. The number of paths  $N_p$  is chosen to be 128 and the maximum

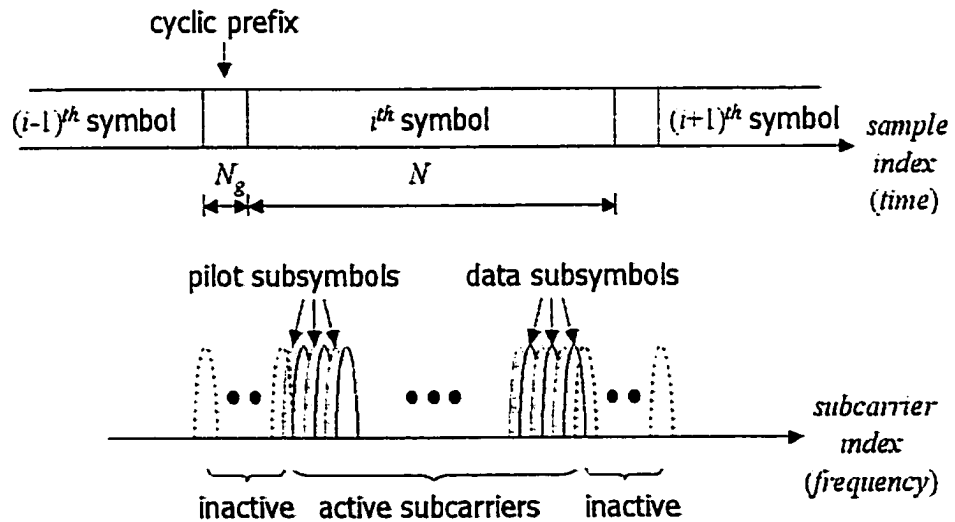


**Figure 3.3** OFDM symbol structure in time and frequency domain (pilot rate  $\frac{1}{2}$ )

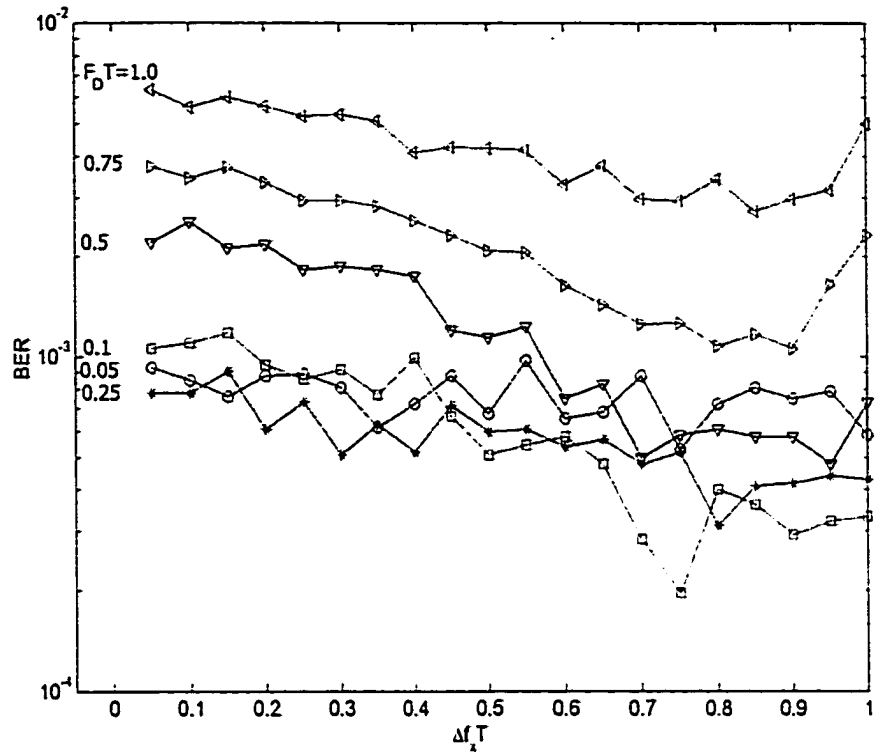
delay spread is 32 sample-intervals. The Doppler spectral density is uniformly distributed in between  $-\text{FD}$  and  $\text{FD}$ , where  $\text{FD}$  is the maximum Doppler spread. The OFDM symbols used for the simulations are shown in Figure 3.3. They are composed of  $N$  subcarriers. Eight lowest subcarriers and eight highest subcarriers are inactive. Each subsymbol is BPSK modulated, and every symbol is preceded by a cyclic prefix with duration equal to the maximum channel delay,  $T_g$ . The simulation is performed in baseband, and there are  $N$  samples within the symbol period  $T$ , and  $N_g$  samples in cyclic prefix. The output of STFP is matched filtered using FFT. A subsymbol is detected by taking the sign of the real part of the corresponding FFT coefficient.

### 3.3.1. Selection of Frequency Shifts for Doppler Branches

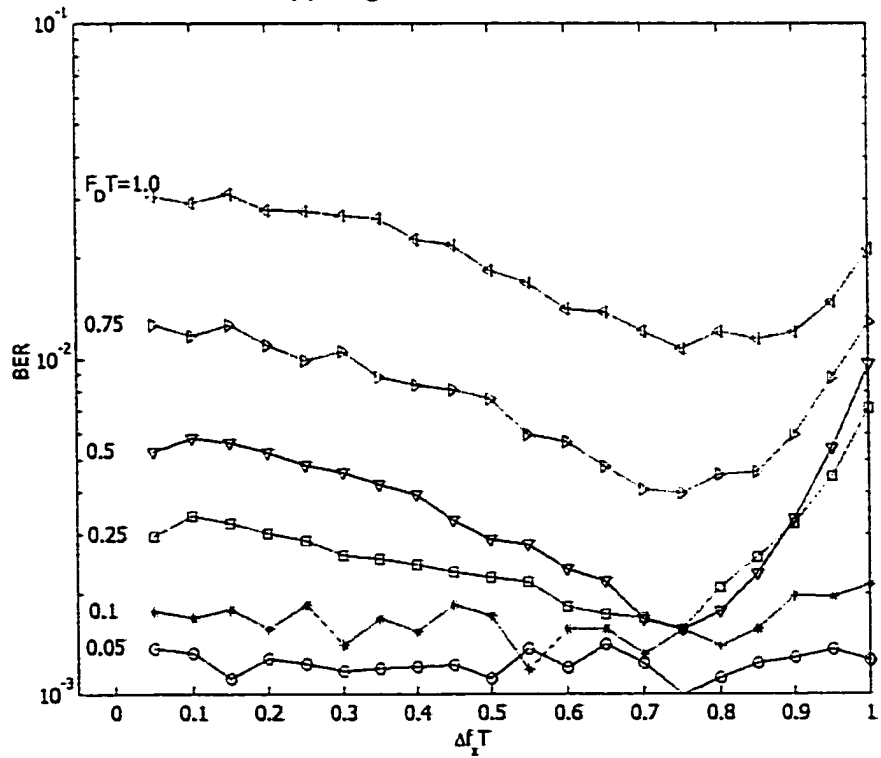
For the first simulation, the number of Doppler branches  $Q$  in STFP is selected to be 3. The three frequency shifts of the three Doppler branches are  $-\Delta f_x T$ ,  $0$  and  $\Delta f_x T$ , respectively. The number of time-taps is chosen to be 32 and the number of antenna is 1. Without any prior knowledge on the channel, the pilot subsymbols in transmitted symbols are used to compute the crosscorrelation vectors. The pilot rate is 1, i.e., the entire transmitted symbols are used for the estimation of crosscorrelation vectors. The weights are computed from (3.14), (3.16),

**Table 3.1** Simulation parameters for deriving the results in Figure 3.4

	PARAMETER	ABBREV.	VALUE
Channel	Number of Paths	$N_p$	128
	Maximum Delay Spread	$D_{max}$	$6 T_s$
	Type of Delay Spread		Uniform
	Type of Doppler Spectral Density		Uniform
	Signal to Noise Ratio	$SNR$	$\infty$
Receiver	Number of Subcarriers Per Symbol	$N$	128 (120 active)
	Pilot Ratio	$\gamma_p$	1
	Number of Time-Taps	$L$	32
	Number of Antennas	$M$	1
	Number of Doppler Channels	$Q$	3
	Freq. Shifts for Doppler Branches	$\{f_x\}$	$\{-\Delta f_x, 0, \Delta f_x\}$



(a) Single-summation STFP



(b) Double-summation STFP

Figure 3.4 BER versus  $\Delta f_x$  for various  $F_D T$

(3.21) and (3.25)-(3.30) with  $K = N$ . These signal and channel parameters are summarized in Table 3.1. The simulation results for the two STFP schemes are shown in Figure 3.4. The BER versus  $\Delta f_x T$  are plotted for six different  $F_D T$ 's. For both STFP schemes, the best choice of  $\Delta f_x T$  is between 0.75 and 0.8. Comparing the performances of these two STFP schemes, the single-summation approach is better than the double-summation approach.

### 3.3.2. BER for Various STFP Configurations (Noise Free)

The following six STFP configurations are used for simulation:

- #1. Time-only processing ( $Q=1$ ,  $M=1$  and  $L=64$ )
- #2. Time-Frequency processing with single summation ( $Q=3$ ,  $M=1$  and  $L=64$ ),
- #3. Time-Frequency processing with double summation ( $Q=3$ ,  $M=1$  and  $L=64$ ),
- #4. Space-Time processing ( $Q=1$ ,  $M=2$  and  $L=64$ ),
- #5. Space-Time-Frequency processing with single summation ( $Q=3$ ,  $M=2$  and  $L=64$ ),
- #6. Space-Time-Frequency processing with double summation ( $Q=3$ ,  $M=2$  and  $L=64$ ),

The BER performances for these six different configurations in noise free condition are shown in Figure 3.5. The number of time-taps  $L$  is 64. The pilot rate  $\gamma_p$  is 1/2, where all even-number subcarriers contain pilot subsymbols. When  $Q=3$ , the frequency shifts for Doppler branches  $\{f_{x_q}\}$  are chosen to be 0 and  $\pm 0.75/T$ . These values are based on the correlation coefficients between Doppler branches shown in Figure 2.4 and simulation results shown in Fig. 3.4. The simulation setup for Figure 3.5 is summarized in Table 3.2.

Compare the three single-antenna results. The time-frequency processing (#2 & #3, with Doppler diversity) results are much better than the time processing result (#1, without Doppler Diversity) when  $F_D T$  is large. For example, BER for the #1 case is almost ten times of the BER for #2 or #3 case when  $F_D T=1$ . The two time-frequency processing (#2 & #3) are similar to each other when  $F_D T$  is large. However, for reasons to be discussed in the next section, the single-summation method does not work well when  $F_D T$  is small. This is unexpected because the single summation scheme determines all weights simultaneously and is supposed to derive optimum solution.

Compare the three two-antenna results. As in the one-antenna situations, the space-time-frequency processing (#5 & #6, with Doppler diversity) results are much better than the space-time processing result (#4, without Doppler Diversity) when  $F_D T$  is large. For example, BER for the #4 case is ten times of the BER for # 5 or # 6 case when  $F_D T = 1$ .

Compare the space-time processing result (#4) and the time-frequency results (#2 & # 3). It is not surprised to see that the time-frequency results are better with large  $F_D T$  values while the space-time result is better with small  $F_D T$  values.

Finally, compare the cases without Doppler diversity (#1 and #4) with the cases with Doppler diversity (#2, #3, #5 and #6). BER increases as  $F_D T$  increases for all cases. However, the increasing rate for cases without Doppler diversity is larger than the cases with Doppler diversity.

Table 3.2 Simulation parameters for deriving the results in Figure 3.5

	PARAMETER	ABBREV.	VALUE
Channel	Number of Paths	$N_p$	128
	Maximum Delay Spread	$D_{max}$	$32T_s$
	Type of Delay Spread		Uniform
	Type of Doppler Spectral Density		Uniform
	Range of Angular Spread		$0 - 180^\circ$
	Types of Angular Spread		Uniform
	Signal to Noise Ratio	$SNR$	$\infty$
Receiver	Number of Subcarriers Per Symbol	$N$	1024 (1016 active)
	Pilot Ratio	$\gamma_p$	1/2
	Number of Time-Taps	$L$	64
	Number of Antennas	$M$	1 or 2
	Number of Doppler Channels	$Q$	1 or 3
	Freq. Shifts for Doppler Branches	$\{f_x\}$	0 or -0.75, 0, 0.75

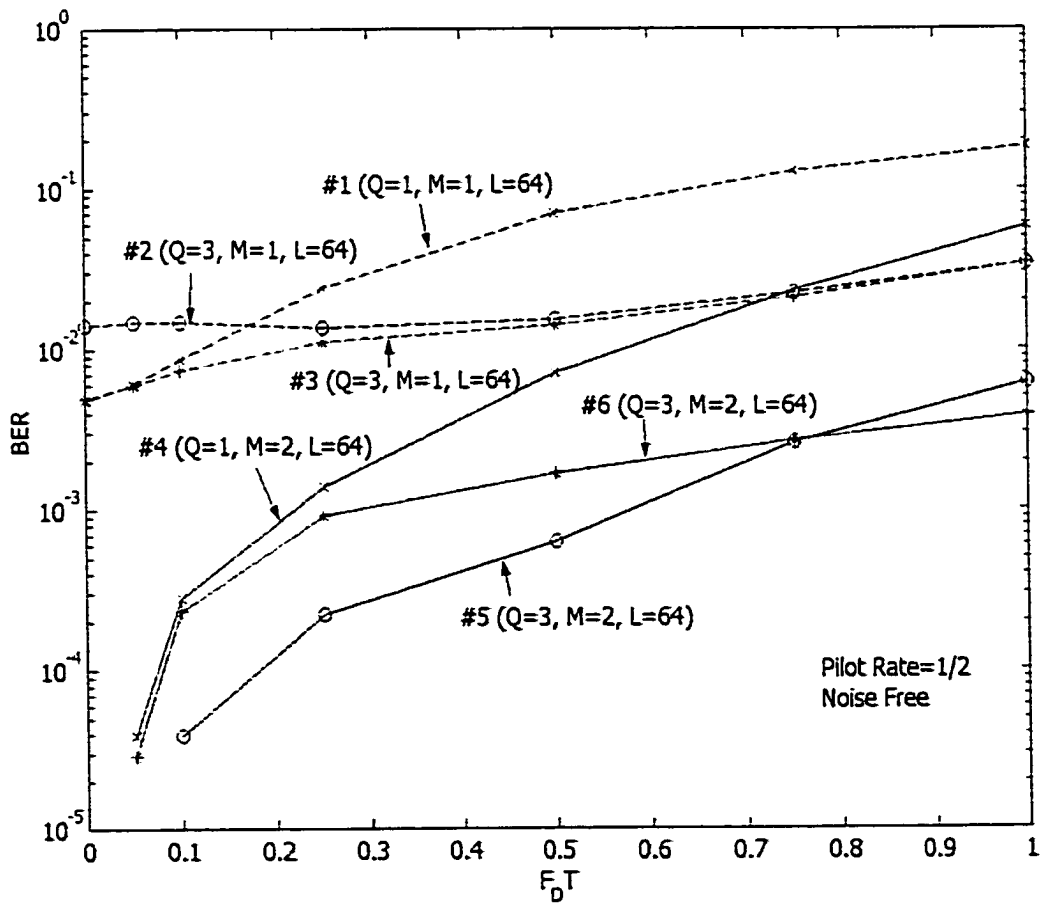


Figure 3.5 BER for 6 STFP configurations



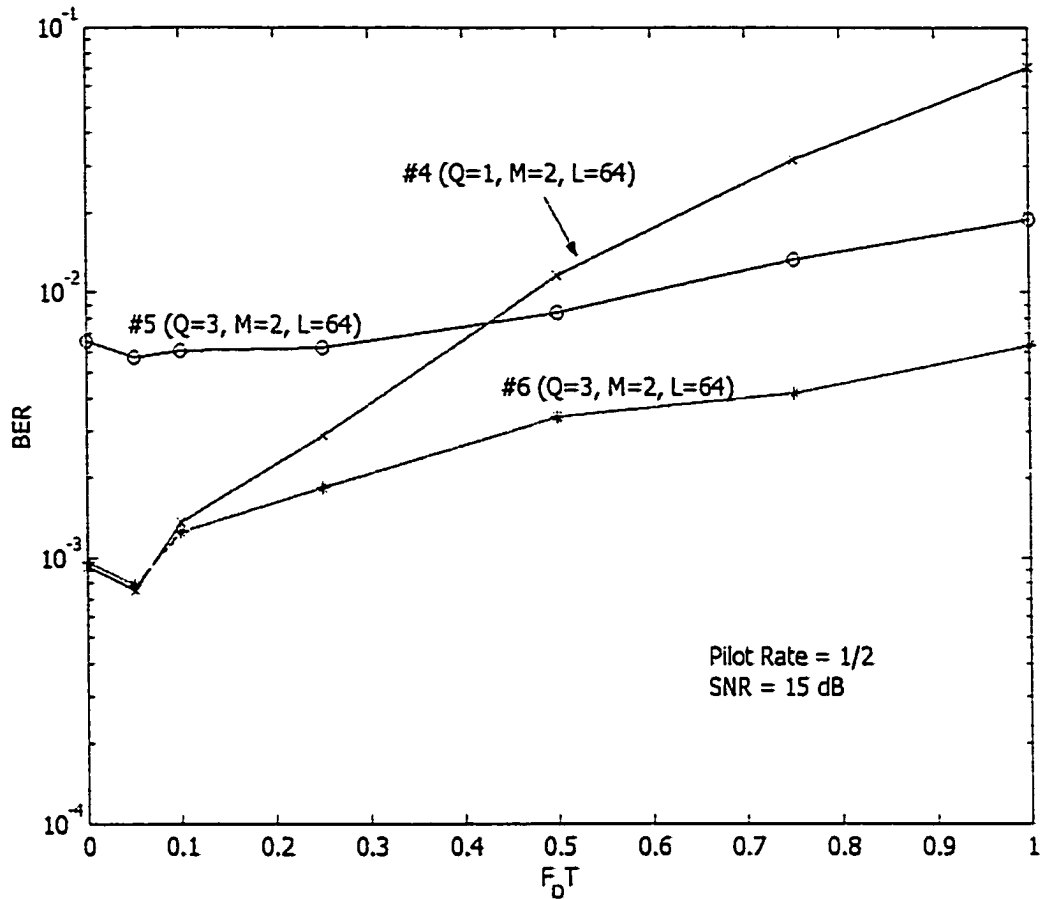


Figure 3.6 BER for 3 STFP configurations at 15 dB SNR

### 3.3.3. BER for Various STFP Configurations (With Noise)

The BER performances presented in the previous section are under noise free situation. In this section, they are re-evaluated under with-noise condition. The BER performances of three two-antenna configurations (#4, #5 and #6) are shown in Figure 3.6. The parameters used in this simulation is the same as those listed in Table 3.2 except that the signal to noise ratio (SNR) for Figure 3.6 is 15 dB. Generally, performances with Doppler diversity are much better than those without. The advantages of using Doppler diversity are more profound under high mobility (i.e., large  $F_D T$ ) conditions. However, there is an abnormality in our simulation results. As shown in Figure 3.6, the single-summation STFP (#5) result is much worse than the double summation STFP result when  $F_D T$  below 0.5. Moreover, it is also worse than the conventional space-time processing (#4, without Doppler diversity). This

abnormality is due to the following several reasons. At first, in single-summation STFP scheme, the weight coefficients are computed from  $MQL \times MQL$  sample correlation matrix and its inversion [3]. In order to make the  $MQL \times MQL$  sample correlation matrix invertible, the number of sample snapshots to be averaged,  $K$ , in (3.25) should be in practice several times greater than the rank of matrix,  $MQL$ . Furthermore, as mentioned previously, sample average method for correlation estimation is not optimum because signal samples are not stationary in our systems. Finally, low pilot rate reduce effective number of independent samples used in correlation estimation. In this simulation, the pilot rates are  $1/2$ ,  $N$  is 1024, and  $MQL$  is  $2 \times 64 \times 3 = 384$ . Therefore, it is equivalent to using at most 512 independent samples (pilots) to estimate 384-ranked sample correlation matrix. Thus, though the estimated correlation matrix is invertible, the estimation error is not small. To remedy this difficulty, one may think of increasing the number of samples. However, this approach will not always work because the statistics of samples are not stationary. The alternative remedy is to adopt the space-time processing techniques [4-6] developed in radar technology for detecting moving objects. In order to concentrate on our main idea, we will not discuss this problem further detail, and will examine more on the properties of double-summation STFP, which require less samples and is more stable than the single summation technique.

### 3.3.4. Improvement of Signal to Interference Ratio

Simulations depicted in Figure 3.7 are carried out to study the signal to interference ratio (*SIR*) improvement for the double summation STFP with different configurations. Here, the interference refers inter-carrier interference (ICI) in OFDM systems. As shown in Figure 3.7, a center subcarrier is separated from all other subcarriers before transmission. The two waveforms containing the center subcarrier and the other subcarriers, respectively, are transmitted through exactly the same time-varying multipath channel and detected by the same receiver separately. The two output powers for these two detections are then used to compute the instantaneous *SIR* for the particular center subcarrier. The instantaneous *SIR* is averaged over a large number of independent trials to obtain the averaged *SIR*.

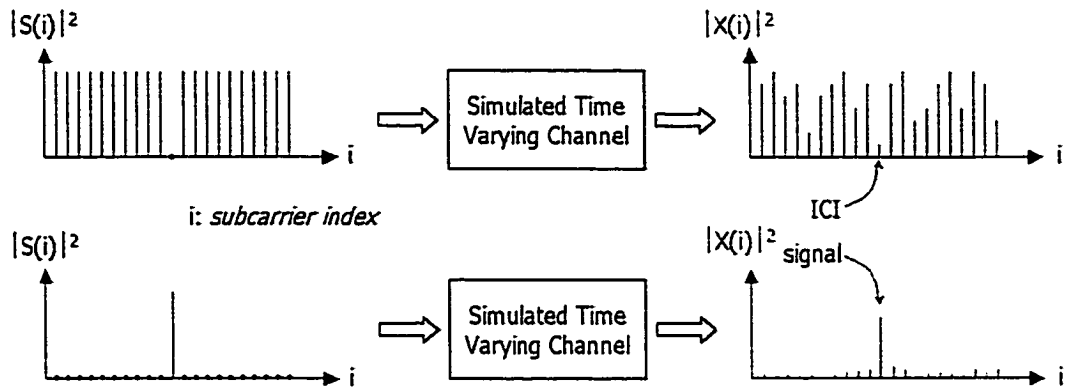


**Figure 3.7** Simulation for deriving signal to ICI power ratio

Consider the noise free condition first. Let angular spreads be uniform from 0 degree to 180 degree. In Figure 3.8,  $SIR$  versus  $F_D T$  curves for the case of  $M=1, 2$ , and 3 and  $Q=1$  and 3 are shown. Parameters used for simulations are listed in Table 3.3. For the same number of antennas, The  $SIR$  of STFP cases ( $Q=3$ , with Doppler Diversity) is higher than that of STP cases ( $Q=1$ , without Doppler diversity). The differences between STFP and STP cases increase as  $M$  increases or as  $F_D T$  increases. For the same number of Doppler branches (either  $Q=1$  or  $Q=3$ ),  $SIR$  increases as  $M$  increases. The increment of  $SIR$  as  $M$  increases is much larger than the increment of  $SIR$  as  $Q$  increases. This increment slightly decreases as  $F_D T$  increases. Using the single antenna system as the reference, the array gains are approximately 3dB and 6dB for 2 and 4 antenna systems, respectively. However, the  $SIR$  gains are around 10 dB and 15 dB for 2 and 4 antenna systems, respectively. The improvement of  $SIR$  using STP or STFP is remarkable. This is because STP can suppress or cancel out the most “harmful” wave arrivals by placing the nulls of its beam pattern at the directions of these harmful waves. The effects of FP (Doppler diversity) are less on increasing  $SIR$  than on changing the signal distribution. This has been shown in Chapter 2 and will be discussed further in the next section.

The effectiveness of STP on  $SIR$ , and consequently BER, improvements can be reduced when the angular spreads are small. In Figure 3.9, BER versus  $F_D T$  for the double-summation STFP are shown. Each curve represents the simulation results for a

**Table 3.3** Simulation parameters for deriving the results in Figure 3.8

	PARAMETER	ABBREV.	VALUE
Channel	Number of Paths	$N_p$	128
	Maximum Delay Spread	$D_{max}$	$8T_s$
	Type of Delay Spread		Uniform
	Type of Doppler Spectral Density		Uniform
	Range of Angular Spread		$0 - 180^\circ$
	Types of Angular Spread		Uniform
	Signal to Noise Ratio	$SNR$	15
Receiver	Number of Subcarriers Per Symbol	$N$	512 (464 active)
	Pilot Ratio	$\gamma_p$	1
	Number of Time-Taps	$L$	32
	Number of Antennas	$M$	1, 2, or 4
	Number of Doppler Channels	$Q$	1 or 3
	Freq. Shifts for Doppler Branches	$\{f_x\}$	0 or -0.75, 0, 0.75

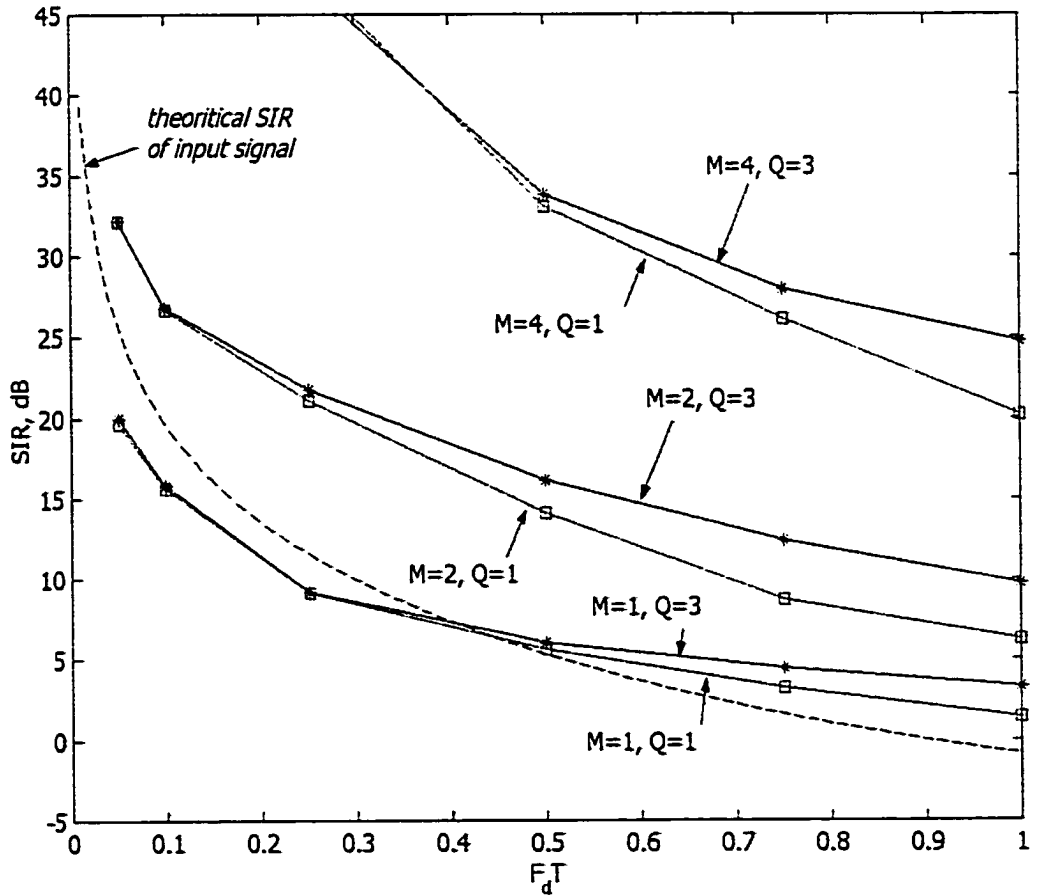


**Figure 3.8** SIR for 3 different double-summation STFP at 15 dB SNR

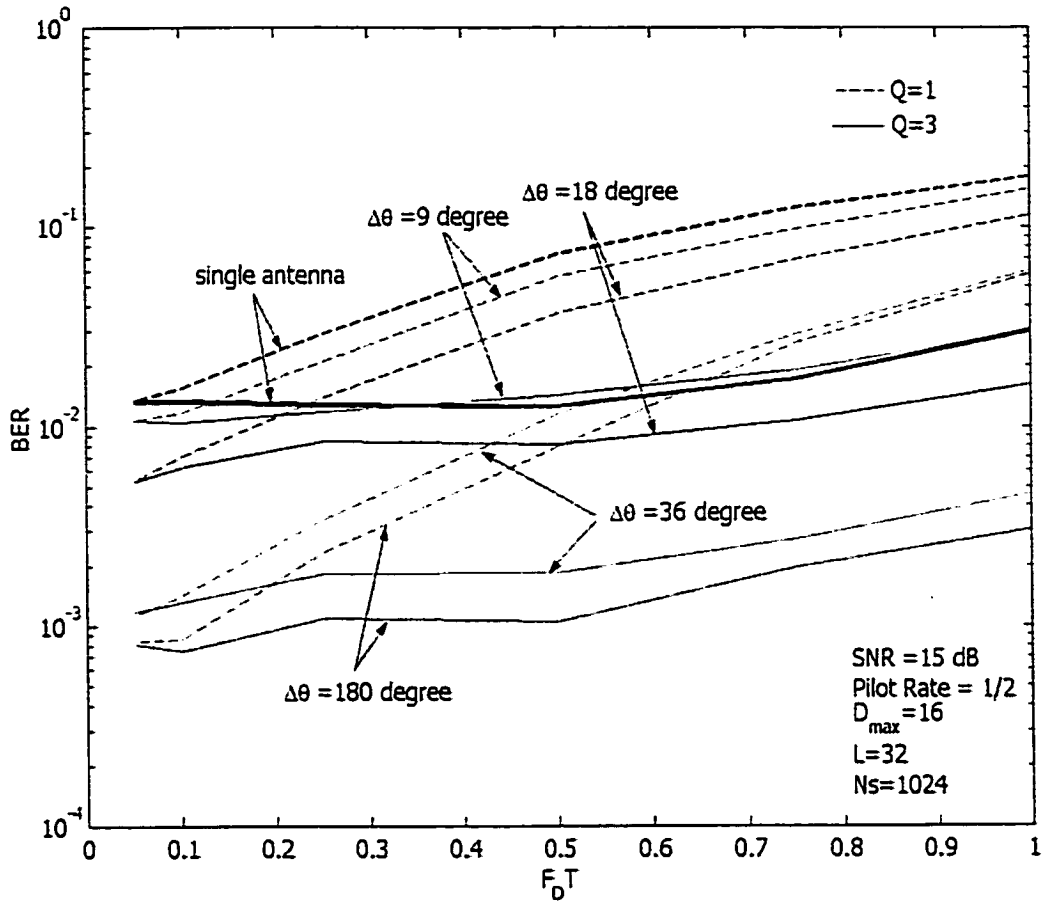


**Figure 3.9** BER performances for different angular spreads

particular set of angular spread  $\Delta\theta$ , the number of antennas  $M$ , and the number of Doppler branches  $Q$ . When  $\Delta\theta$  is less than  $18^\circ$ , BER performances of the 2-antenna systems are only slightly better than those of the single-antenna systems.

### 3.4. Time Domain Doppler Diversity (Time Frequency Processing)

In the frequency domain Doppler diversity system (i.e., frequency processing (FP)), it was shown in Chapter 2 that diversity gain is due to differences in the channel responses among different Doppler branches. Such effects are also found in the time domain Doppler diversity system (i.e., time-frequency processing (TFP)), which is a special case of STFP with single antenna. Consider the decision variable  $Z(i)$  which is the output of the matched filter of the double-summation STFP configuration in Figure 3.2. Here,  $Z(i)$  contains the desired signal component, ICI component and noise component. Because subsymbols are BPSK modulated, the sign of the desired signal component is that of the transmitted data subsymbol,  $d_i$ , where  $i$  denotes the  $i^{\text{th}}$  subsymbol. Let  $M=1$ , then the STFP is reduced to TFP. The histograms of  $Z(i)/d_i$  derived from 5000 trials is shown in Figure 3.10 and the parameters used for simulation are summarized in Table 3.4. The histograms of the desired signal component and the noise plus ICI components are shown in Fig. 11. At  $F_D T=0.25$ , the histograms of  $Q=1$  and  $Q=3$  are very similar to each other, and the effect of Doppler diversity is very small (BER's are 0.0323 for  $Q = 1$ , and 0.0176 for  $Q = 3$ ). However, at  $F_D T=0.75$ , the effect of Doppler diversity on change of signal histograms is profound. The probability for  $Z(i)/d_i > 0$  when  $Q=3$  is much larger than that when  $Q=1$  (BER's are 0.1400 for  $Q = 1$ , and 0.0288 for  $Q = 3$ ). This explains the reason why time-domain Doppler diversity (TFP) improves BER performances when  $F_D T$  is large. This mechanism is very similar to that for the frequency domain Doppler diversity (FP, shown in Figure 2.6). However, the centers of the histograms in Figure 2.6 are near zero while the centers of histograms in Figure 3.10 is near one. The additional time processing (TP) in TFP has moved the distribution of  $Z(i)/d_i$  toward the right hand side. Therefore, the BER performance of TFP is better than that of FP.

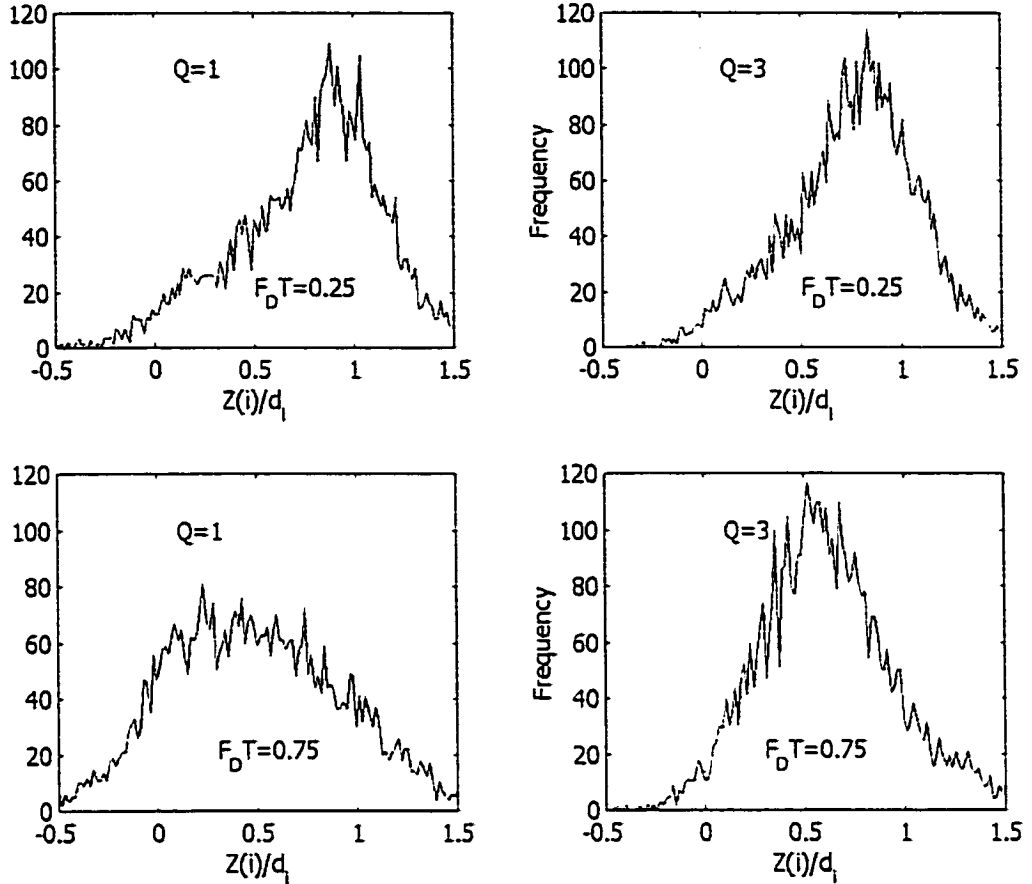
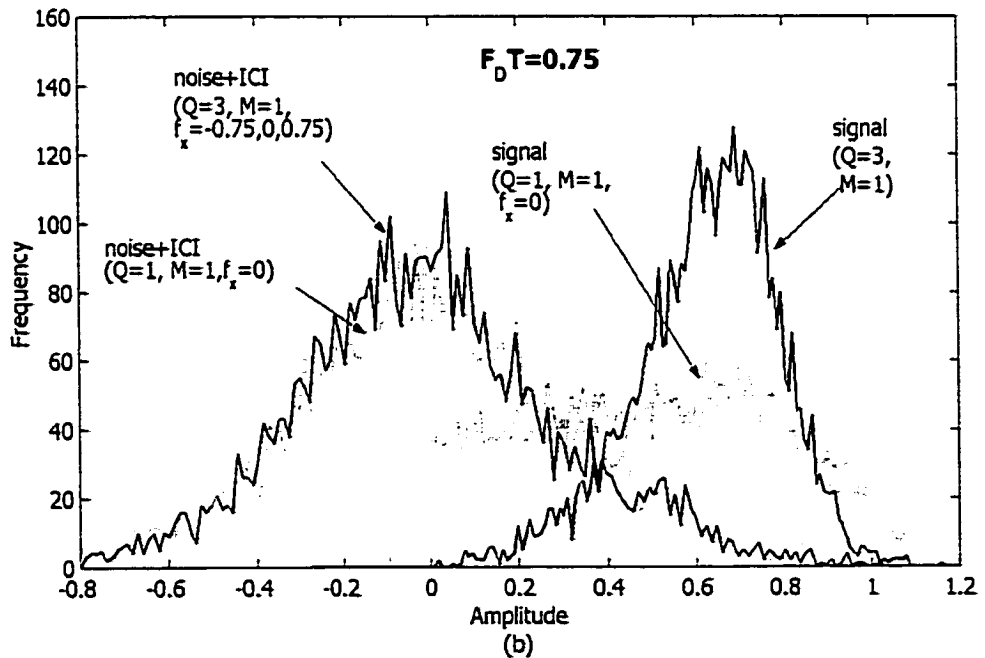
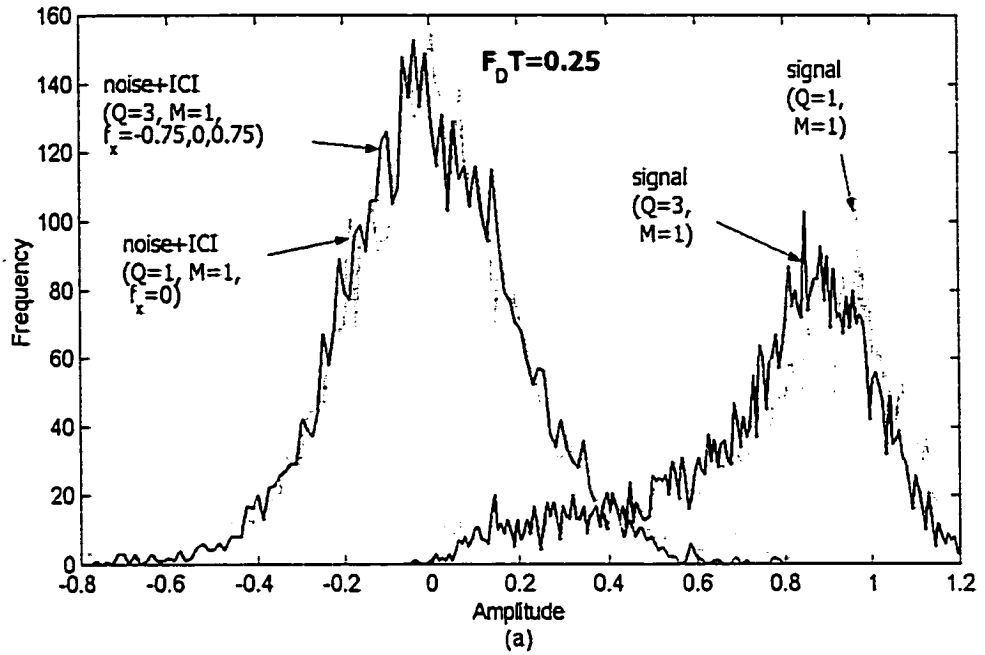


Figure 3.10 Histograms for the receiver output of time domain Doppler diversity

Table 3.4 Simulation parameters for deriving the results in Figure 3.10

	PARAMETER	ABBREV.	VALUE
Channel	Number of Paths	$N_p$	128
	Maximum Delay Spread	$D_{max}$	$16T_s$
	Type of Delay Spread		Uniform
	Type of Doppler Spectral Density		Uniform
	Signal to Noise Ratio	$SNR$	15
Receiver	Number of Subcarriers Per Symbol	$N$	512 (464 active)
	Pilot Ratio	$\gamma_p$	1/2
	Number of Time-Taps	$L$	32
	Number of Antennas	$M$	1
	Number of Doppler Channels	$Q$	3
	Freq. Shifts for Doppler Branches	$\{f_x\}$	0 or -0.75, 0, 0.75



**Figure 3.11** Histograms for the desired signal and the noise plus ICI for cases with ( $Q=3$ ) and without ( $Q=1$ ) Doppler diversity.



### 3.5. Conclusions

In this chapter, based on the novel Doppler diversity discussed in Chapter 2, we propose novel space-time-frequency processing (STFP) schemes for OFDM communications systems. Two structures are investigated: single-summation and double-summation STFP. Optimum weights are computed using the MMSE criterion in both structures. Through the simulations, it has been shown that both STFP structures can provide significant improvements in BER performance. The single-summation STFP has the potential to provide the optimum performance, yet the double-summation STFP is less complex. The required complexity for the double-summation STFP is  $O(M^2L^3)$ , while that for the single-summation STFP is  $O(Q^3M^2L^3)$ . Moreover, the double-summation STFP is more reliable than the single-summation STFP because the number of samples needed for estimating the correlation matrix in the double-summation STFP is only several  $ML$ 's, while that for single-summation STFP is several  $QML$ 's. In practice, the number of available samples is often sufficiently large for the double-summation STFP but may not be sufficient for the single-summation STFP.

STFP with multiple antennas outperforms TFP (with single antenna) if there are enough pilot samples available for estimating the correlation matrix and the angular spreads are large enough. When the angular spread is small, multiple antennas may not be able to provide space diversity. It has been reported that the angular spreads measured in urban and suburban area are very likely within  $9-25^\circ$  [7]. In such cases, Doppler diversity is more effective than the space diversity if Doppler spread is large.

In the OFDM systems, Doppler spreads produce ICI, which is the dominant performance degradation factor. The higher the Doppler effect is, the worse the BER performance becomes. Fortunately, for the various proposed Doppler diversity schemes, the higher the Doppler effect is, the larger the diversity gain grows to be. Therefore, the various Doppler diversity schemes proposed in Chapters 2 and 3 are relevant to OFDM-related systems. In fact, the proposed STFP schemes are very general and are not limited to OFDM systems. With proper modifications, they can be applicable to other types of communication systems such as DS-SS-CDMA.

## References

- [1] A.J. Paulraj and C. B. Papadias, "Space-time Processing for wireless communications," *IEEE Signal Processing Magazine*, pp. 49-83, November 1997.
- [2] John G. Proakis, *Digital Communications*, 3rd ed., New York: McGraw-Hill, pp.777-795, 1995.
- [3] S. U. Pillai, *Array Signal Processing*, New York: Springer-Verlag New York Inc., 1989.
- [4] J. Ward, *Space-Time Adaptive Processing for airborne Radar*, Technical Report 1015, MIT Lincoln Laboratory, Lexington, MA, December 1994.
- [5] S. U. Pillai, J. R. Gerci and Y. L. Kim, "Generalized forward/backward subaperture smoothing techniques for sample starved STAP," *IEEE Trans. on Signal Processing*, Vol. 48 No. 12, pp. 3569 –3574, December 2000.
- [6] Alex B. Gershman, George V. Serebryakov and Johann F. Bohme, "Constrained Hung-Turner adaptive beam-forming algorithm with additional robustness to wideband and moving jammers," *IEEE Trans. on Antennas and Propagation*, Vol. 44 No. 3, pp. 361 – 367 March 1996.
- [7] Cheolhang Cheon, George Liang and Henry L. Bertoni, "Simulating radio channel statistics for different building environments," *IEEE Journal on Selected Areas in Communications*, Vol. 19, No. 11, pp. 2191-2200, November 2001.

# Chapter 4

## Underwater Acoustic Channel Simulator for Broadband Communication Systems

### 4.1. Introduction

New technologies for establishing high-capacity communication links are universally in great demands. In order to satisfy the hunger of higher and higher data rates, newer communication systems are compelled to use broader bandwidth and achieve higher bandwidth efficiency. This trend appears in the development of both radio and underwater communication industries. However, broader bandwidth does not always be available in underwater acoustic (UWA) environments. Neither can it always bring along higher bandwidth efficiency.

UWA channels are far too complex, noisy and unpredictable to be tackled by simple communication schemes. First, due to inhomogeneity and time variations of channel characteristics, UWA signals usually exhibit strong temporal and spatial fluctuations in both amplitude and phase. Secondly, compounded by delay spread in propagation and other frequency-dependant factors such as absorption and boundary interactions, UWA signals also suffer from significant frequency-selective fades. In other words, in terms of the time domain description, UWA signals usually show severe weakening in strength and distortion in shape

after certain distances of propagation. Finally, there exist many non-stationary, non-white noises in underwater environments. These highly space, time and frequency dependent features pose numerous obstacles for establishing reliable UWA communications. The effects of these features determine the ultimate limits of the available channel bandwidth, practical distance and/or data rate for underwater communications.

Several broadband underwater communication systems have been proposed recently to increase the data rate. Yet, performance evaluations of such systems are very difficult to attain. They cannot be achieved through analytical means because the systems and the environments involved are far too complex. Neither can they be obtained conveniently from experiments because sea test is usually very costly and ineffective. Furthermore, the results obtained in one sea test cannot be extended to other cases easily. It seems that, if a good acoustic channel simulator is available, numerical simulation is the most economical and effective tool for system design and development and for performance prediction and assessment. Therefore, development of a broadband channel simulator is crucial to the growth of UWA communication technologies.

Different underwater channel simulators have been proposed during recent decade [1-5]. In [1] and [2], stochastic fading simulators are developed to generate diffused components of multipath propagation channel. The fading is Rayleigh distributed in these models. In [3], derived from experimental results, a generalized propagation model is developed to simulate acoustic channel with non-Rayleigh fading. In [4], the spectral characteristics of fluctuations of channel characteristics are studied in numerical simulation. In [5], a framework using a minimum-phase filter and an all-pass filter to represent the response of each eigenray is proposed. One thing in common in these different simulators is that they employ complex

*amplitude modulators* to generate fluctuation of channel characteristics while key channel parameters such as propagation loss are kept constant for the entire signal frequency band. Therefore, they are suitable only for simulating narrowband systems, in which the variation of propagation delay can be represented as the variation of carrier phase shift. However, since various loss mechanisms and many time variation factors such as Doppler shift and spread are frequency dependent, a broadband simulator has to account for these effects in addition to other broadband features.

In this paper, a novel physics-based broadband channel simulator is developed. The ray model used in [5] is adopted to describe the relationship between source motion and channel impulse response. However, instead of using the conventional *amplitude-modulator* approach, we develop a novel *frequency-modulator* approach, in which the variations of propagation delays are directly accounted for. For a time-harmonic input, the time variations in the UWA channel are transformed into the carrier *frequency* shifts in our approach but into phase shift in conventional approaches. Although the same time-harmonic result is obtained from these two different models, physical mechanisms are very different. This difference is manifested when multiple frequencies are considered. For a broadband input, frequency-dependent Doppler effects in the UWA channel can be accounted for by the proposed frequency-modulator (but not by the amplitude-modulators [1-5]). In a recent publication [6], time-scaling technique is used to model the frequency-modulator effect, and a poly-phase filter bank is proposed to implement these time-scaling effects. Using a shallow water channel as an example, time and frequency characteristics of a broadband orthogonal frequency division multiplexing (OFDM) signal with spectrum ranged from 8 to 11 kHz are simulated. The simulation results are very similar to the experimental results [7].

## 4.2. Underwater Acoustic Channel Model

Taking into consideration various physical mechanisms of acoustic propagation, a UWA channel is modeled as a time varying filter with additive noises as shown in Figure 4.1. The received signal  $r(t)$  can be represented as

$$r(t) = s(t) * h(t, \tau) + v(t) \quad (4.1)$$

where  $s(t)$  is the transmitted signal,  $h(t, \tau)$  is the time-varying channel impulse response and  $v(t)$  is the additive colored noise. Time variation of channel impulse response is due to changes of source location, receiver location and/or environmental parameters. The main noise sources are ambient noise and self-noise. The noise spectrum is usually not white and may have very different characteristics under different conditions.

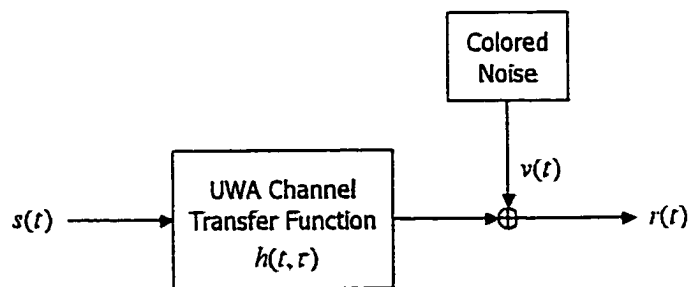
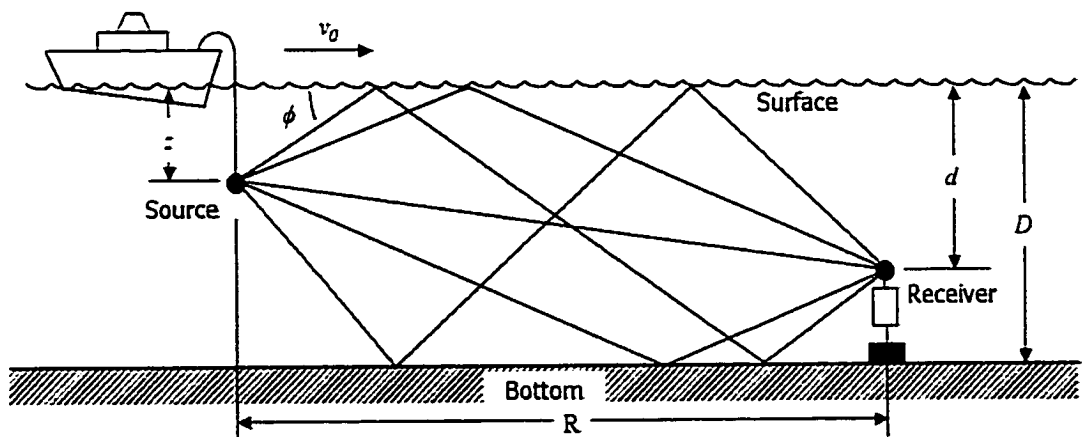


Figure 4.1 Underwater acoustic channel configuration

Since a typical UWA channel is a good acoustic waveguide, the received signal can be expressed as the superposition of a finite number of dominant eigenrays arriving from different paths. The channel impulse response can therefore be constructed as a sum of impulse responses of eigenrays, and the problem of determining the channel impulse response is reduced to the task of determining the impulse response for each relevant eigenray path. Given the system layout and environment parameters such as the sound velocity profile, bottom type and sea state, parameters of each relevant eigenray may be computed by means of a ray trace program. The impulse response of each eigenray path can be modeled by a minimum-phase system connected to an all-pass system [5]. Thus,

$$h(t, \tau) = \sum_{n=1}^{N_p} h_{M_n}(t, \tau) * h_{A_n}(t, \tau) \quad (4.2)$$

where  $N_p$  is the number of relevant eigenrays. For the  $k^{\text{th}}$  eigenray,  $h_{M_k}(t, \tau)$  is a minimum-phase system reflecting the frequency dependent path gain and  $h_{A_k}(t, \tau)$  is an all-pass system modeling the time-varying propagation delay. Without loss of generality, we will investigate these systems using a simplified isospeed channel model shown in Figure 4.2.



**Figure 4.2** A simplified isospeed channel model

### 4.2.1. All-pass system

The all-pass system for the  $k^{\text{th}}$  path is characterized by its time-dependent delay  $\tau_k(t)$  and is represented by

$$h_{A_k}(t, \tau) = \delta\{\tau - \tau_k(t)\}, \quad (4.3)$$

where  $\delta(\tau)$  is the Dirac delta function. If the sound speed  $c$  is a constant over the entire path, propagation delay  $\tau_k(t)$  can be represented by

$$\tau_k(t) = \frac{L_k(t)}{c} \approx \tau_{0_k} - \frac{1}{c} \int_{t_0}^t \bar{v}(\zeta) \cdot \bar{l}_k d\zeta \quad (4.4)$$

where  $L_k(t)$  is the path length for the  $k^{\text{th}}$  eigenray,  $\tau_{0_k} = L_k(t_0)/c = \tau_k(t_0)$  is the reference delay at time  $t_0$ ,  $\bar{v}(t) \cdot \bar{l}_k$  is the dot product of the source velocity vector and the unit trajectory vector along the  $k^{\text{th}}$  eigenray path at source. In practice, instantaneous path length is a function of both deterministic and random factors. These factors are functions of source and sensor velocities, motions of reflecting boundaries and sound speed profile. Such factors create fluctuations in propagation delay and cause Doppler spread. Therefore, it is convenient to express  $\tau_k(t)$  in terms of a mean delay (corresponding to an effective source velocity  $v_0$ ) and an effective zero-mean fluctuation  $\xi_k(t)$ . Equation (4.4) becomes

$$\tau_k(t) = \tau_{0_k} - \frac{v_0 \cos \phi_k}{c} (t - t_0) - \frac{1}{c} \int_{t_0}^t \xi_k(\zeta) d\zeta, \quad (4.5)$$

where  $\phi_k$  is the elevation angle of the eigenray and  $v_0 t \cos \phi_k + \xi(t) = \bar{v}(t) \cdot \bar{l}_k(t)$ . Note that the delay fluctuation  $\xi_k(t)$  contains all effective fluctuations due to motion of source,



receiver, reflecting boundaries, etc. In many cases, delay fluctuations for different eigenrays are highly correlated because the variation of system geometry, which is the major cause of delay fluctuation in our model, affects almost all eigenrays.

#### 4.2.2. Minimum-Phase System

Frequency dependent path gain can be modeled by a minimum-phase system, which is characterized by its frequency response  $|H_{M_i}(f)|$ . Major factors affecting path gain are spreading, absorption and boundary reflection losses. Since these factors do not vary rapidly in time, they can be modeled as time-invariant systems.

Spreading loss is a geometrical effect representing the weakening of a sound signal as it propagates (and spreads) outward from the sound source. The loss is a function of distance and depends on the spreading type. Assuming a cylindrical spreading, we use a commonly used factor,  $10\log L$ , as the spreading loss factor in our path gain calculation.

Absorption loss is due to the conversion of acoustic energy into heat in the propagation medium, which is both frequency and distance dependent. There are various empirico-theoretical expressions for absorption models. Among them, we choose Fisher-Simmons loss curve (see [8][9]) that models frequency dependence of absorption loss for seawater constituents such as boric acid and magnesium sulfate, and viscosity. Figure 4.3 shows an absorption loss curve generated by a 9<sup>th</sup> order polynomial equation and approximated by the least square method.

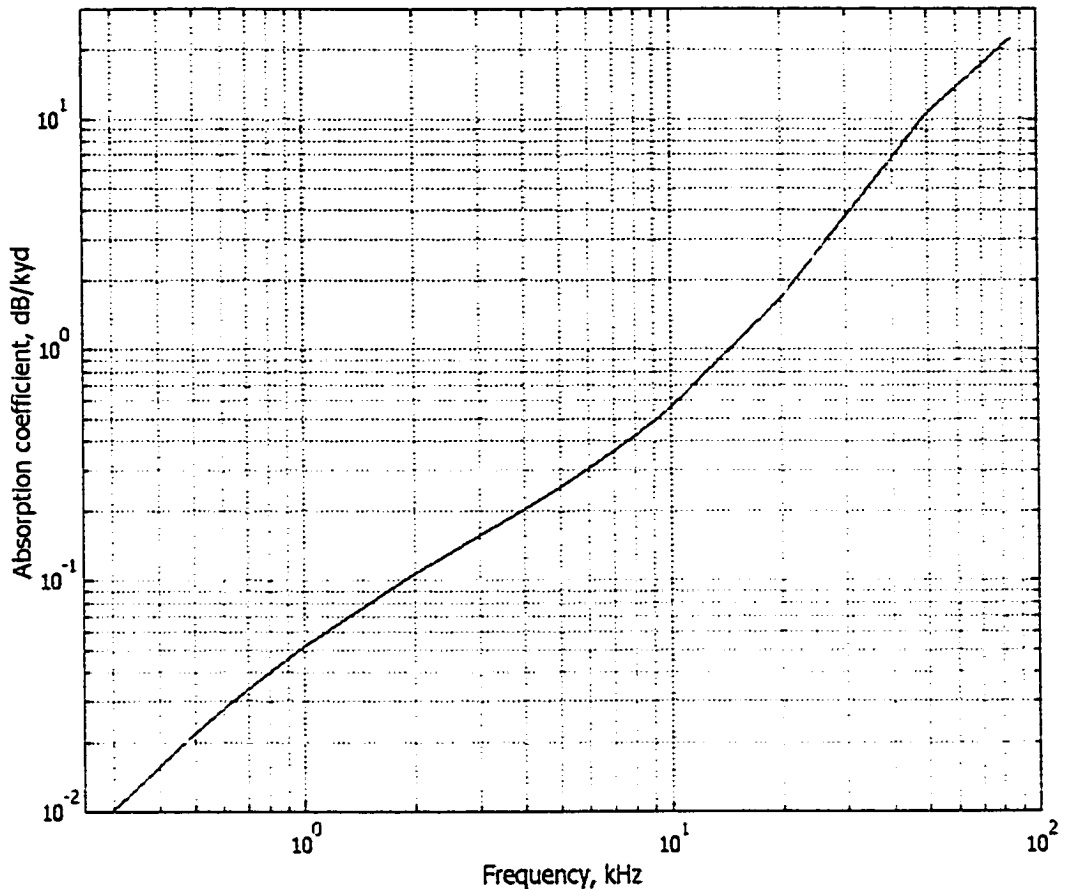


**Figure 4.3** Absorption coefficient vs. frequency at  $S=35$  ppt,  $pH=8$ , depth zero and temperature of  $20$  °C. The curve is plotted using a 9<sup>th</sup> order polynomial equation approximating the Fisher-Simmons absorption loss in [8].

The most complex loss factor for an eigenray is the attenuation at sea surface and/or bottom. It depends on frequency, grazing angle, roughness of surface or bottom, and bottom types. A simple empirical formula for the surface reflection loss coefficient could be found in [10][11]:

$$\mu = 10 \log\left(\frac{1 + (f/f_1)^2}{1 + (f/f_2)^2}\right) - (1 + (90 - w)/60) \cdot (\phi/30)^2 \quad (4.6)$$

where  $\mu = 10 \log(I_2/I_1)$  is the logarithmic ratio of reflecting-wave intensity  $I_2$  to incident-wave intensity  $I_1$ . Here,  $w$  is the wind speed in knots,  $\phi$  is the incident angle in degree,  $f$  is

the acoustic wave frequency in kHz,  $f_1 = \sqrt{10} \cdot f_2$  and  $f_2 = 378 w^{-2}$ . The formula is 2dB less than comparing to the generic sonar model (GSM) model for the Beckman-Spizzichino loss.

For bottom reflections, since there exist too many types of bottom layered structure and material, a typical loss factor is very difficult to obtain. However, since grazing angle is very small and less than the critical angle for most of the UWA channel geometry with large range to depth ratio, we consider the total reflection scenario in our simulation.

### 4.2.3. Additive Noise

Background noise in UWA channel can be decomposed into self-noise and ambient noise. Self-noise is generated from platform of the receiver, surface of sensor packages, and cables where the sensors are attached. The characteristics of self-noises differ from case by case.

Sources of ambient noise are shipping, surface wave, biological noise, thermal noise, etc. These noises show different behaviors and characteristics at different conditions. Fortunately, for a few to several tens of kHz range, spectral slopes of  $-5$  to  $-6$  dB per octave or about  $-17$  dB per decade are most common [9]. In this study, for simplicity, we do not separate self-noise and ambient noise. A  $-5$  dB per octave slope is employed in our simulation.

## 4.3. Implementation of Channel Response

The key characteristics of channel simulators are examined in details and design procedures of each component are presented in this section. As discussed in Section II, each eigenray is modeled as a cascade combination of a spectral-shaping filter and a variable-delay all-pass

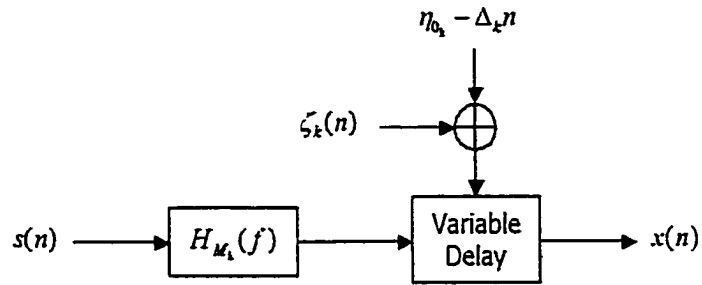


**Figure 4.4** Signal processing model for the channel transfer function.  $\Delta_k = v_0 \cos \phi_k / cT$ ,

$$\eta_{0_k} = \tau_{0_k} / T + t_0 v_0 \cos \phi_k / cT$$

filter (see Figure 4.4). The spectral shaping filter is approximated as a time invariant system, yet the all-pass system is time varying. Considering the additional delays in the all-pass systems, more freedom can be allowed for designing the spectral-shaping systems. The all-pass function is realized by combining both integer and fractional time shifts using a linear phase filter with a controllable phase response to obtain the appropriate time-varying delay. In such a manner, the time varying all-pass system generates frequency- dependent Doppler effect. This is one of the most important features of our broadband UWA channel simulator.

### 4.3.1. Doppler Effect and All-Pass System

Variations of propagation delays cause Doppler shifts and spreads in all frequency constituents of a broadband UWA signal. Consider one frequency constituent, a time-harmonic input  $e^{j2\pi f_0 t}$  with frequency  $f_0$ , as the input to the  $k^{\text{th}}$  all-pass filter. The output signal  $x_e(t)$  is expressed as

$$x_e(t) = e^{j2\pi f_0 t} * h_{A_k}(t, \tau) = \exp \left\{ j2\pi f_0 \left( t - \tau_0 + \frac{v_0 \cos \phi_k}{c} (t - t_0) + \frac{1}{c} \int_{\tau_0}^t \xi_k(\zeta) d\zeta \right) \right\} \quad (4.7)$$

The *instantaneous frequency*  $f_i(t)$  of the output signal  $x_e(t)$  is time derivative of the phase term in (4.7):

$$f_i(t) = f_0 \left( 1 + \frac{v_0 \cos \phi_k}{c} + \frac{1}{c} \xi_k(t) \right), \quad (4.8)$$

where  $f_0(v_0 \cos \phi_k + \xi_k(t))/c$  is the *instantaneous Doppler shift*. The *mean Doppler shift*  $f_{DM}$  and the *mean square Doppler spread*  $B_D^2$  are defined as

$$f_{DM} \equiv \int_{-\infty}^{\infty} f X_D(f) df, \quad B_D^2 \equiv \int_{-\infty}^{\infty} f^2 X_D(f) df - f_{DM}^2, \quad (4.9)$$

where  $X_D(f)$  is the Doppler spectrum [13]. In general, obtaining the Doppler spectrum  $X_D(f)$  from (4.7) is complicated since the integral in (4.7) is non-stationary and, in addition, frequency modulation is a nonlinear process. However, if the random fluctuation,  $\xi_k(t)$ , is a zero-mean stationary Gaussian random process,  $f_{DM}$  can be simplified using a similar technique in [14]. Details are shown in Appendix A. Thus, from (A.8), the mean Doppler shift,  $f_{DM}$ , is

$$f_{DM} = f_0 \frac{v_0 \cos \phi}{c} \quad (4.10)$$

and the *mean square Doppler spread*  $B_D^2$  and the *RMS (root-mean square) bandwidth* of Doppler spread  $B_D$  are

$$B_D^2 = \left( \frac{f_0}{c} \right)^2 \sigma_\xi^2, \quad B_D = \frac{f_0}{c} \sigma_\xi. \quad (4.11)$$

respectively. Note that equations (4-11) are derived for a single eigenray response only. Combining the effects of multiple eigenrays, the resulting  $f_{DM}$  and  $B_D$  increase because eigenrays with different elevation angles have different  $f_{DM}$ 's.

### 4.3.2. Realization of Time Varying All-Pass System

For a band limited input signal  $\tilde{s}_{BL}(t)$ , the all-pass system,  $h_{A_k}(t, \tau)$ , in (4.2) can be replaced by an ideal low pass filter,  $\tilde{h}_{L_k}(t, \tau)$ , with a time varying delay. Therefore, the output signal  $\tilde{x}_{BL}(t)$  can be represented by

$$\tilde{x}_{BL}(t) = \tilde{s}_{BL}(t) * \tilde{h}_{L_k}(t, \tau), \quad \tilde{h}_{L_k}(t, \tau) = \frac{\sin 2\pi f_L \{\tau - \tau_k(t)\}}{\pi \{\tau - \tau_k(t)\}} \quad (4.12)$$

Here,  $\tilde{h}_{L_k}(t, \tau)$  is an impulse response of the ideal low pass filter with  $f_L$  representing the cut-off frequency. In practice, a window function can be employed to control aliasing and to avoid Gibbs phenomenon near the cut-off frequency  $f_L$ . In the discrete time domain where the sampling interval  $T < 1/(2f_L)$ , the low pass impulse response in (4.12) is approximated as

$$h_{L_k}(n, m) \approx w(m - \tau_k(nT)/T) \frac{\sin 2\pi f_L T \{m - \tau_k(nT)/T\}}{\pi T \{m - \tau_k(nT)/T\}} \quad (4.13)$$

where  $w(m)$  is a window function and  $\{\tau_k(nT)\}$  is a set of discrete time delays. From (4.5),

$$\tau_k(nT) = \tau_{0_k} - \frac{v_0 \cos \phi_k}{c} (nT - t_0) - \zeta_k(nT), \quad \zeta_k(n) = \frac{1}{c} \int_{t_0}^{nT} \xi_k(\zeta) d\zeta \approx \frac{T}{c} \sum_n \xi_k(nT). \quad (4.14)$$

Integer-delays can be easily obtained by shifting the sample sequence or, equivalently, changing the sample index. On the other hand, fractional delays less than one sample period  $T$  have to be obtained by interpolation that can be implemented by a set of subfilters such as a polyphase filter bank [15]. Using the property of convolution, the filtering process in (4.12) can be represented by

$$x_{BL}(n) = s_{BL}(n) * \tilde{h}_{L_k}(n, m) = s_{BL}(n - q_k) * \tilde{h}_{L_k}(n, m + q_k) \approx s_{BL}(n - q_k) * g_{p_k}(n) \quad (4.15)$$

for  $q_k = \lfloor \tau_k(nT)/T + 0.5 \rfloor$  and  $p_k = \lfloor (\tau_k(nT)/T - q_k) \times M_p \rfloor$ , where  $s_{BL}(n) \equiv \tilde{s}_{BL}(nT)$ ,  $x_{BL}(n) \equiv \tilde{x}_{BL}(nT)$ , the notation  $\lfloor \tau \rfloor$  denotes the largest integer which does not exceed  $\tau$ ,  $M_p$  is the number of subfilters in the filter bank, and the  $i^{\text{th}}$  subfilter  $g_i(n)$  is

$$g_i(n) = w\left(n - \frac{i}{M_p}\right) \frac{\sin 2\pi f_L T \left(n - \frac{i}{M_p}\right)}{\pi T \left(n - \frac{i}{M_p}\right)}, \quad -\frac{M_p}{2} \leq i < \frac{M_p}{2}. \quad (4.16)$$

The number of subfilters,  $M_p$ , determines not only the precision of delay but also the noise power induced by approximation errors. Therefore, to select an optimum  $M_p$ , we need to compromise precision with other factors such as memory usage, quantization errors and maximum  $S/N$  requirement.

### 4.3.3. Generation of the Random Fluctuations

There are many physical mechanisms causing travel time fluctuations in underwater channels. They are too complex to be modeled analytically in a unified manner. Therefore, in this paper, we use a set of sea trial [16] data to extract required statistics of the fluctuation. In Figure 4.5, a set of typical instantaneous Doppler power spectra found in the experimental data is represented on the time-frequency plane. There were 4 tonal components of which the original frequencies are 8007.8, 8019.5, 10976.6 and 10988.3 Hz, respectively. They were superimposed onto an OFDM signal and then passed through a shallow UWA channel. Details of the signaling will be explained in Section 4.4. The distance between receiver and transmitter was about 3 km. Both transmitting and receiving platforms were stationary. Each of the tonal components is analyzed by the MVSE (minimum variance spectral estimation)

method [17] after being translated to the baseband and decimated. Consequently, the frequency axis represents Doppler frequency shift,  $f_D$ . The procedure is briefly described in Appendix B.

From Figure 4.5, we observe that Doppler shifts are proportional to their corresponding source frequencies, as represented in (4.8). Doppler spread is roughly in the order of a tenth of Hz. The time varying characteristics of the four tones are very similar to one another. They show similar traces of the spectral peaks in the time-frequency plane.

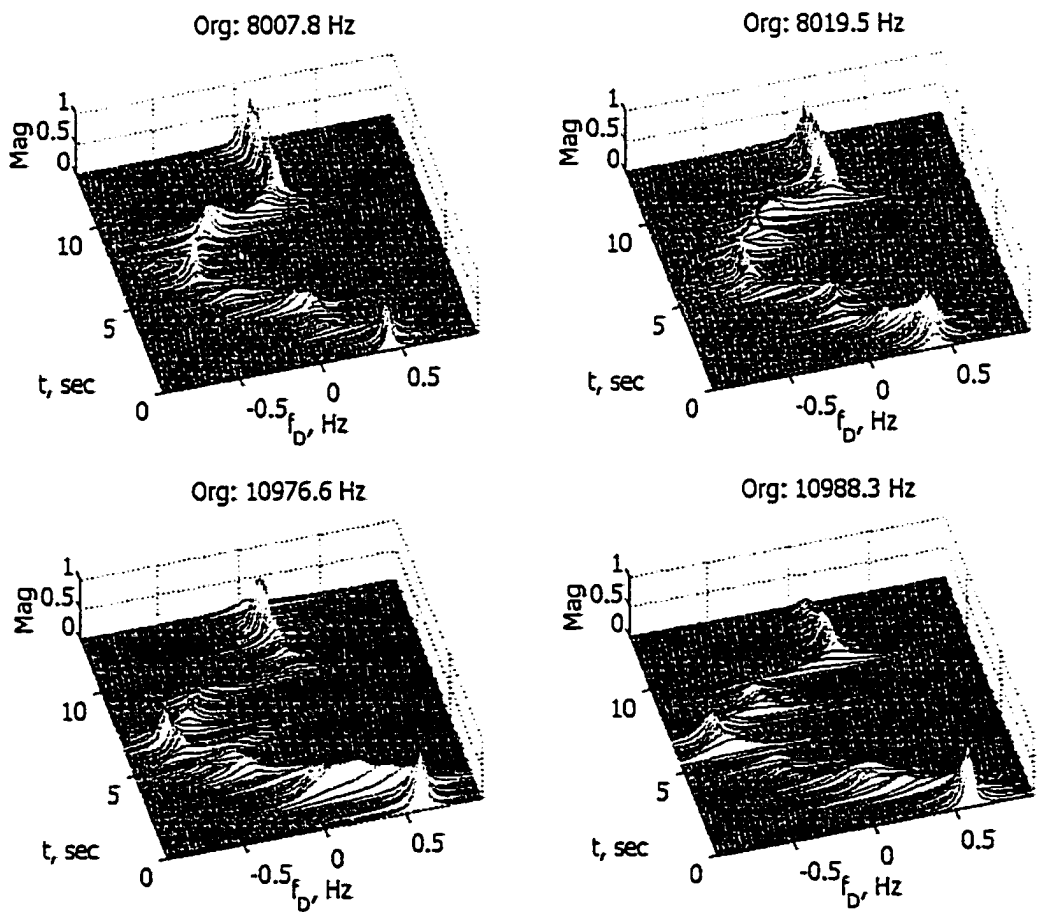


**Figure 4.5** Observation of Doppler effects in real data



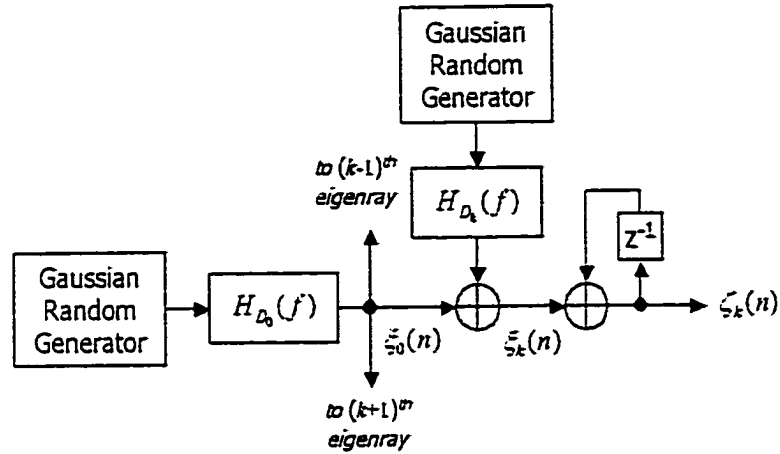


**Figure 4.6** Generation of random fluctuation of time delay for the  $k^{\text{th}}$  eigenray

Considering the fact that the received signal is a superposition of multiple eigenrays, it implies that the time fluctuations of various eigenrays are highly correlated. In order to obtain random but correlated random sequences  $\{\xi_k(n) \equiv \xi_k(nT)\}$  for generating random time fluctuations, two types of random number generators are employed (see Figure 4.6)

For each  $k$ ,

$$\xi_k(n) = a_k \xi_0(n) + \tilde{a}_k \tilde{\xi}_k(n) \quad (4.17)$$

where  $\xi_0(n)$  and  $\tilde{\xi}_k(n)$  are zero-mean Gaussian random variables with unit variance and the constants  $a_k$  and  $\tilde{a}_k$  are the designing parameters. The common random number  $\xi_0(n)$  supplies the dominant portion of time fluctuation,  $a_k \xi_0(n)$  for every eigenray. The  $k^{\text{th}}$  independent random number  $\tilde{\xi}_k(n)$  supplies the  $k^{\text{th}}$  eigenray its own independent time fluctuation,  $\tilde{a}_k \tilde{\xi}_k(n)$ . Accumulating in time the random number  $\xi_k(n)$  generates the delay fluctuation  $\zeta_k(n)$  of the  $k^{\text{th}}$  eigenray. As shown in Figure 4.5, since the frequency range of such fluctuations is far less than the sampling frequency, the integration in (4.14) can be

approximated by a summation. Furthermore, for the same reason, generation of the delay fluctuation  $\zeta_x(n)$  involves very high ratio of interpolation (see (4.15)).

#### 4.3.4. Realization of Spectral-Shaping Filters

In our loss model, the spectral-shaping filters in Fig. 4.4 are specified by path-gains of eigenrays. Therefore, these filters can be implemented in term of minimum-phase systems, which require only magnitudes responses.

As shown in Figure 4.7, the path gains for five eigenrays with various numbers of surface

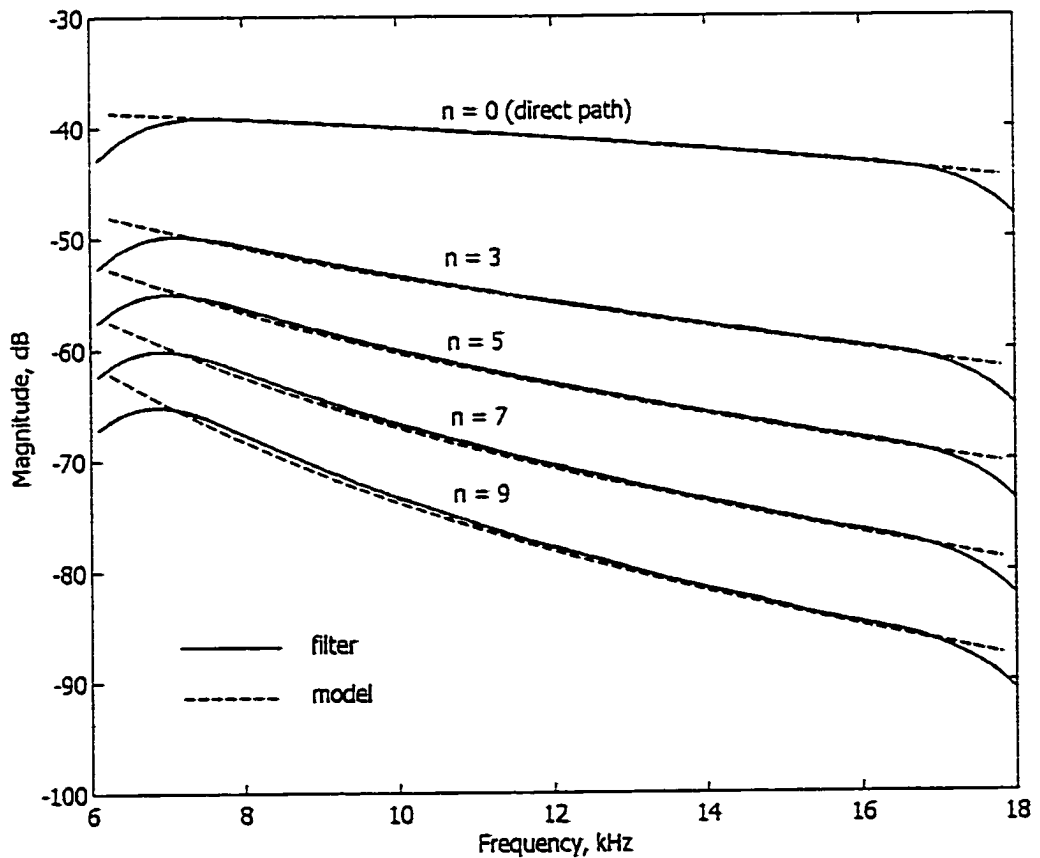


**Figure 4.7** Comparison of frequency responses between the theoretical model and the designed filter

reflections are compared with the corresponding filter responses designed by the window method [18]. In the figure, the variable  $n$  is the total number of interactions with boundaries (including both surface and bottom). For  $n = 0, 3, 5, 7,$  and  $9$ , the number of surface reflections is  $0, 2, 3,$  and  $5$ , respectively. The environment parameters employed in the simulation are: horizontal range of 5000 m, wind speed of 10 knots, bottom depth of 100 m, source depth of 10 m, receiver depth of 90 m and sound speed of 1460 m/s. The filters are designed to approximate path gains from 8 kHz to 16 kHz. The approximation error appeared in the figure is small.

#### 4.4. Simulation Results

The goal of this simulation is to generate signals with characteristics similar to those obtained from experiments. In this manner, the channel simulator can be claimed to characterize accurately the real underwater channel. The parameters used for a sample simulation is summarized in Table 4.1. As discussed in Section 4.2.2, the bottom reflection coefficients are approximated to be one and the surface reflection coefficients are computed using equation (4.6), which is a function of frequency and wind speed. The number of total eigenrays  $N_p$  is set to be 20 such that the power ratio of the weakest ray over the direct ray is about 0.1 %. Propagation delays and reception angles are calculated by the image method.

Both OFDM and sinusoids are applied to assess the performance of our simulator. Since the OFDM signal has almost flat power spectrum spanning the entire signal frequency band, it is used to exhibit broadband features of the simulator. The sinusoidal signals provide precise and quantitative descriptions for narrowband characteristics. Figure 4.8 shows the

signaling structure (four sinusoids and 754-subcarrier OFDM waveform). The total length of waveform is 14.952 sec. This waveform was used for sea trials [16]. The results of the sample simulation will be compared with the experimental data.

**Table 4.1** Simulation parameters

	PARAMETER	ABBREV.	VALUE
Channel	Bottom Depth	$D$	100 m
	Source Depth	$Z$	10 m
	Receiver Depth	$d$	90 m
	Horizontal Distance	$R$	5000 m
	Wind Speed	$w$	10 knots
	Sound Speed	$c$	1460 m/s
	Source Platform Speed	$v_0$	0, 10 knots
Signal	Sampling Frequency	$f_s$	48 kHz
	Frequency Span		8 kHz – 11kHz
	Format		OFDM, Sinusoidal

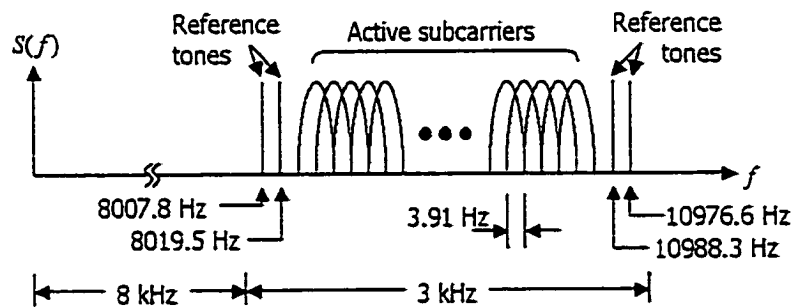


**Figure 4.8** Frequency domain representation of the OFDM signal and four sinusoids used for the sample simulation

### 4.4.1. Instantaneous Doppler Spectrum

The time variation of instantaneous Doppler spectra in sea trial data has been shown in Figure 4.5. We intended to control the spectrum of random processes  $\{\xi_k(n)\}$  for every  $k$  so as to generate similar results to those shown in Figure 4.5. For this simulation, the standard deviation  $\sigma_k$  of  $\xi_k(n)$ , for every  $k$ , was set to be  $2.5 \times 10^{-5} \times c$  to make RMS bandwidth of Doppler spread to be approximately 0.2 Hz at 8 kHz and 0.275 Hz at 11 kHz.

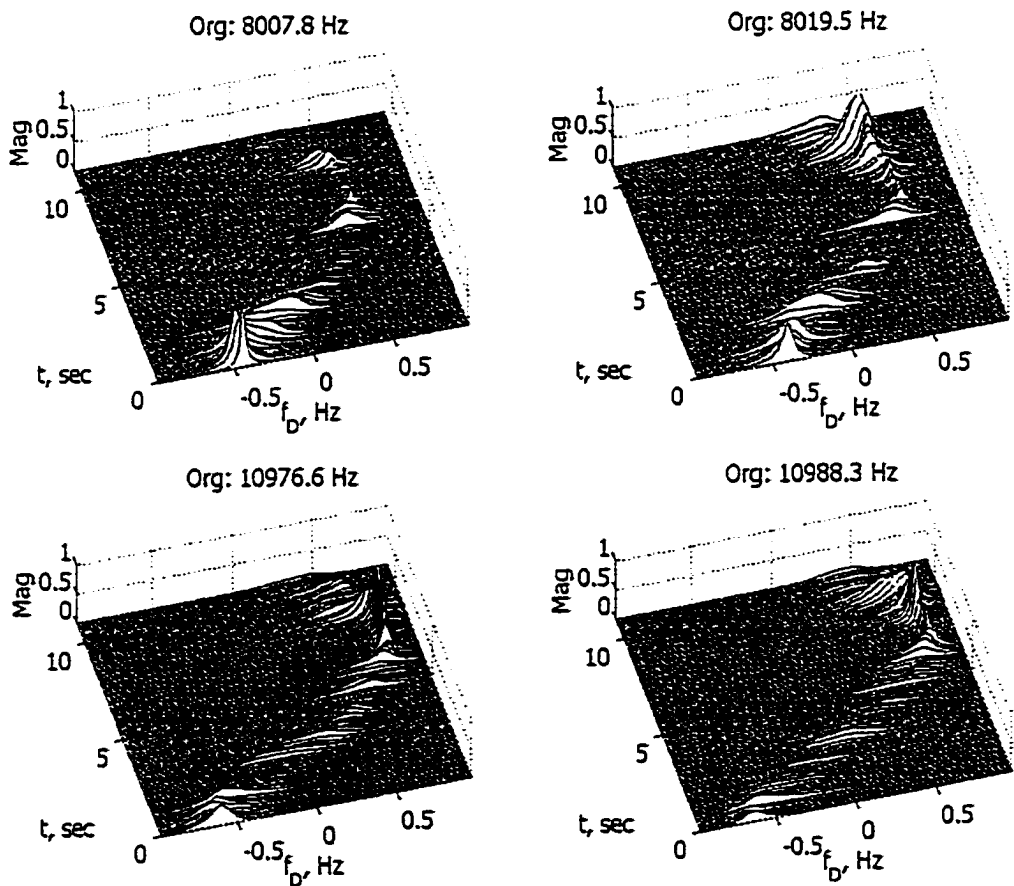


**Figure 4.9** Simulated frequency fluctuation of 4 sinusoidal components

The designing constants  $a_k$  and  $\tilde{a}_k$  are chosen to be

$$\tilde{a}_k = 0.0375 N_r \sigma_k, \quad a_k = \sqrt{\sigma_k^2 - \tilde{a}_k^2} \quad (4.18)$$

where  $N_r$  is the number of surface reflection. Note that  $a_k$  determines the common portion of the random delay fluctuation in the  $k^{\text{th}}$  eigenray. A proper selection of  $a_k$  and  $\tilde{a}_k$  is crucial in determining the fading patterns and depths in the broadband channel transfer function. This point will be discussed later in Figure 4.13. Figure 4.9 shows the time varying Doppler spectra for the four reference tones. These results are derived by the MVSE approach in Appendix B. As was intended, the characteristics of the data in Figure 4.9 and Figure 4.5 are very similar to each other.

#### 4.4.2. Instantaneous Doppler Frequency

The trajectories of the peak spectra (in Figure 4.9) show the instantaneous Doppler frequencies in the time-frequency plane. To verify this statement, choose

$$\tilde{a}_k = 0, \quad a_k = \sigma_k \quad (4.19)$$

such that the delay fluctuation of all eigenrays are perfectly correlated. Figure 4.10 shows the contours for Doppler spectra of the reference tone  $f = 8007.8$  Hz. In addition, the instantaneous Doppler frequency  $f_D = f_0(v_0 \cos \phi_k + \xi_k(t))/c$  in (4.8) is also plotted. Here,  $v_0 = 0$  and  $\xi_k = \xi_0$  for every  $k$ . Figure 4.10 shows that the instantaneous Doppler frequencies calculated from (4.8) coincide with the trace of the peak Doppler spectra.

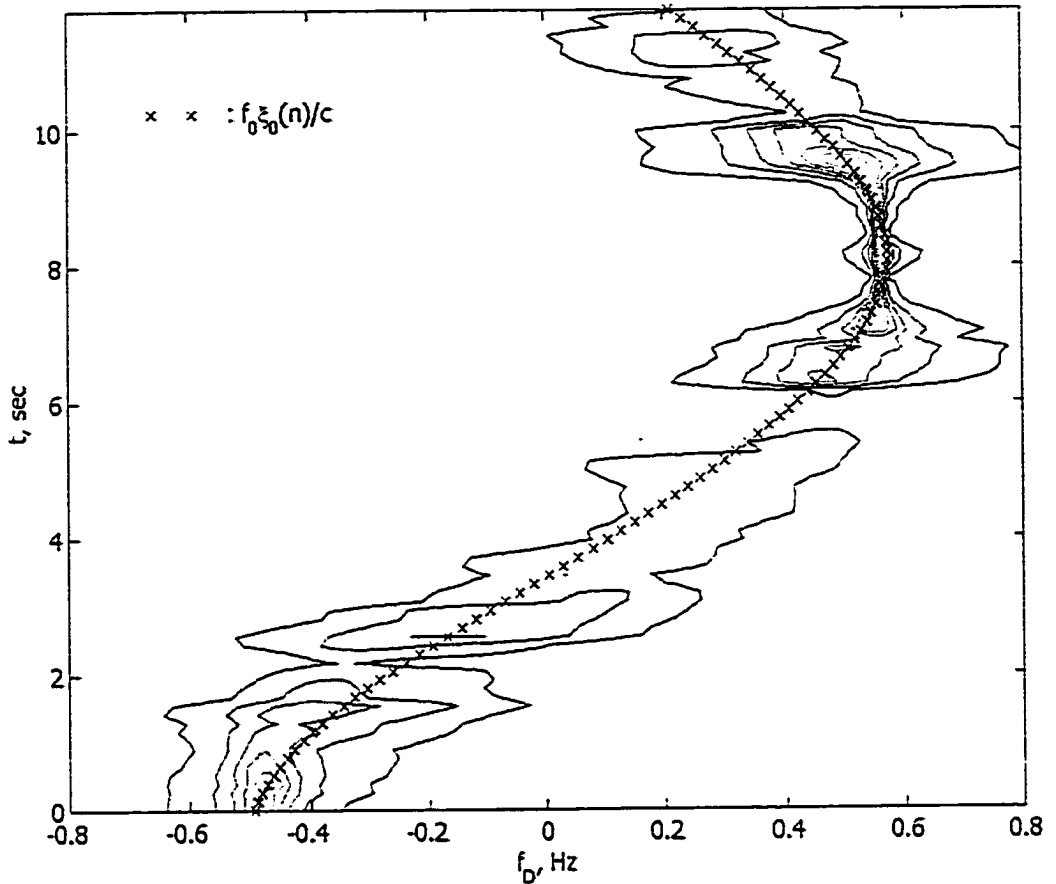


**Figure 4.10** Comparison between the random process  $f_0 \xi_0(n)/c$  and the estimate of instantaneous Doppler shift  $f_D$

### 4.4.3. Power Spectral Density

Power spectral density (PSD) can be estimated using Welch's averaged-periodogram method [18]. After frequency translation (complex bandshifting) and decimation, PSD's of two reference tones estimated from experimental and simulated signals are shown in Figure 4.11. In this simulation, all parameters are the same as in Figure 4.9. Figure 4.11a-b shows PSD's for experimental signals [7,16] and Figure 4.11c-f for simulated signals. The original tonal frequency in the left figures is 8007.8 Hz and that of the right figures is 10988.3 Hz.

Each PSD was obtained from a 14.952-second period of a corresponding experimental or simulated signal.

Let us examine the experimental PSD's first. Because the velocity between source and receiver is zero ( $v_0 = 0$ ), there does not exist mean Doppler shift in Figure 4.11a and Figure 4.11b. However, the power spectrums of tonal signals are broadened due to Doppler spread. Moreover, the Doppler spread for the higher frequency tonal is broader than that of the lower frequency tonal. Such broadband characteristics are well shown in our simulated results. In Figure 4.11c and Figure 4.11d, because  $v_0$  is 0, there is no Doppler shift. Yet, the frequency spread due to delay fluctuations shown in Figure 4.11c is narrower than that in Figure 4.11d.

Our channel simulator can also be applied to moving-source scenarios. For example, consider  $v_0 = 10$  knots. The Doppler frequency shift in Figure 4.11e is 28.2 Hz ( $10 \text{ knots} \times 0.514 \text{ m/knots} \div 1460 \text{ m/sec} \times 8007.8 \text{ Hz}$ ), and that in Figure 4.11f is 38.7 Hz ( $10 \text{ knots} \times 0.514 \text{ m/knots} \div 1460 \text{ m/sec} \times 10988.3 \text{ Hz}$ ). In addition, the frequency spread due to delay fluctuations shown in Figure 4.11e is narrower than that in Figure 4.11f. It is also remarkable that the Doppler spread is not symmetrical. The signals with smaller Doppler shifts (in the left hand side of spectrum) are weaker than those with larger Doppler shifts (in the right hand side). This is due to the fact that rays going through more reflections between the sea surface and the channel bottom are weaker and also have greater elevation angles (greater angles imply smaller Doppler shifts).



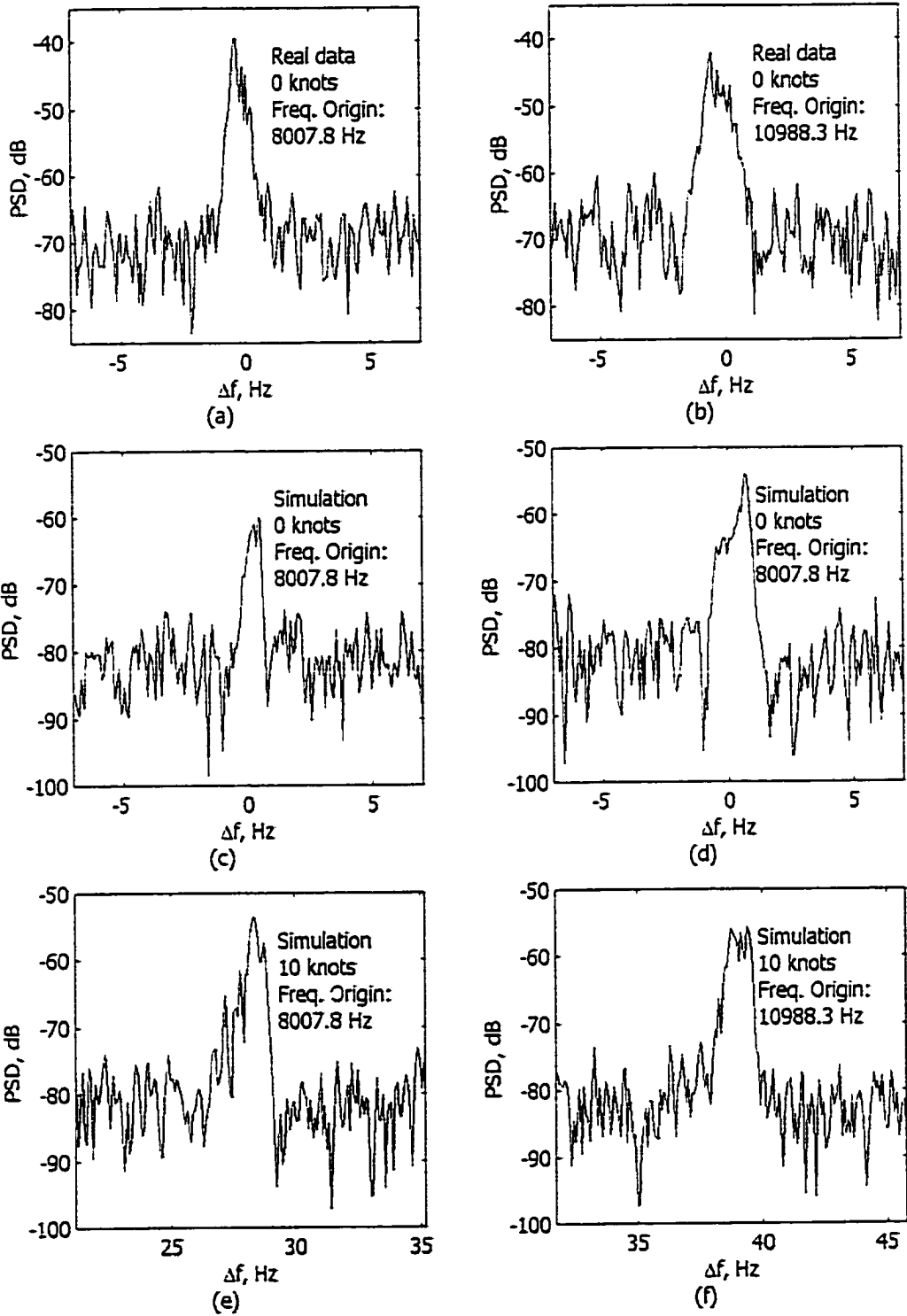


**Figure 4.11** Power spectral densities of experimental and simulated narrowband signals

#### 4.4.4. Mean Doppler Shift and Spread

Figure 4.12a shows the Doppler shifts computed using both (4.9) and (4.10). To use (4.9), 20 independent simulations per horizontal velocity  $v_0$  are performed to obtain the averaged PSD of the simulated Doppler spread signal first. Equation (4.9) is then employed to calculate  $f_{DM}$ . In these simulations, the standard deviation of  $\xi_i(n)$  is set to  $0.125 \times 10^{-5} \times c$  to make the RMS bandwidth of Doppler spread approximately 0.14 Hz. As shown in Figure 4.12a, the results obtained from (4.9) are very close to those from (4.10).

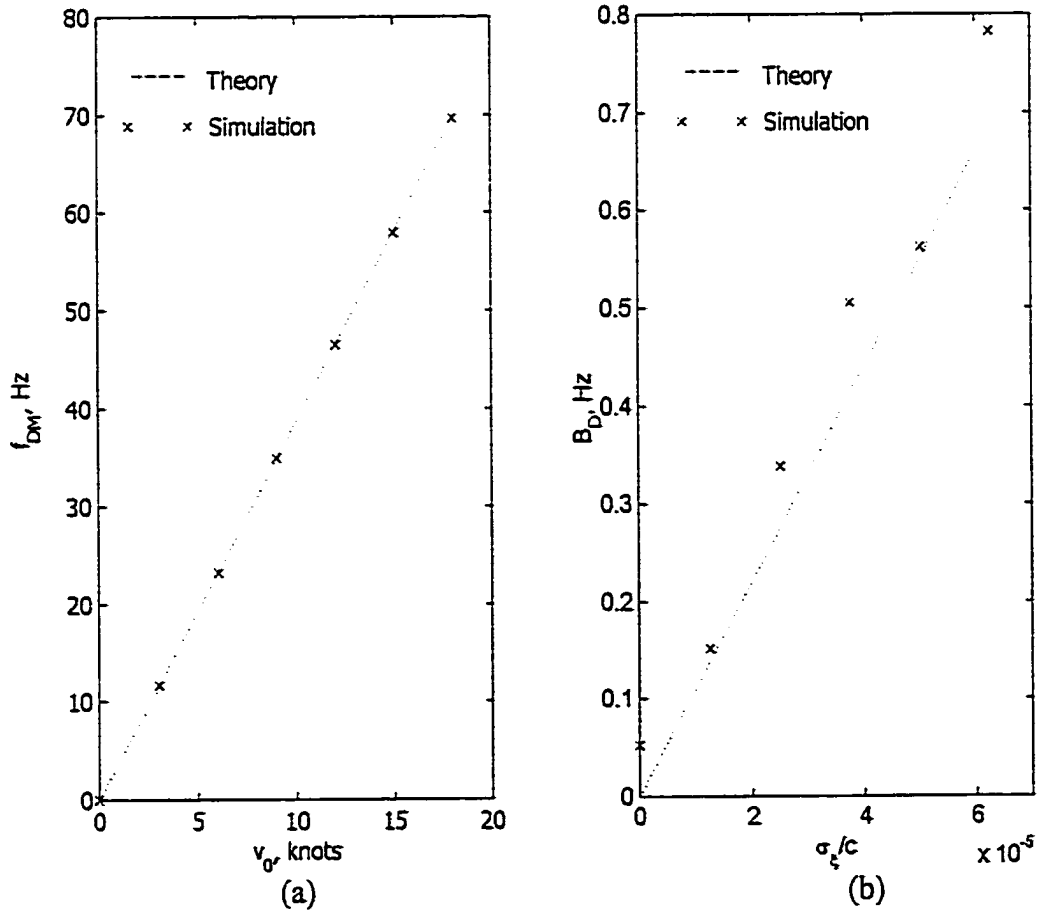


**Figure 4.12** Comparison between theoretical values (Equation 4.10) and simulation results (Equation 4.9) for mean Doppler Frequency  $f_{DM}$  and rms Doppler spread  $B_D$

Figure 4.12b shows the Doppler spread computed using both (4.9) and (4.11). Similarly, to use (4.9), 50 independent simulations are performed for each  $\sigma_f$  in the figure, and their PSD's are averaged before applying (4.10 & 4.11). The results are shown in Figure 4.12b, where the rms Doppler spreads  $B_D$ 's are positively biased comparing to theoretical values. The cause of this bias is mainly due to limited resolution of PSD estimation, which is obvious at  $\sigma_f = 0$ . Taking into account this bias, we can see that  $B_D$ 's obtained from simulations are in reasonable agreement with theoretical values.

#### 4.4.5. Frequency and Time Response of the Simulated Channel

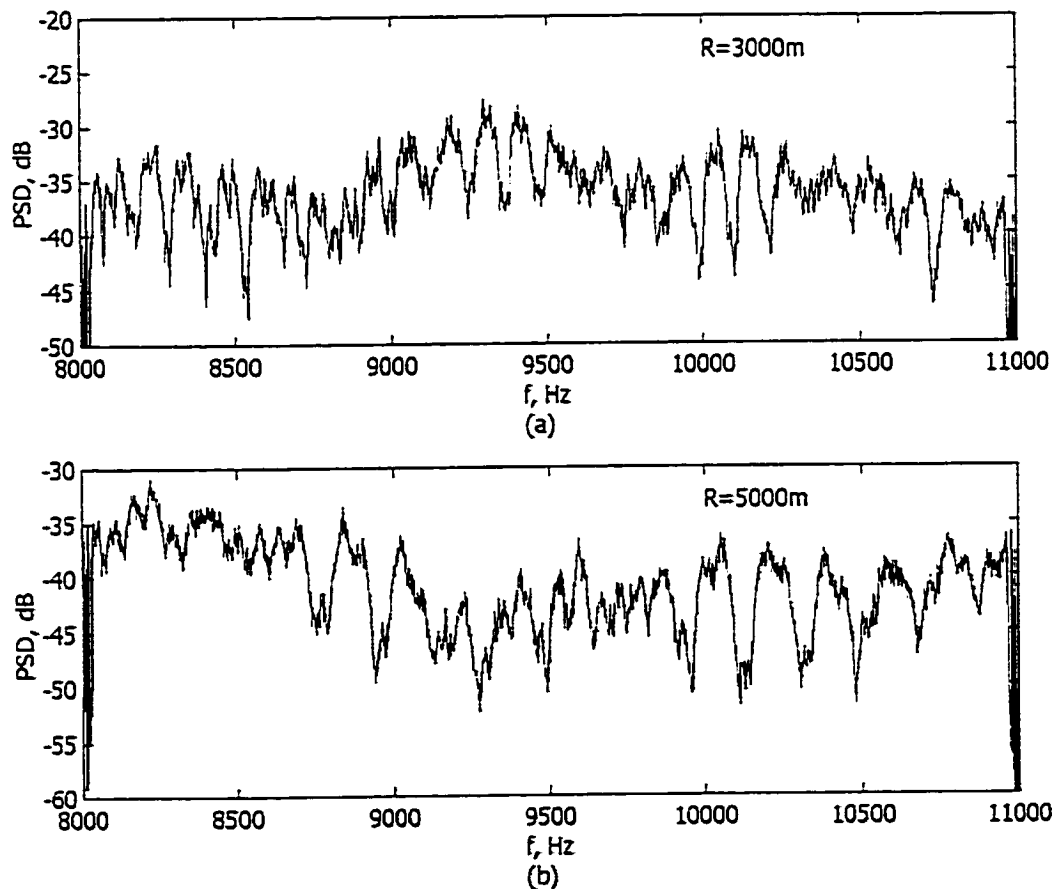


**Figure 4.13** Power spectral densities of experimental and simulated broadband signals

The frequency spectrums of simulated signals are shown in Figure 4.13. Since the OFDM source signal has almost flat frequency spectrum, the spectrum of received signal directly reflects frequency response of the channel. Figure 4.13a is power spectral density of simulated signal for distance of 3000 m, and Figure 4.13b is that for 5000 m. All other parameters are the same as those in Figure 4.9. The signal to noise ratio is 20 dB. Comparing the two simulated channel responses, coherent bandwidth is wider for the longer distance scenario because of smaller differences in ray travel times.

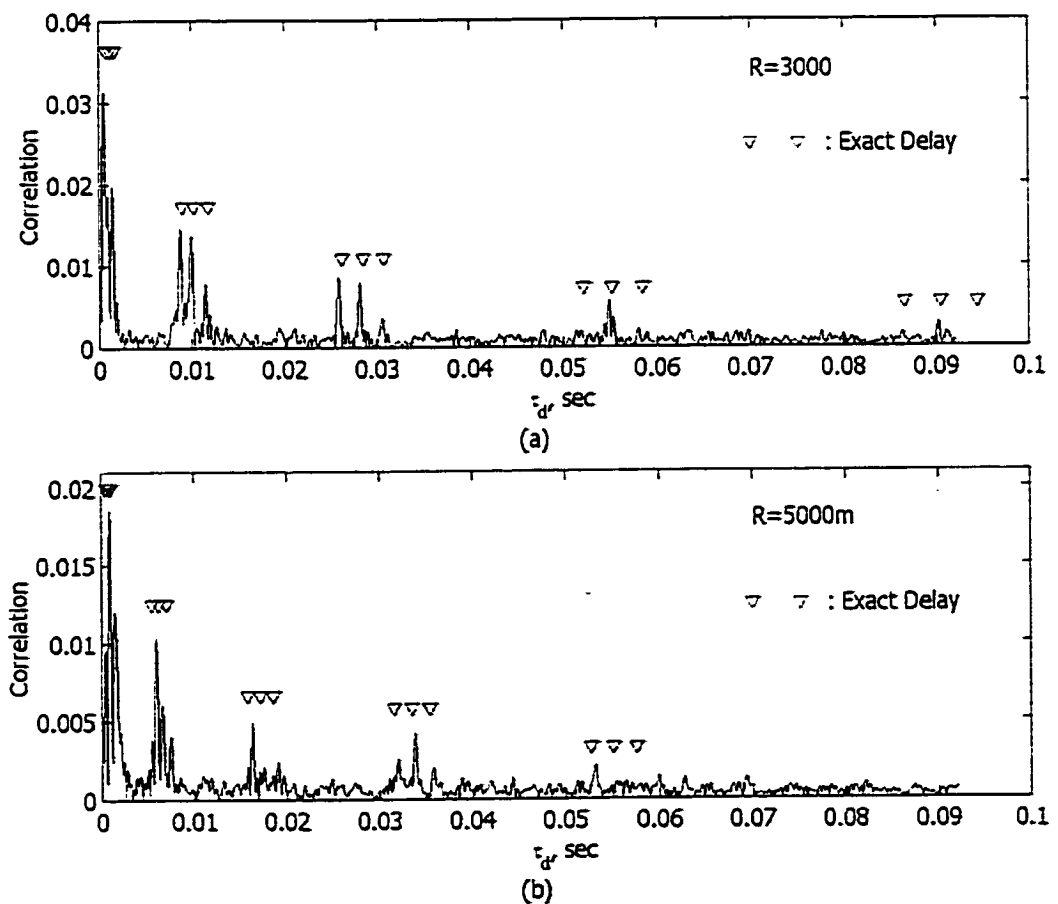


**Figure 4.14** Path delay estimation for simulated signal

Figure 4.14 shows the estimates of impulse responses (cross-correlations between simulated channel outputs and the source waveform) of the channel. The triangle marks above the curves show the exact delays. Only 15 marks are shown for 20 rays because there are only 15 distinct arrival times. The peaks of the cross-correlation results are well matched to the exact delays. The ray magnitudes decrease as their corresponding delays increase because rays with longer delay experience more reflections and have longer path-length.

As mentioned earlier,  $\tilde{a}_k$  and  $a_k$  in (4.17) determine correlation between time-delay fluctuations for different rays. If  $\tilde{a}_k$  is large comparing to  $a_k$ , the correlations among rays are reduced and consequently, the frequency selectivity of the channel becomes lessen. In Figure 15a, b and c, power spectrums of simulated signals in the case of  $\tilde{a}_k=0$  (i.e.,  $a_k=\sigma_k$ , all rays have the same time-delay fluctuation),  $\tilde{a}_k=0.0375 N_r\sigma_k$ , and  $\tilde{a}_k=\sigma_k$  (i.e.,  $a_k=0$ , all rays have independent time-delay fluctuations) are shown to demonstrate such effect. Therefore, one has to tune these two parameters  $\tilde{a}_k$  and  $a_k$  to yield the proper frequency selectivity in practice.

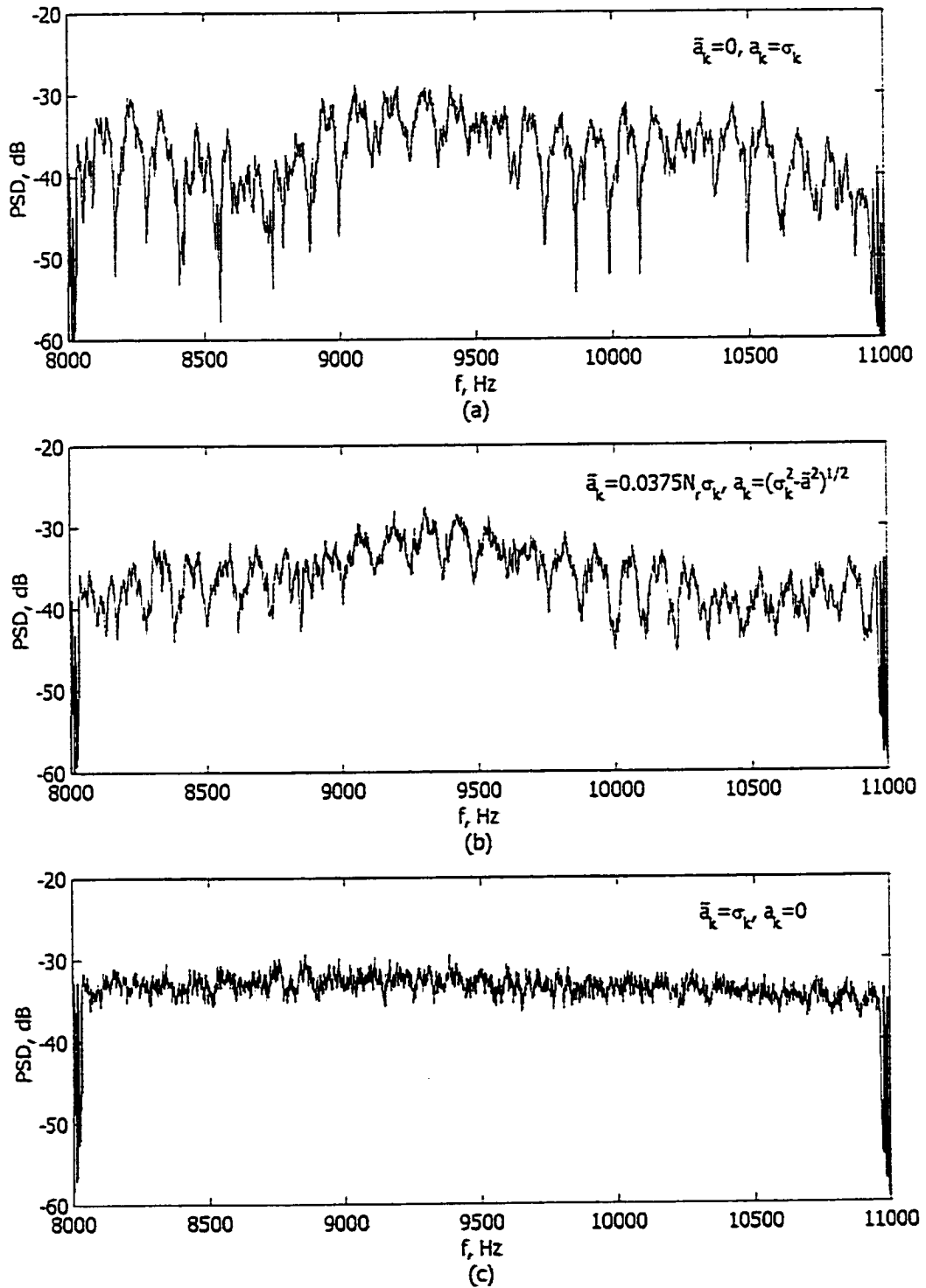


**Figure 4.15** PSD for 3 different sets of  $\bar{a}_k$  and  $a_k$

## 4.5. Conclusions

A physics-based broadband channel simulator was established to simulate an underwater acoustic channel as a time-varying filter with added colored noises. Although the frequency dependence of loss factors are applied in the design of simulator, this study concentrates on the generation of Doppler effects using a novel frequency-modulator scheme. The random fluctuations in propagation delays are analyzed and simulated to generate realistic Doppler spreads found in practical time-varying UWA channels. The relationships between input parameters and resultant Doppler effects are established to enable one to have precise control of the time-varying effects of simulation results. Our scheme provides means to determine both instantaneous and ensemble averaged Doppler shifts and spreads for narrowband signals and to control the frequency selectivity for broadband signals.

The features of proposed simulator are demonstrated through sample simulations and are verified by experimental data. Although we consider isospeed channel in our simulation, the scheme can be directly applied to general inhomogeneous profiles if a general ray-tracing code is available. In order to focus on the study on Doppler effects, we have ignored some practical effects such as rough surface scatterings, reverberations, amplitude variations, and phase changes. These effects can be added into the proposed channel simulator and will be considered in our future works. Since the proposed simulator is very general, it will be useful for performance prediction and algorithm development of both UWA broadband communications and other sonar systems.

## Appendix A

### Mean Doppler Frequency and RMS Doppler Spread

The autocorrelation  $R_{xx}(t, t - \tau)$  of  $x_c(t)$  is

$$R_{xx}(t, t - \tau) = E \{ x_c(t) x_c^*(t - \tau) \} = e^{j2\pi f_0 \left( t - \frac{v_0 \cos \phi_k}{c} \tau \right)} E \{ \exp jz(t, \tau) \} \quad (\text{A.1})$$

where the random variable  $z(t, \tau)$  is represented by

$$z(t, \tau) = \frac{2\pi f_0}{c} \int_{t-\tau}^t \xi(\zeta) d\zeta. \quad (\text{A.2})$$

Assuming  $\xi(t)$  is a stationary, zero mean Gaussian random process with variance of  $\sigma_\xi^2$ ,  $z(t, \tau)$  is also a zero mean Gaussian random variable since it can be considered as a weighted sum of Gaussian random variables. Moreover, the variance  $\sigma_z^2(\tau)$  of  $z(t, \tau)$  does not depend on  $t$ , but on  $\tau$  only, and is defined as:

$$\sigma_z^2(\tau) = E \{ z(0, \tau) z^*(0, \tau) \} = \left( \frac{2\pi f_0}{c} \right)^2 \int_0^\tau \int_0^\tau E \{ \xi(\nu) \xi^*(\zeta) \} d\nu d\zeta \quad (\text{A.3})$$

The expectation in (A.1) is the characteristic function of Gaussian random variable  $z(t, \tau)$ .

Therefore  $R_{xx}(t, t - \tau)$  can be represented in terms of  $\sigma_z^2(\tau)$ , that is

$$R_{xx}(\tau) = \exp(j2\pi f_0 \tau) R_D(\tau), \quad R_D(\tau) \equiv \exp \left( j2\pi f_0 \frac{v_0 \cos \phi_k}{c} \tau \right) \exp \left( -\frac{\sigma_z^2(\tau)}{2} \right) \quad (\text{A.4})$$

The Doppler spectrum  $X_D(f)$  is the Fourier transform of the demodulated autocorrelation

$R_D(\tau)$ :

$$X_D(f) \equiv \int_{-\infty}^{\infty} R_D(\tau) e^{-j2\pi f \tau} d\tau \quad (\text{A.5})$$

The mean Doppler frequency  $f_{DM}$  is



$$f_{DM} = \int_{-\infty}^{\infty} f X_D(f) df = \frac{1}{j2\pi} \left( \frac{d}{d\tau} R_D(\tau) \right) \Big|_{\tau=0} = f_0 \frac{v_0 \cos \phi}{c} \quad (\text{A.6})$$

The mean square Doppler bandwidth  $B_D^2$  is

$$B_D^2 = \frac{1}{P} \int_{-\infty}^{\infty} f^2 X_D(f) df - f_{DM}^2 = \frac{1}{4\pi^2 P} \left( \frac{d^2}{d\tau^2} R_D(\tau) \right) \Big|_{\tau=0} = \left( \frac{f_0}{c} \right)^2 \sigma_{\xi}^2 \quad (\text{A.7})$$

Therefore,

$$B_D = \left( \frac{f_0}{c} \right) \sigma_{\xi}. \quad (\text{A.8})$$

## Appendix B

### Instantaneous Frequency Spectrum Estimation using MVSE

The procedure to obtain instantaneous frequency spectrum in Figure 4.5, Figure 4.9 and Figure 4.10 can be divided into the following three steps.

Step1. Complex bandshift, lowpass filtering and decimation:

$$x_B(m) = g_L(m) * [x(m)e^{-j2\pi f_0 m}] \text{ (complex bandshifting and lowpass filtering)}$$

$$x_D(n) = x_B(mD) \text{ (decimation by factor of } D\text{)}$$

where

$x(m)$  : input sequence

$f_0$  : center frequency, which is normalized by sampling frequency  $f_s$ ,

$g_L(m)$  : impulse response of lowpass filter with cut - off frequency  $f_c < \frac{f_s}{2D}$ .

$f_s$  : original sampling frequency before decimation

Step2. Estimate instantaneous correlation matrices:

$$\hat{\mathbf{R}}_{xx}(n) = \frac{1}{2K+1} \sum_{k=n-K}^{n+K} \mathbf{x}(k)\mathbf{x}^H(k)$$

where,

$\hat{\mathbf{R}}_{xx}(n)$  : estimate of correlation matrix.

$\mathbf{x}(k)$  :  $(2L+1) \times 1$  data vector (input time sequence).

$$\mathbf{x}(k) = [x_D(k+L) \dots x_D(k) \dots x_D(k-L)]^T$$

$(\ )^H$  : conjugate transpose of a matrix

Step3. Compute minimum variance spectral estimate:

$$\hat{S}_{xx}^{MV}(f, n) = \left[ \mathbf{e}^H(f) \hat{\mathbf{R}}_{xx}^{-1}(n) \mathbf{e}(f) \right]^{-1}$$

where

$S_{xx}^{MV}(f, n)$  is the MVSE of sample  $x(n)$  for frequency  $f$  which is normalized by the sampling frequency  $f_s / D$ .

$$\mathbf{e}(f) = \left[ 1, e^{j2\pi f}, e^{j4\pi f}, \dots, e^{j4L\pi f} \right]$$

## References

- [1] Abolfazl Falahati, Bryan Woodward, and Stephen C. Bateman, "Underwater acoustic channel models for 4800b/s QPSK signals," *IEEE J. Ocean. Eng.*, vol. 16, no. 1, pp. 12-20, January 1991.
- [2] R. Galvin and R.F.W. Coates, "A stochastic underwater acoustic channel model," *Proc. of IEEE Oceans '96*, vol. 1, pp. 203-210, September, 1996.
- [3] Essebbbar, G. Loubet, and F Vial, "Underwater acoustic channel simulations for communications," *Proc. of IEEE Oceans '94*, vol. 3, pp. 496-500, September, 1996.
- [4] Christian Bjerrum-Niese, Leif Bjorno, Marc Andre Pinto, and Bruno Quelled, "A simulation tool for high data-rate acoustic communication in a shallow-water, time-varying channel," *IEEE J. Ocean Eng.*, vol. 21, no. 2, pp. 143-149, April 1996.
- [5] Albert A. Gerlach, "Acoustic transfer function of the ocean for motional source," *IEEE Trans. Acoust., Speech, Signal Processing*, vol. ASSP-26, no. 6, pp. 493-501, December 1978.
- [6] Byung-Chul Kim and I-Tai Lu, "Parameter Studies of OFDM Underwater Communication Systems," in *Proc. Oceans 2000*, vol.2 pp. 1251-1255, Sept. 2000.
- [7] Byung-Chul Kim and I-Tai Lu, "Sea trial results of a robust and spectral-efficient OFDM underwater communication system," under preparation for publication.
- [8] Robert J. Urick, *Sound Propagation in the Sea*, Los Altos: Peninsula Publishing, 1982, p.5-10.
- [9] Robert J. Urick. *Principles of Underwater Sound*, 3<sup>rd</sup> ed., New York: McGraw-Hill, 1983.

- [10] R. Coates, "An empirical formula for computing the Beckmann-Spizzichino surface reflection loss coefficient," *IEEE Trans. Ultrasonics, Ferroelectrics, and Frequency Control*, vol. 35, no. 4, pp. 522-523, July 1988.
- [11] Adam Zielinski, Young-Hoon Yoon, and Lixue Wu, "Performance analysis of digital communication in a shallow water channel," *IEEE J. Ocean. Eng.*, vol. 21, no. 2, pp. 143-149, April 1996.
- [12] H. Weinberg, *The Generic Sonar Model*, Naval Underwater systems Center tech. document 9671A New London, CT: 1980.
- [13] Harry L. Van Trees, *Detection, Modulation and Estimation Theory, Part III Radar-Sonar signal Processing and Gaussian Signals in Noise*, New York: John Wiley & Sons, Inc., pp.363, 1971.
- [14] Harry L. Van Trees, *Detection, Modulation and Estimation Theory, Part II Nonlinear Modulation Theory*, New York: John Wiley & Sons, Inc., pp.100-104, 1971.
- [15] Ronald E. Crochiere and Lawrence R. Rabiner, *Multirate Digital Signal Processing*, NJ: Prentice-Hall, Inc., pp. 79-81, 1983.
- [16] Michael B. Porter, Vincent K. McDonald, Paul A. Baxley, and Joseph A. Rice, "SignalEx: linking environmental acoustics with the signaling schemes," *Proc. Oceans 2000*, vol.1 pp. 595-600, Sept. 2000.
- [17] Don H. Johnson and Dan E. Dudgeon, *Array Signal Processing: Concepts and Techniques*, NJ: Prentice-Hall, Inc., pp. 76, 330-333, 1993.
- [18] David J. Defatta, Joseph G. Lucas and William S. Hodgkiss, *Digital Signal Processing: A System Design Approach*, NY: John Wiley & Sons, 1988.

## Chapter 5

# OFDM Underwater Communications Systems

### 5.1. Introduction

Due to the complexity of environment and the motions of transducers, sea surface, etc., the underwater acoustic signals exhibit random temporal and spatial frequency fluctuations in both amplitude and phase. In addition, because of the multipath propagation characteristics of the underwater channels, the acoustic signals suffer severe time and frequency selective fades. These highly space, time and frequency dependent features pose numerous obstacles for any attempt to establish reliable, high-speed, and long-range underwater acoustic communications.

In recent years, many efforts have been made to develop coherent broadband systems with an emphasis on equalization for increasing the communication data rates and distances. However, there are environments in which the equalization-based phase coherent broadband communication algorithms fail or yield excessive bit errors. The fundamental technical bottleneck of this kind of approaches is the challenge in equalizing time-varying frequency-selective fades.

An alternative approach to achieve reliable, high-speed communications is to use a multi-

carrier modulation scheme, in which broadband data is effectively transmitted in parallel as  $M$  narrowband channels on  $M$  subcarriers [1-2]. To improve spectral efficiency and eliminate the use of guard bands between sub-carriers, each subcarrier is chosen to be orthogonal to the others. Such a multi-carrier system is referred to as orthogonal frequency division multiplexing (OFDM). If its bandwidth is smaller than the coherent bandwidth, each narrowband subcarrier experiences only flat fading during propagation through the underwater channels. To further combat the frequency dispersiveness, the symbol duration of the data stream carried by each subcarrier is chosen to be much larger than the delay spread of the channel so that intersymbol interference can be removed by simple techniques such as guard time insertion. Similarly, pilots can also be inserted into the data streams to estimate the time variation of each narrowband subcarrier channel. The difficulty in equalization is greatly reduced.

The OFDM technique has been claimed to be one of the most promising future communication technologies for achieving high data rate and large system capacity. It is currently a very popular choice for future wireless applications, including wireless LANs, cellular and PCS data, and possibly Fourth Generation wireless communications systems. However, little efforts are devoted toward underwater acoustic communications. This paper presents design criteria, analysis procedures and simulation results of an OFDM system for broadband underwater acoustic communications. Practical issues such as broadband channel simulation, Doppler shift offset, and pilot channel estimation are addressed.

## 5.2. Underwater Acoustic Communications (UWA)

### 5.2.1. Channel Modeling

Underwater acoustic channel supports time-varying multiple propagation paths. Each path has its unique but time-dependent delay  $\tau_p(t)$  and complex attenuation  $\alpha_p(t)$ . The channel impulse response is represented by

$$g(\tau; t) = \sum_p \alpha_p(t) \delta[\tau - \tau_p(t)] \quad (5.1)$$

Both  $\tau_p(t)$  and  $\alpha_p(t)$  can be expressed as random processes due to the facts that the geometry of both sea floor and sea surface are complex and random, and the motions of the sea surface, currents and transducers are unpredictable. For a transmitted signal  $x(t)$ , the received signal  $y(t)$  through the channel can be represented by

$$y(t) = x(t) * g(\tau; t) + n(t) = \sum_p \alpha_p(t) x[t - \tau_p(t)] + n(t) \quad (5.2)$$

where  $n(t)$  is background noise. Because of the time and frequency dispersion, the channel has time-varying frequency selectivity. The coherence bandwidth is approximately reciprocal of the maximum propagation delay  $\tau_{\max}(t)$ .

### 5.2.2. Doppler Effect

The random motions of sea surfaces and currents cause Doppler spread. In addition, the motions of transducers contribute to a Doppler shift to each ray arrival. Since ray angles are different, the Doppler shifts caused by these rays are also different. The differences among these Doppler shifts also contribute to Doppler spread of the received signal. Usually, the



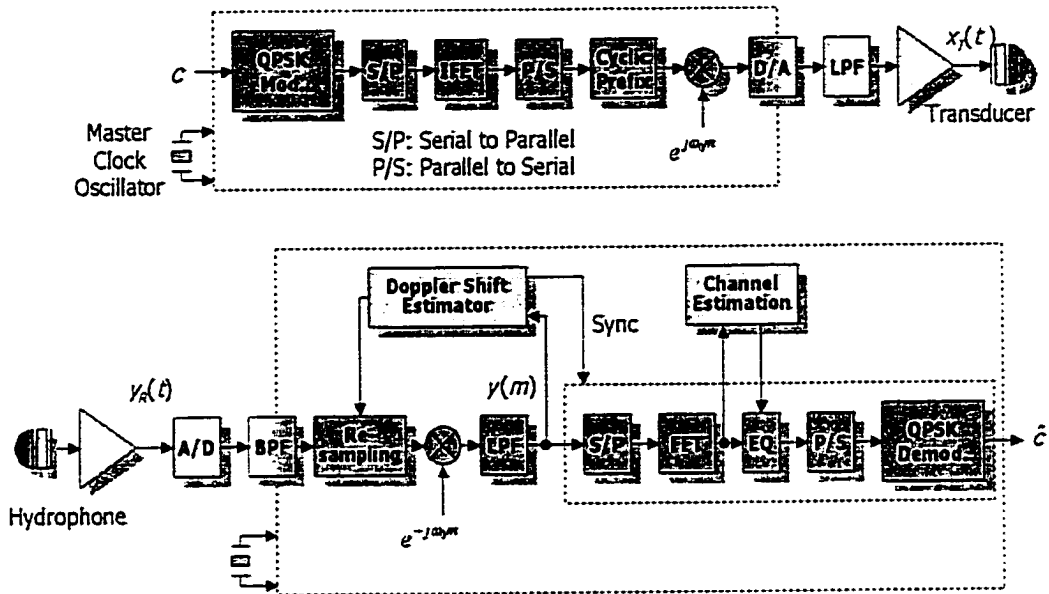


**Figure 5.1** Block diagram of a OFDM system for underwater communications

average Doppler shift can be much larger than the overall Doppler spread and has to be compensated properly in the receiver.

Let  $\Delta_p$  be the Doppler shift factor of the  $p^{\text{th}}$  ray and  $\Delta$  be the average value of  $\Delta_p$ . If  $v$  is the relative speed for two platforms,  $\theta_p$  is the reception angle,  $C$  is the sound-speed,  $\Delta_p = (v/C) \cos \theta_p$ . Here, without loss of generality, the transmission angle is also assumed to be  $\theta_p$ . Assuming the Doppler shift is constant in a symbol-duration  $T$ , from (5.2),

$$\begin{aligned}
 y(t) &= \sum_p \alpha_p(t) x[t + \Delta_p t - \tau_p^r(t)] + n(t) \\
 \text{or} &= \sum_p \alpha_p(t) x[(1 + \Delta)t - \tau_p^r(t)] + n(t)
 \end{aligned} \tag{5.3}$$

In (5.3),  $(1 + \Delta)$  is a time-scaling factor causing Doppler shift and  $\tau_p^r(t)$  and  $\alpha_p(t)$  contributes to Doppler spread.

### 5.3. OFDM Systems for Underwater Communications

The block diagram of the OFDM modem for underwater communications is shown in Figure 5.1. In underwater, OFDM signal is usually ultra broadband because of the low carrier frequency (or large bandwidth to carrier frequency ratio). In fact, the carrier frequency is so low that down conversion can be done in digital processing unit.

#### 5.3.1. Transmitting and Receiving Signal

In Figure 5.1a, input  $c$  is a serial bit-stream that is to be QPSK modulated. The S/P outputs  $\{d_k\}$  are modulated by  $N$  subcarriers, and each of them has frequency spacing of  $1/T$  Hz. They are summed to form a symbol with duration  $T$ . The modulation and summing operation can be efficiently implemented using inverse FFT. It is followed by cyclic prefix insertion, D/A conversion, and low pass filtering. The baseband signal  $x(t)$  and the transmitted signal  $x_T(t)$  can be represented by

$$x(t) = \sum_{k=0}^{N-1} d_k e^{j\frac{2\pi}{T}kt}, \quad x_T(t) = \sum_{k=0}^{N-1} d_k e^{j2\pi(\frac{k}{T}+f_0)t} \quad (5.4)$$

where  $f_0$  is carrier frequency and  $d_k$  is the  $k^{\text{th}}$  QPSK signal. From (5.3) & (5.4), received signal  $y_R(t)$  can be represented by

$$y_R(t) = \sum_p \alpha_p(t) \sum_{k=0}^{N-1} d_k e^{j2\pi(\frac{k}{T}+f_0)[(1+\Delta)t - \tau_p^*(t)]} + n(t). \quad (5.5)$$

#### 5.3.2. Doppler Shift Estimation and Compensation

In (5.5), for  $p$ th ray, time variable  $t$  was scaled and delayed by  $[(1+\Delta)t - \tau_p^*(t)]$ . The first

(scaling) term contributes to Doppler shift and signal bandwidth variation, and the second (delayed) term contributes to Doppler spread. In addition, the time varying attenuation  $\alpha_p(t)$  in (5.5) also contributes to Doppler spread. If Doppler effect is considerable, the effect of the first term (time scaling) is far greater than that of the second term. In a recent work [3], sampling rate conversion (using the sampling rate  $(1 + \Delta) / T_s$  at receiver) is employed to compensate effectively Doppler shift and signal bandwidth variation due to the time scaling term in (5.5).

### 5.3.2.1. Doppler Shift Estimation using Cyclic Prefix

In order to estimate the time scaling factor  $1 + \Delta$ , we extend the ML-estimation of carrier frequency offset in [4] using correlation between the cyclic prefix and its replica (the tail part of the symbol). Because an underwater OFDM system usually requires a long cyclic prefix to avoid the large inter-symbol interference, this approach is well suited here.

Assume that the variation of attenuation  $\alpha_p(t)$  and delay  $\tau_p''(t)$  in a symbol-duration  $T$  is negligible. Sampled at every interval  $T_s$  and down-converted to baseband, the signal  $y(mT_s)$  in receiver can be represented by

$$y(mT_s) = \sum_p \alpha_p \sum_{k=0}^{N-1} d_k e^{j2\pi \left\{ \left( \frac{k}{T} + f_0 \right) \left[ (1 + \Delta) m T_s - \tau_p'' \right] + f_0 m T_s \right\}} + n(mT_s) \quad (5.6)$$

where  $T_s = T / N$  is the known sampling interval in the transmitter and  $T_s$  is the sampling interval in the receiver. Note that path-attenuation  $\alpha_p$ 's are mutually uncorrelated and the magnitude of QPSK signal  $d_k$  is 1. Since the cyclic prefix and their replicas are well correlated while the remaining samples are mutually uncorrelated, the auto correlation

$$R_y(\xi) \equiv E \left\{ \psi(mT_s) y^*((m + \xi)T_s) \right\} = \sum_p E \{ |\alpha_p|^2 \} \sum_{k=0}^{N-1} e^{-j2\pi \frac{k}{T} (1+\Delta)\xi T_s} \times e^{-j2\pi((1+\Delta)T_s - T_{s0})\xi f_0} + E \left\{ n(mT_s) n^*((m + \xi)T_s) \right\} \quad (5.7)$$

If the noise  $n$  is white, the magnitude of  $R_y$  is maximum at the zero lag  $\xi = 0$  and at the non-zero lag

$$\xi = \xi_{peak} \approx NT_{s0} / [(1 + \Delta)T_s]. \quad (5.8)$$

Thus, time scaling factor can be obtained from measuring the time lag  $\xi_{peak}$  between the first and the second peaks of  $R_y$ . It can also be obtained from the phase  $\phi_{peak}$  of  $R_y$  at the second maximum at ( $\xi = \xi_{peak}$ ).

$$\phi_{peak} \approx -2\pi [(1 + \Delta)T_s - T_{s0}] \xi_{peak} f_0 \quad (5.9)$$

Due to noises and numerical errors, the estimates of time scaling factors from (5.8) and (5.9) may not be the same. However, if the estimates of time scaling factor  $(1+\Delta)$  from (5.8) and (5.9) are accurate and therefore equal, and if the sampling interval  $T_s = T_{s0} / (1 + \Delta)$ , the peak location  $\xi_{peak}$  in (5.8) becomes integer  $N$  and the phase  $\phi_{peak}$  in (5.9) becomes 0. Based on this observation, we propose the following iterative approach for estimating the time scaling factor  $(1+\Delta)$ :

Step 1: Guess an initial sampling interval  $T_s$ .

Step 2: Find  $\xi_{peak}$  and  $\phi_{peak}$  from  $R_y(\xi)$ .

Step 3: Derive an  $(1+\Delta)$ -estimate from (5.8) and (5.9).

Step 4: If  $\xi_{peak} \approx N$  and  $\phi_{peak} \approx 0$ , terminate the iteration.

Step 5: Determine a new sampling interval  $T_s = T_{i0} / (1 + \Delta)$  .

Step 6: Repeat Steps 1 to 5.

### 5.3.2.2. Doppler shift compensation

Sampling rate conversion is implemented by polyphase filter bank, which is equivalent to interpolator-decimator pair [5]. If the total number of phases is 4096, 0.025% of interpolating resolution can be obtained. After Doppler shift compensation, time scaling factor  $(1 + \Delta)$  in (5.6) is removed.

### 5.3.2.3. Pilot-aided MMSE Channel Estimation and Equalization

Even though Doppler shift is compensated, the remaining Doppler-spread (compounding with the existing multipath propagation feature) still causes time-varying frequency-selective fading. Usually, an adaptive channel estimation and equalization procedure is required in the receiver. A practical 2-dimensional MMSE channel estimator [6] needs to be designed with proper frequency and time correlation functions. The slowly varying delay profiles can be estimated using pilots or other probing methods. However, statistics for Doppler spread in a specific situation are difficult to obtain. Fortunately, we find from our simulations that the probability density function of Doppler spread can be considered uniform with a limited maximum frequency-spread in most cases.

In order to interpolating the channel responses in the time-frequency plane, a 2-D pilot grid has to be arranged properly to satisfy Nyquist sampling theorem. Pilot spacing in frequency domain  $N_f$  is determined by coherent bandwidth  $1/\tau_{max}$  and symbol duration  $T$ , and pilot spacing in time domain  $N_t$  is determined by the maximum Doppler spread  $B_{D_{max}}$  and symbol

duration  $T$  plus guard interval  $T_g$ :

$$N_f < \frac{T}{\tau_{\max}}, \quad N_t < \frac{1}{(T + T_g) B_{D_{\max}}} \quad (5.10)$$

## 5.4. Simulation

### 5.4.1. System Specification

System specification for the simulation is shown in Table I. Assume that bandwidth is 8000 Hz, the maximum Doppler spread is 0.5 Hz, and the maximum delay spread is 50 ms (i.e., minimum coherent bandwidth is about 20Hz). Since the symbol duration is the inverse of sub-carrier bandwidth, one can determine either the symbol duration or the sub-carrier bandwidth first. Sub-carrier bandwidth is determined by coherent bandwidth and Doppler spread as shown in Table I. Considering frequency selective fading, narrower sub-carrier bandwidth is preferable, but for larger Doppler spreading, shorter symbol duration or wider sub-carrier bandwidth is required. Similarly, the symbol duration is determined by both coherent bandwidth (i.e., inverse of delay spread) and Doppler spread. As shown in Table I, the symbol duration has to be larger than the delay spread and smaller than the coherent time (inverse of the Doppler spread). Since QPSK modulation is used, one sub-carrier has two bits; so one OFDM symbol bears 4096 bits. Using the two formulas in (5.10), the minimum pilot spacing in frequency domain for our system is 5.12, and that in time domain is 6.53. We chose 3 for both of  $N_f$  and  $N_t$ , so the density of pilots is 1/9.

Table 5.1 System specification

PARAMETER	RELATIONSHIP	VALUE
Transmission Frequency Band		8000-16000Hz
Signal Bandwidth	$BW$	8000 Hz
Maximum Doppler Spread	$B_{Dmax}$	0.5Hz at 16000Hz
Maximum Delay Spread	$\tau_{max}$	50 ms
Coherent Bandwidth	$B_c = 1/\tau_{max}$	20 Hz
Number of Subcarriers: $N$		2048
(Such that $B_c \gg B_s \gg B_{Dmax}$ )	$B_s = B/N$	(20 >> 3.90625 >> 0.5)
Sub-Carrier Bandwidth		3.90625 Hz
Guard Interval:	$T_g$	50 ms ( $\tau_{max} \leq T_g$ )
Symbol Duration:	$T$	256 ms ( $1/B_s$ )
( $1/B_{Dmax} \gg T \gg T_g$ )		(1560 >> 256 >> 50)
Symbol Rate	$R_s = 1/(T_g + T)$	3.27 symbols/sec
Number of Bits per Subcarrier	$N_b$	2 (QPSK Modulation)
Equalization		2×1D MMSE
Pilot Spacing	Frequency Domain: $N_f$ Time Domian: $N_t$	3 3
Pilot Rate	$R_p = 1/(N_f \times N_t)$	1/9
Bit Rate: $R = (1 - R_p) \times R_s \times N \times N_b$		11898.3 bps
Bandwidth Efficiency:	$\eta = R/B$	1.49

### 5.4.2. Channel Simulator

An underwater channel simulator was developed, which can simulate the Doppler and multipath effects for broadband signals. Path delay  $\tau_p(m)$  is composed of 2 components:

$$\tau_p(m) = \Delta_p m + \tau'_p(m) \quad (5.11)$$

$\Delta_p$  is the delay increasing (or decreasing) rate which generate Doppler shift, and is determined by relative velocity of transmitter and receiver.  $\tau'_p(m)$  is a stochastic process which simulates irregular motions of sea surface, transmitter and receiver, and other factors

affecting propagation delay. Its mean value is determined by average sound velocity and path length between transmitter and receiver. It is controlled to generate proper Doppler spectrum and delay spread. Path gain  $\alpha_p(m)$  is a random process whose mean value is determined by the channel impulse response.

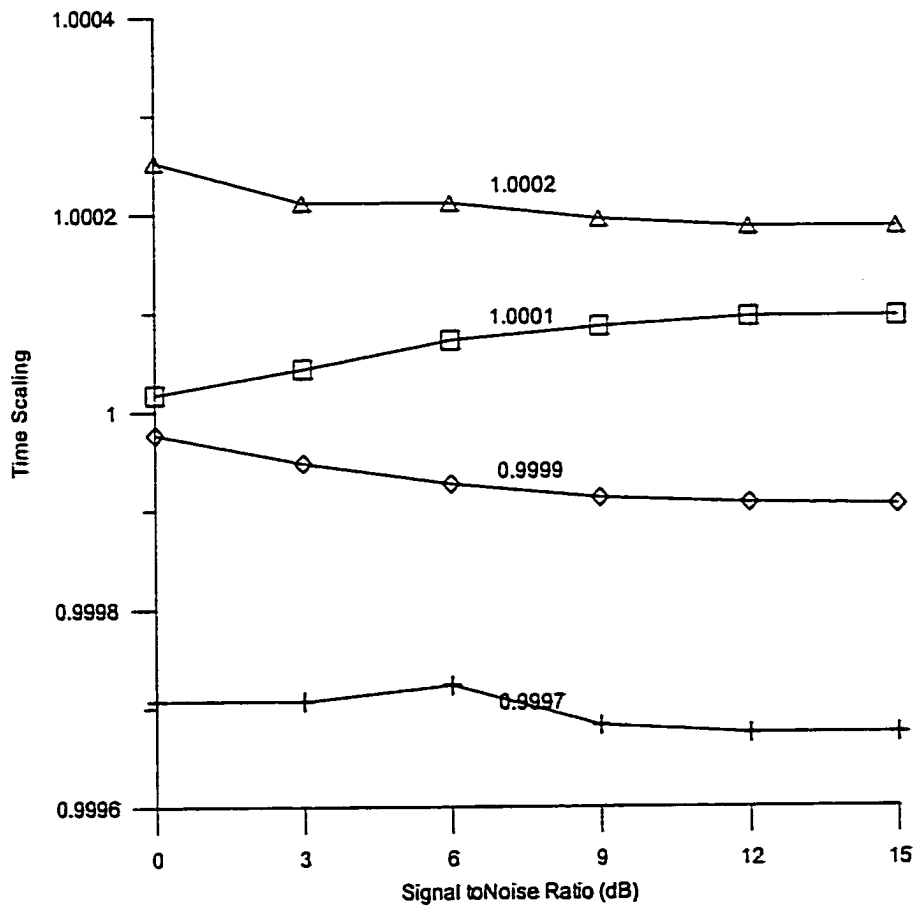


**Figure 5.2** Doppler shift estimation for simulated signal



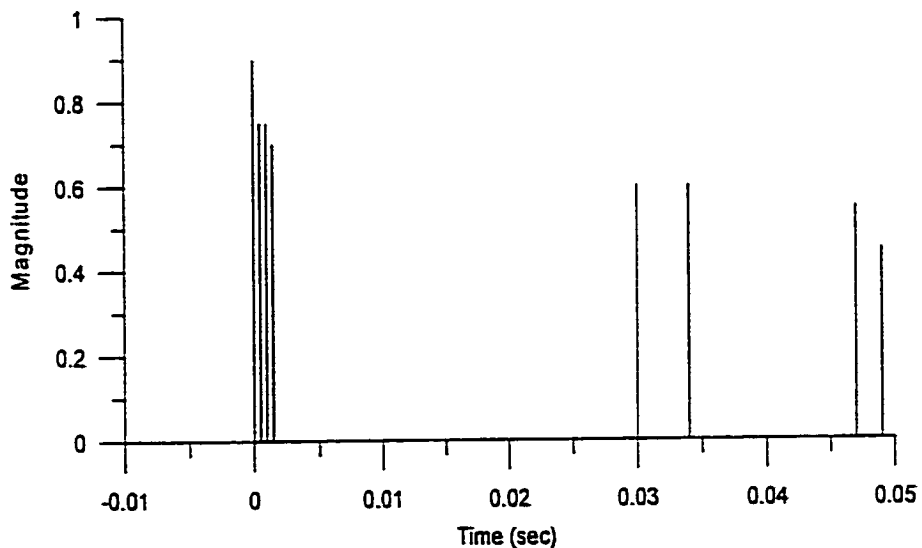
### 5.4.3. Doppler Shift Estimation

Figure 5.2 shows estimated values of time scaling factor caused by Doppler shift. Four examples are calculated. Actual values are 0.9997, 0.9999, 1.0001 and 1.0002. All values are averages of 9 consecutive estimates for the same signal to noise ratio.

### 5.4.4. BER Performance

For BER simulation, a 8-ray model was used, which is based on the prediction model and measured results appeared in [7]. The impulse response of the channel is shown in Figure 5.3. Note that the magnitude and time-delay are continuously varying in time to generate Doppler shift and spread.

Uncoded bit error rate versus S/N is shown in Figure 5.4 for 3 different Doppler spreads. For the worst case, Doppler shift of 0.04% (4 Hz at 10 kHz or 6.4Hz at 16kHz) is estimated



**Figure 5.3** Channel Impulse Response for Simulation

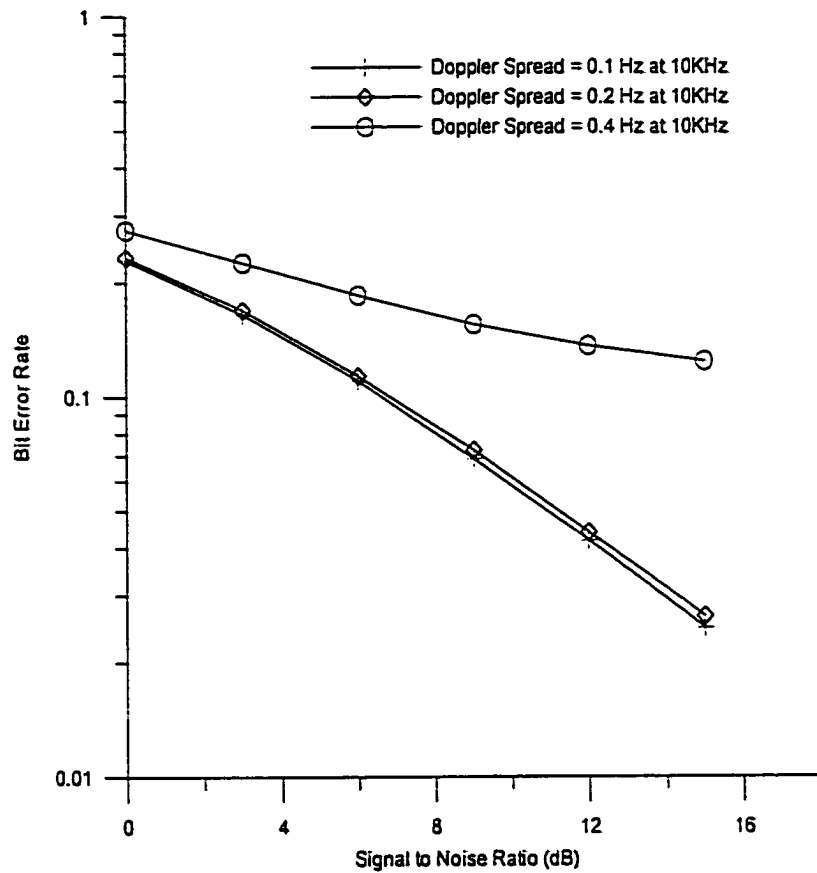


**Figure 5.4** BER versus signal to noise ratio

using cyclic prefix, and compensated by the re-sampling process. Interleaving and convolutional coding can be used to spread information in the frequency domain to combat frequency selective fading. Multi-Carrier CDMA is the other option for combating the frequency selectivity.

## 5.5. Conclusion

Design criteria and analysis procedures of practical OFDM systems are shown. A new channel simulator is developed to generate ultra broadband underwater channel responses that are used in numerical simulations. In our approach, inter symbol interference caused by delay spread is removed by the insertion of cyclic prefix. Furthermore, Doppler shift is compensated effectively using the proposed re-sampling procedure, which is preceded by the frequency shift estimation using cyclic prefix. The  $2 \times 1D$  MMSE channel estimator makes full use of the correlation of channel frequency response at different times and frequencies. The presented OFDM approach is a very robust communication technique to time and frequency selectivity when the product of Doppler spread ( $B_{D_{\max}}$ ) and symbol period ( $T+T_g$ ) is less than 0.20. When  $B_{D_{\max}} \times (T+T_g) > 0.2$ , time domain receiving techniques need to be employed to take advantages of the large delay spread and time variation feature. This work will be published elsewhere.

## References

- [1] W. K. Lam and R. F. Ormondroyd, "A novel broadband COFDM modulation scheme for robust communication over the underwater acoustic channel," Proc. IEEE Oceans '98, vol. 2, pp. 794-799, September 1998.
- [2] John A. C. Bingham, "Multicarrier modulation for data transmission: an idea whose time has come," IEEE Communications Magazine, 28(5):5-14, May 1990.
- [3] Bayan, S. Sharif, Jeff Neasham, Oliver R. Hinton, and Alan E. Adams, "Computationally efficient Doppler compensation system for underwater acoustic communications," IEEE J. Oceanic Eng., vol 25, No.1, pp. 52-61, January 2000.
- [4] Jan-Jaap van de Beek, Magnus Sandell, Per Ola B\*ryjesson, "ML estimation of time and frequency offset in OFDM systems," IEEE Trans. Signal Processing, vol.45, No. 7 pp. 1800-1805, July 1997.
- [5] J. G. Proakis and D. G. Manolakis, Digital Signal Processing – Principles, Algorithms and Applications, 3rd ed., Englewood Cliffs, NJ: Prentice-Hall, 1996.
- [6] Peter Hoehner, Stefan Kaiser and Patric Robertson, "Two-dimensional pilot-symbol-aided channel estimation by wiener filtering," in Proc. IEEE ICASSP '97, vol. 3, pp. 1845-1848, April 1997.
- [7] Vincent K. McDonald, Joseph A. Rice, Michael B. Porter, Paul A. Baxley, "Performance measurements of a diverse collection of underwater acoustic communication signals," Proc. IEEE Oceans '99, vol. 2, pp. 1002-1008, September 1999.

## Chapter 6

### Field Trials of OFDM Underwater Communications in SignalEx-C and SignalEx-D

#### 6.1. Introduction

Underwater acoustic (UWA) channels are very hostile for high-rate data communication systems. Time-varying multipath propagation with wide delay-spreads causes frequency selective fading (time dispersion) and frequency shift and spread (frequency dispersion). In order to combat frequency selectivity while maintaining high data rates, multicarrier transmission schemes such as Orthogonal Frequency Division Multiplexing (OFDM) can be employed. In OFDM, multiple subcarriers with very narrow bandwidth are transmitted in parallel so that each subcarrier can experience flat, non-frequency selective fading. The subcarriers are chosen to be orthogonal to each other so that they can be packed closely to increase the spectral efficiency. However, as the symbol duration increases, the subcarrier spacing decreases and the effects of frequency dispersion becomes profound. If the frequency dispersion becomes so severe that the orthogonality among subcarriers is shattered, the OFDM system performance will degrade drastically. Because of this reason, previous works on OFDM in UWA requires the spacing of adjacent subcarriers to be greater than  $2/T$ , which is twice of the minimum spacing  $1/T$ , where  $T$  is the symbol duration.

In this study, in order to overcome frequency dispersion and to obtain maximum spectral

efficiency with  $1/T$  subcarrier spacing, we separate frequency shifts and frequency spreads and treat them individually. This separation is justified by the fact that the differences of reception angles in UWA channels are relatively small for typical operating conditions. Therefore, the mean value of frequency dispersion is regarded as frequency shift and the deviation from the mean value is frequency spread.

The mean frequency shift can be estimated using cyclic prefix, which is inherently built in typical OFDM signaling. The estimation scheme is based on that frequency shift is caused by compression or expansion of the transmitted waveform by Doppler effect. Thus, by estimating the time scaling (dilation) factor, one can approximate the mean frequency shift. In fact, this time scaling factor can be used to compensate the frequency shift. In this study, the time scaling factor is estimated from the change of time lag between cyclic prefix and its replica in the symbol at receiver. Using the estimates of time scaling factor, received signal is resampled to compensate frequency shift. After compensating the frequency shift, channel estimation and equalization are performed to deal with Doppler spread. Channel estimation, assisted by pilot symbols, is based on the pilots along frequency and time axis.

In this chapter, we concentrate on the sea trial results. The U.S. Navy has embarked on a systematic program called Signal-Ex, for comparing modem performances of various communication systems and relating these performances to practical underwater acoustic propagation conditions. The experiments involve participation from a large number of institutions, whose waveforms are transmitted and received through a pair of common teleonar testbeds. The 'Teleonar testbeds' are compact units consisting of a Pentium II computer, a projector, a 4-hydrophone receiver, high-speed DSP units, and Benthos ATM885 modems. The testbed can digitize and store multichannel acoustic data sampled at 48 kHz in

real-time [1]. We transmit two OFDM signals with minimum frequency spacing ( $1/T$ ) in two Signal-Ex experiments. The received signals are analyzed here to validate of our approach and to show its performance in practical UWA environments.

## 6.2. Signal Ex-C

Signal Ex-C, the 3<sup>rd</sup> Signal Ex experiment, was performed at a shallow water site west of Point Loma, CA, USA, from the 23<sup>rd</sup> to the 25<sup>th</sup> in May 2000. One of two teleonar testbeds is deployed on the bottom of about 200 m depth. The other was deployed at fixed positions with distance of 3, 5, and 7 km. Details on the experimental environment including the sound speed profile and the channel impulse response can be found in [2-4].

### 6.2.1. Source Signal Specifications

Signal specifications used for this experiment are shown in Table 6.1. How each parameter is designed is explained in details in the following:

#### A. *FORMAT*

In practical applications, coding is usually required to reduce bit error rate (BER) on the expense of data rate reduction. Therefore, the signaling scheme we designed for the experiment is coded orthogonal frequency division multiplexing (COFDM). However, the BER results shown in this chapter are for the uncoded OFDM signaling because the improvement of BER of coded systems over that of uncoded systems are well known. The signal spectrum has been shown in Figure 4.8.

Table 6.1 Signal Specifications for Signal Ex-C

PARAMETER	ABBREVIATION	VALUE
Transmission Frequency Band	$(BW)$	8000-11000Hz
Format		COFDM
Symbol Duration	$T$	0.256 Sec
Cyclic Prefix Length	$T_g$	0.092 Sec
Subcarrier Spacing	$1/T$	3.91 Hz (1/0.256)
Total Number of Subcarriers	$N$	768 (3kHz/3.91Hz)
Number of Data Subcarriers	$K_d$	620 (768-63-67-18)
Number of Pilot Subcarriers	$K_p$	63
Number of Dummy Subcarriers	$K_m$	67
Number of Reference Subcarriers		18
Number of Bits per Subcarrier	$N_b$	2 (QPSK)
Number of Transmitted Symbols		22
Number of Data Bits Transmitted		26040
Effective Data Rate		3563 bps
Equalizer Length		10 (time axis), 24 (frequency axis)

### B. SYMBOL DURATION AND SUBCARRIER SPACING

The symbol sequence on time axis is shown in Figure 6.1. The symbol duration should be long enough to combat frequency selectivity of the channel caused by the long delay spread, while keeping the phase variation in a symbol due to Doppler effects as small as possible. Before the experiment, the maximum delay-spread of the channel was predicted to be 90 ms to 110 ms (the coherence bandwidth would be about 9 to 11 Hz) by propagation model, and

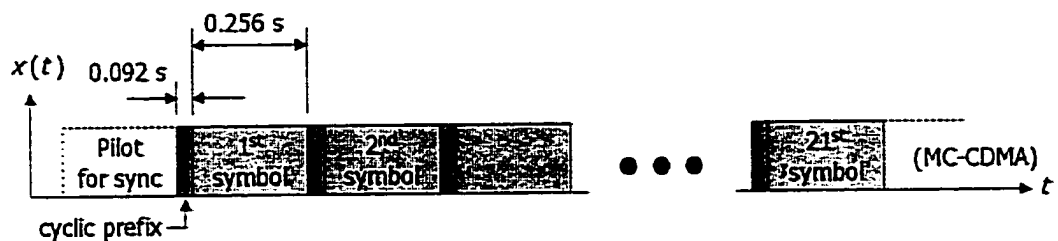


Figure 6.1 Symbol sequence on time axis



Doppler spread was expected to be 0.5 to 1Hz. In order to keep phase variation in a symbol less than  $\pi/2$  (or  $F_D T$  of 0.25; this absolute number could be obtained from previous simulation in [8]), symbol duration should be less than 0.25 sec. This value, 0.25 sec, is acceptable because it limits the minimum subcarrier spacing to 4 Hz and is twice smaller than coherence bandwidth. However, considering sampling frequency of the recorder (48 kHz), the available bandwidth (3 kHz) and the FFT size (1024) for matched filtering, 0.256 second was finally chosen and the subcarrier spacing is 3.91Hz.

### *C. CYCLIC PREFIX LENGTH*

The length of the cyclic prefix was determined by the maximum path-delay predicted by the propagation model. Considering the sampling rate in baseband and the predicted delay spread of channel, which is about 90 ms to 110 ms, the length of the cyclic prefix was chosen to be 92 ms.

### *D. TOTAL NUMBER OF SUBCARRIERS*

Since the subcarrier spacing was chosen to be 1/0.256 Hz, and the bandwidth of 3 kHz was already given, the total number of carriers becomes  $N = BW \times T = 3000 \times 0.256 = 768$ .

### *E. DATA AND PILOT SUBSYMBOLS, DUMMY AND REFERENCE CARRIERS*

In the receiver, channel estimation for every subsymbol is performed before equalization. We employ MMSE frequency-time 2×1D pilot-symbol aided channel estimation [5-7] in this study. The pilot-subsymbol grid used in the receiver processing is shown in Figure 6.2 where  $N_f$  is the pilot spacing along the frequency (subcarrier) axis and  $N_t$  is the pilot spacing along the time (symbol) axis. In our system,  $N_f = 4$  and  $N_t = 3$ . This is constrained by the maximum delay spread and the maximum Doppler spread of channel.

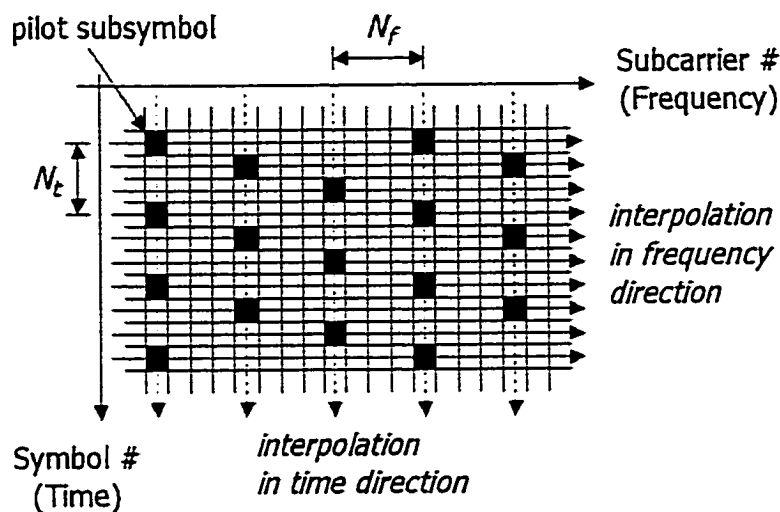


Figure 6.2 Pilot-Subsymbol Grid

In addition to the original COFDM data or pilot subsymbols, we insert 4 reference time-harmonic tones into our symbol. These 4 tones occupy 18 subcarrier spaces and are for analysis purpose, such as examination of Doppler spectrum (see chapter 4). Alignment of subsymbols and reference tones are illustrated in Figure 6.3. Let  $\lceil x \rceil$  denote the smallest integer which is greater than or equal to  $x$ . Therefore,

$$\begin{aligned} & \text{the number of pilot subcarriers in the } 1^{\text{st}} (4^{\text{th}}, 7^{\text{th}}, \dots) \text{ row in Figure 6.2 is} \\ & \lceil (\text{number of subcarriers} - \text{number of subcarriers occupied by the reference tones}) / N_f \rceil, \\ & = \lceil (768 - 18) / 12 \rceil = 63, \end{aligned}$$

Moreover, when a FIR type MMSE estimator is used, channel estimates for the leftmost and rightmost  $(N_f - 1) \times (L_f / 2 - 1)$  subcarriers cannot be obtained, where  $L_f$  is the FIR filter length. Since  $L_f$  in our system is 24, there are at least  $(4 - 1) \times (24 / 2 - 1) = 33$  dummy subsymbols in each side of the spectrum. These dummy subcarriers could not be used to carry data. In our design, taking the pilot subcarriers into consideration, the number of dummy subcarriers becomes

$$2 \times (N_f - 1) \times (L_f / 2 - 1) + \text{remainder}((\text{total number of subcarriers} - \text{number of subcarriers occupied by reference tones} - 1) / N_f) = 66 + \text{remainder}((768 - 18 - 1) / 12) = 67.$$

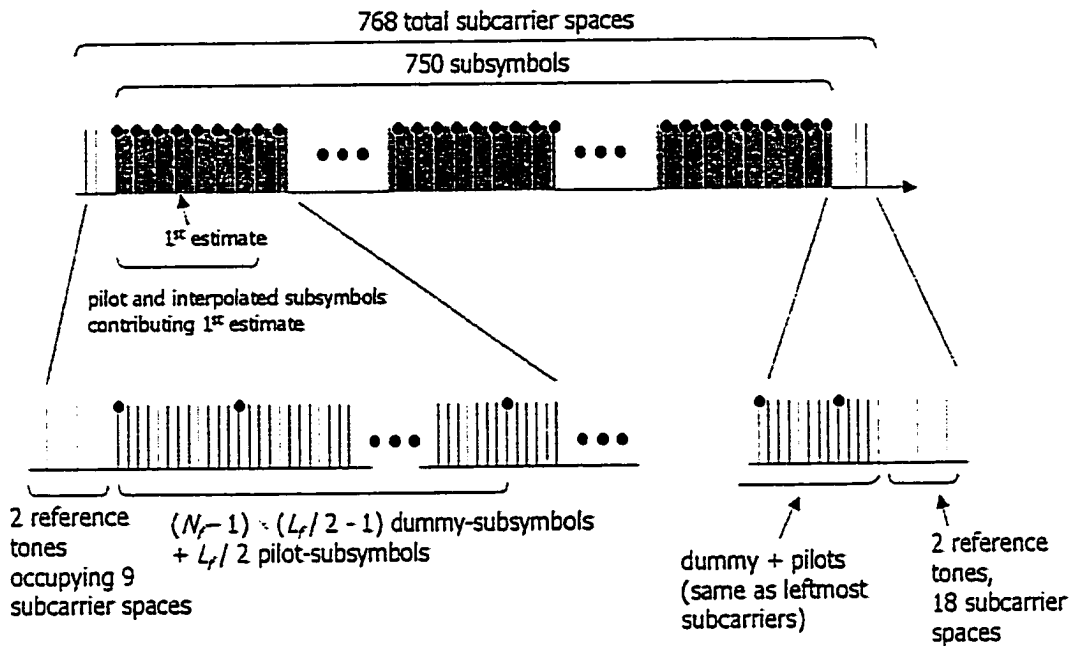


**Figure 6.3** Symbols and reference tones

#### F. NUMBER OF BITS PER SUBCARRIER

Each subcarrier is QPSK (Quadrature Phase-shift Keying) modulated. Therefore, a subcarrier contains two bits of data.

#### G. TOTAL NUMBER OF SYMBOLS

For this analysis, the first symbol (all subcarriers are pilots) was used for synchronization and the remaining 21 symbols contain both data and pilot subcarriers.

#### H. NUMBER OF DATA BITS TRANSMITTED

Total number of data bits transmitted = number of bits per subcarriers  $\times$  number of data subcarriers per symbol  $\times$  total number of symbols transmitted  
 $= 2 \times 620 \times 21 = 26040$

#### I. EFFECTIVE DATA RATE

data bit rate = number of bits per subcarriers  $\times$  number of data subcarriers per symbol  
 $/ (\text{symbol duration} + \text{cyclic prefix}) = 2 \times 620 / (0.256 + 0.092) = 3563 \text{ (bps)}$

## 6.2.2. Received Signals Processing

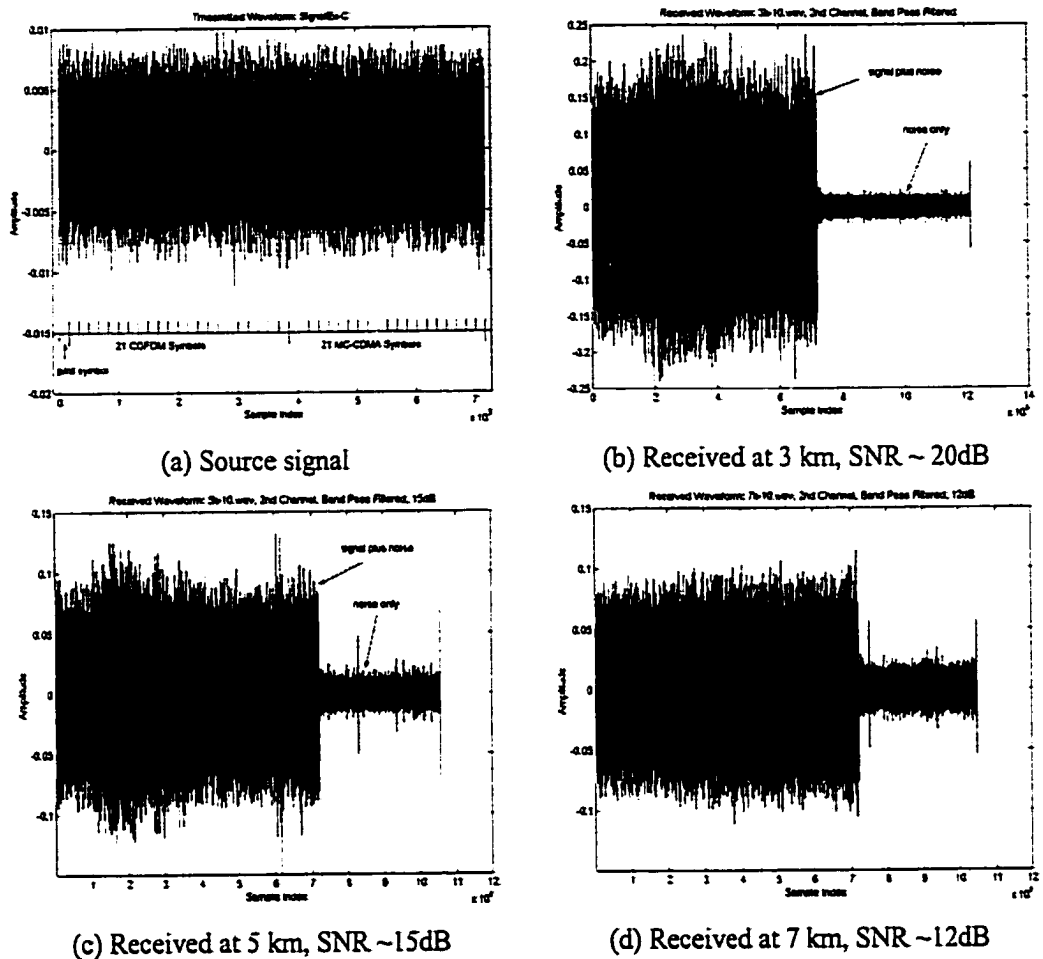


**Figure 6.4** Source and received signal at various distances

The ranges between source and receivers are 3 km, 5 km and 7 km. Source and receiver are stationary. Waveforms of source and typical received signals at these three ranges are shown in Figure 6.4. Signal to noise ratio is approximated by the ratio of the variance of signal plus noise samples and the variance of noise only samples. Signal processing block diagrams for source generation and for receiver processing are shown in Figure 5.1.

### 6.2.2.1. Doppler shift estimation and compensation

The primary shortcoming of OFDM is intercarrier interference induced by Doppler shift and spread, which may destroy the orthogonality among subcarriers. In underwater communications, Doppler spread is not large because of small angle spreads in most practical situations. However, Doppler shift can be very large when the platform is moving. This is due to the fact that sound speed is not much larger the speed of platform. In a moving platform system, if the Doppler shift is uncompensated, the intercarrier interference can grow out of control. In the proposed system, Doppler shift is estimated by measuring the time scaling factor of the received waveform and the time scaling factor is computed using the time lag between the cyclic prefix and its replica in the received symbol [8]. Since SignalEx-C is performed with fixed geometry, the mean Doppler shift is almost 0. The estimated instantaneous frequency scaling factor is shown in Figure 6.5. Compensation of Doppler shift was done by a re-sampling procedure (interpolation/decimation) in the discrete time domain.

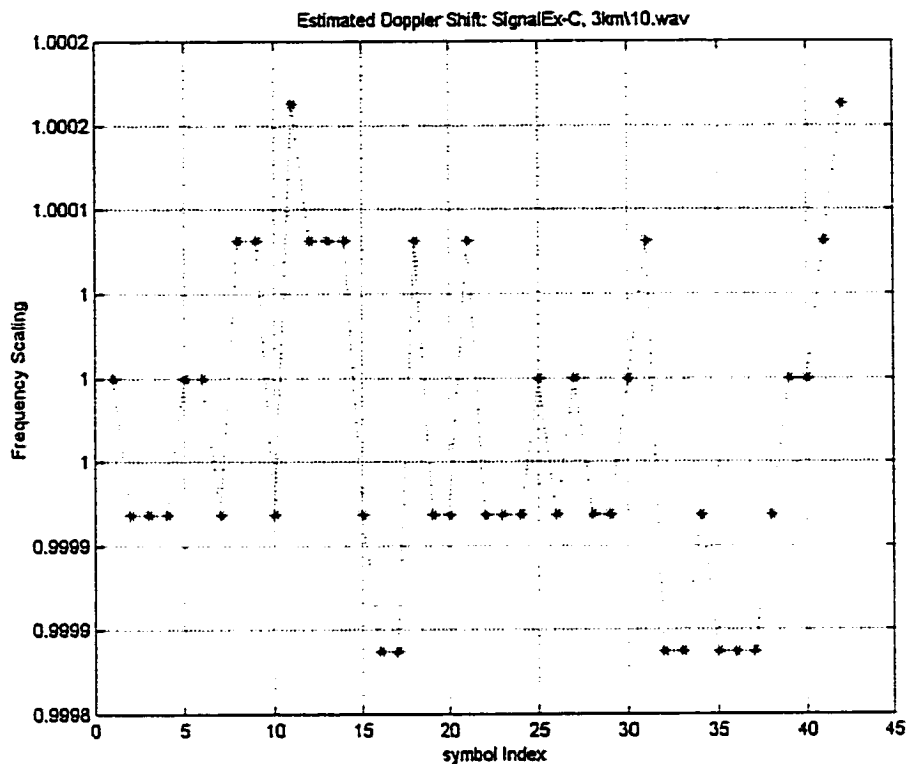


Figure 6.5 Symbol by symbol estimation of Doppler shift for a signal received at 3 km

### 6.2.2.2. Channel Estimation and Delay Profile Estimation

In order to equalize both time and frequency dispersions of the received signals, two-dimensional time-frequency pilot-symbol aided MMSE channel estimation and equalization are employed. The estimated magnitude responses for subcarriers are plotted in Figure 6.6-9. In Figure 6.6 and Figure 6.7, channel responses are estimated from 4 consecutive symbols received at 3 km, and Figure 6.9 and 6.10 are at 7 km. Delay profiles are estimated using cross correlation between the transmitted and received waveforms. The delay profile is used to estimate pdf of the path delay, which is required in MMSE channel estimation.

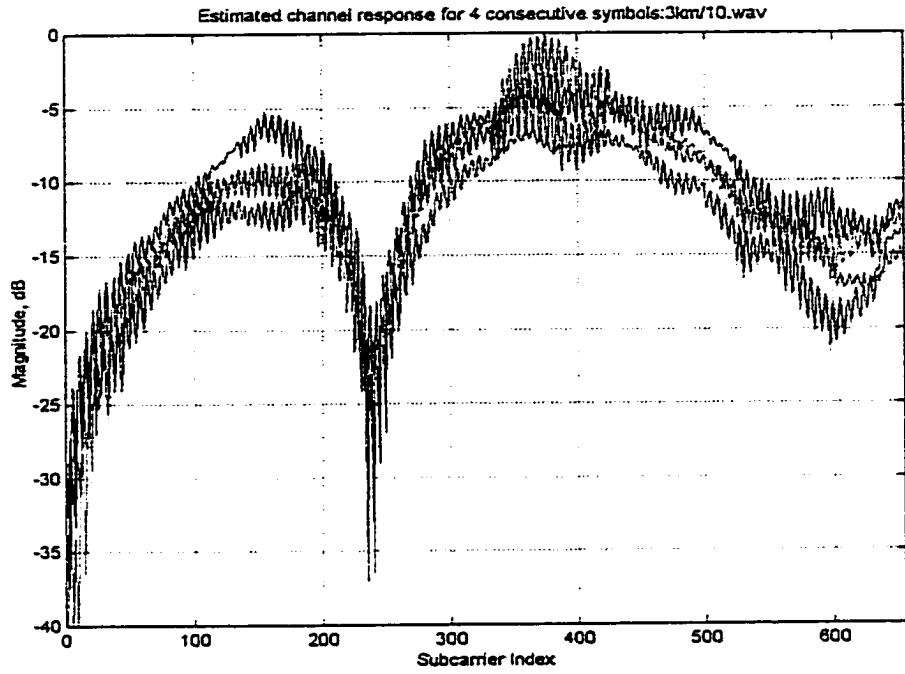


Figure 6.6 Channel frequency response for 3 km

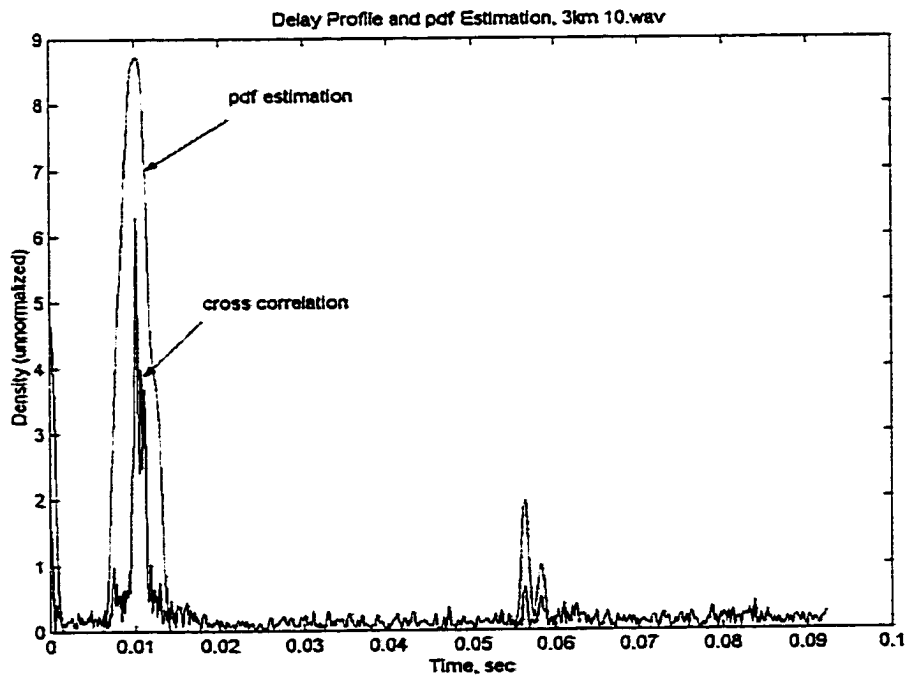


Figure 6.7 Delay profile for 3 km

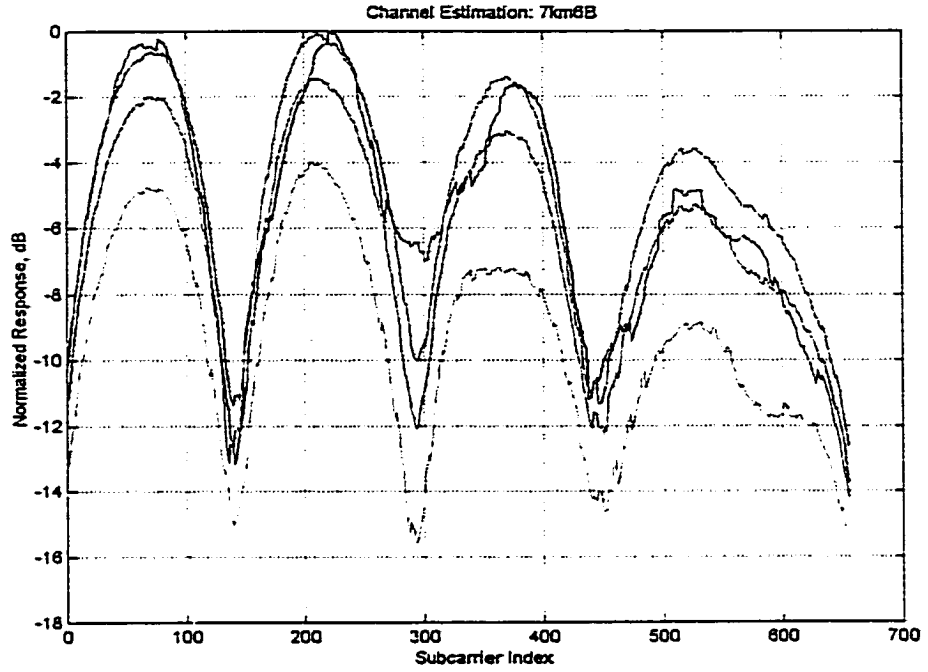


Figure 6.8 Channel frequency response for 7 km

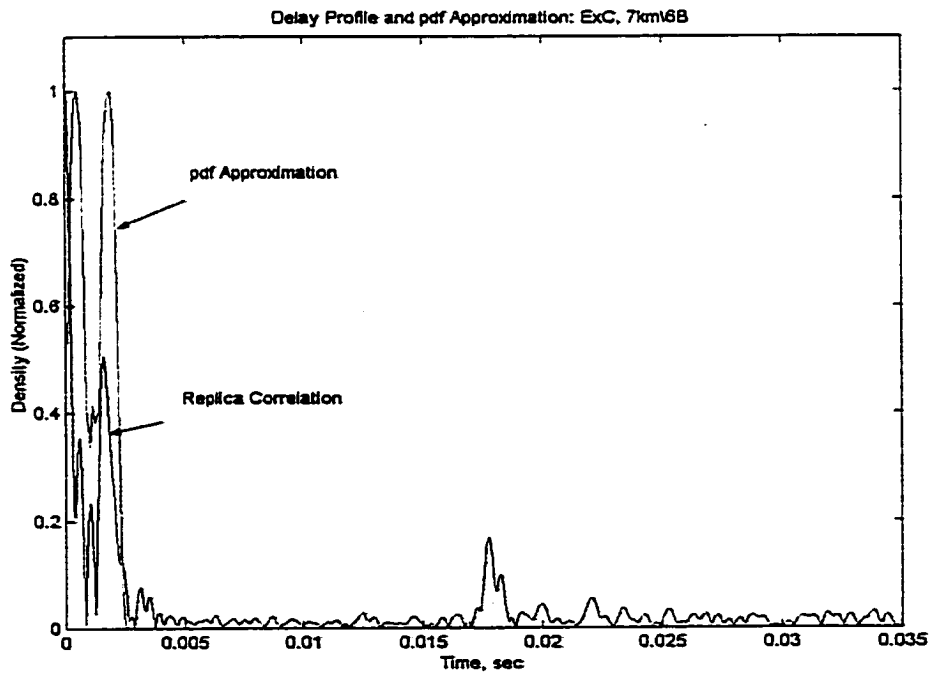


Figure 6.9 Delay profile for 7 km



Figures 6.6 and 6.8 show deep fades at some subcarriers in the middle of the frequency spectrum. Closely examining Figures 6.6 and 6.7 or Figures 6.8 and 6.9, it is not difficult to find the correlations between the fade patterns and the delay separation. It seems that small ripples in Figure 6.6 are due to the interference of the first arrival (arriving at 0.011sec) and the 3<sup>rd</sup> arrival (arriving at 0.055sec) in Figure 6.7. This is because the delay separation between the first and the 3<sup>rd</sup> arrivals is about 50 ms, and the frequency spacing between small ripples in the magnitude response in Figure 6.6 is about 20 Hz (1/50msec). Moreover, the strength of the 3<sup>rd</sup> arrival is much weaker than that of the first arrival. Therefore, the magnitude of interfering ripples is small. Similarly, the frequency separation of the first and second deep fades in Figure 6.6 is around 800Hz, and the delay separation of the first and second arrivals in Figure 6.7 is around 1.2msec ( $\approx 1/800\text{Hz}$ ). The magnitude response (shown in Figure 6.8) and the delay profile (in Figure 6.9) also have such relationships. The two peaks in Figure 6.9 generate the fade pattern in figure 6.9.

### **6.2.2.3. Constellation of Subsymbols after Equalization**

Constellations of equalized subsymbols received at 3km, 5km, and 7km are shown in Figures 6.10-12, and their corresponding average SNR's are about 20 dB, 15dB and 12 dB, respectively. It seems that there were high but slow Doppler shift fluctuations, especially for the cases in Figure 6.10 and Figure 6.12 where the constellations of consecutive symbols rotated. Since the number of total symbols is only 21, our channel estimation approach cannot provide accurate estimation of these Doppler shift fluctuations. Therefore, these constellation rotations are not completely compensated.

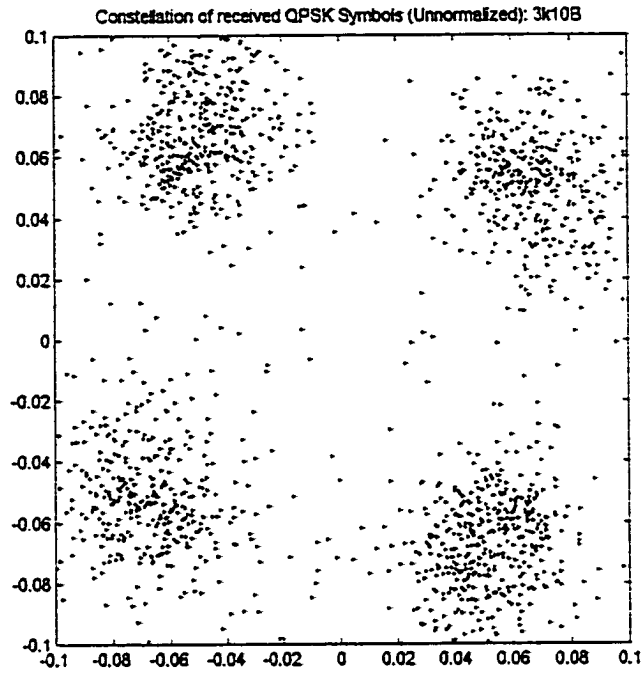


Figure 6.10 Constellation of equalized subsymbols: 3 km,  $S/N \approx 20\text{dB}$

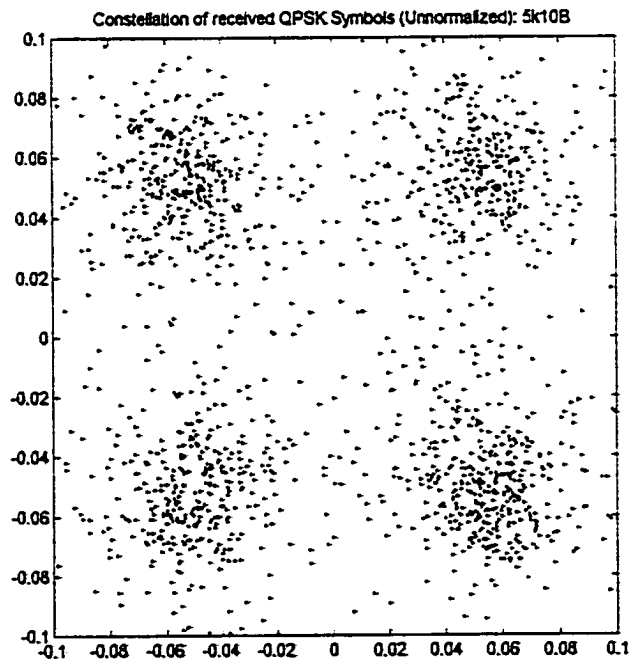


Figure 6.11 Constellation of equalized subsymbols: 5 km, about 15 dB

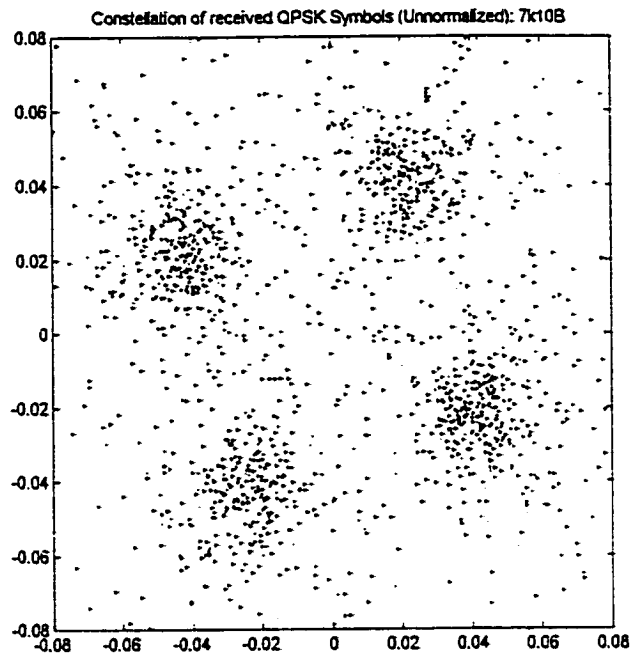
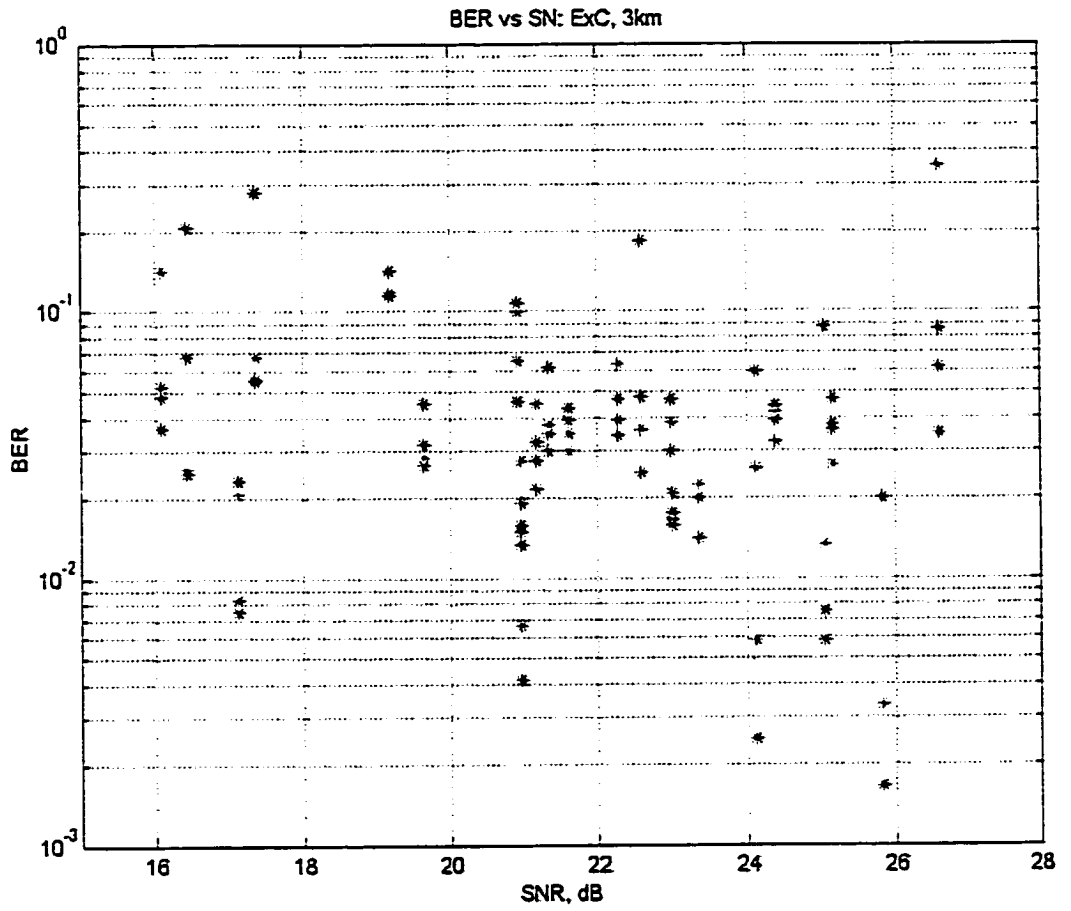


Figure 6.12 Constellation of equalized subsymbols: 7km, about 12 dB

#### 6.2.2.4. Bit Error Rate

BER of subsymbols plotted in Figures 6.10-12 are shown in Figures 6.13-15, respectively. Note that all of these estimates are undecoded, raw-bit error rates. In Figure 6.13, BER's are scattered. Symbols with higher SNR do not show better BER performances. This is caused by inaccurate channel estimation (and hence incomplete equalization) due to the lack of available symbols per records. In Figure 6.14, the BER's are also scattered, but BER's decrease as SNR increases. However, poor BER's for some symbols with SNR higher than 22 dB are observed. In Figure 6.15, BER's decrease as SNR increase. Note that subsymbols with BER's higher than 0.5 should be discarded.



**Figure 6.13** BER of symbols for the 3 km data

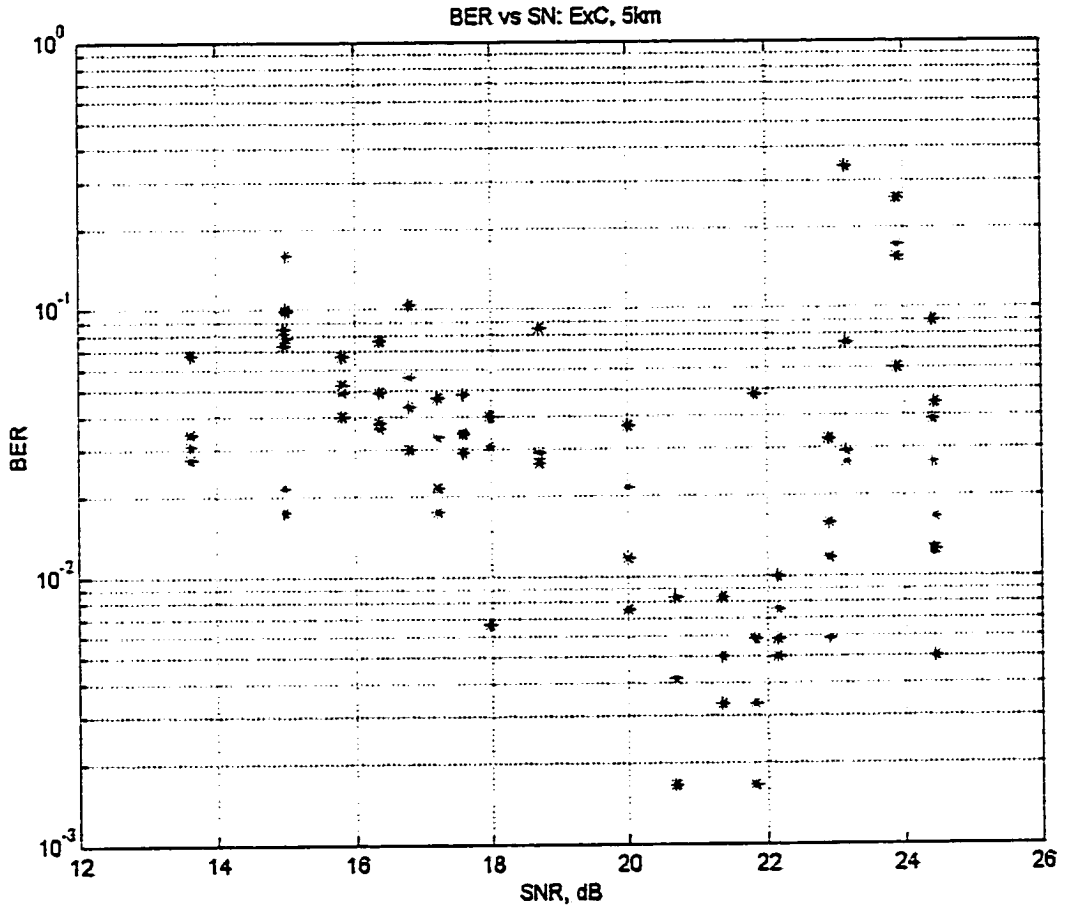


Figure 6.14 BER of symbols for the 5 km data



### 6.3. Signal Ex-D

Signal Ex-D, the 4<sup>th</sup> Signal Ex experiment, was performed at Buzzard Bay, MA, USA, from the 10<sup>th</sup> to the 11<sup>th</sup> in August 2000. Details on the experimental environment including the sound speed profile and the channel impulse response can be found in [9].

#### 6.3.1. Source Signal Specifications

Signal specifications used for SignalEx-D are summarized in Table 6.2.

**Table 6.2** Signal Specifications for SignalEx-D

Item	Specification
Frequency Band	8 kHz – 11 kHz
Format	COFDM
Symbol Duration	0.256 Sec
Cyclic Prefix	0.1 Sec
Subcarrier Spacing	3.91 Hz (1/0.256)
Total Number of Subcarrier Spaces	768
Number of Data Subsymbols	638 (83% of total subcarriers)
Number of Pilot Subsymbols	64
Number of Dummy Carriers	66
Number of Reference Tones	0
Number of Bits per Subsymbol	2 (QPSK)
Number of Symbols	74
Number of Data Bits Transmitted	94424
Effective Data Rate	3584 bps
Length of Equalizer	22 (time axis), 24 (frequency axis)

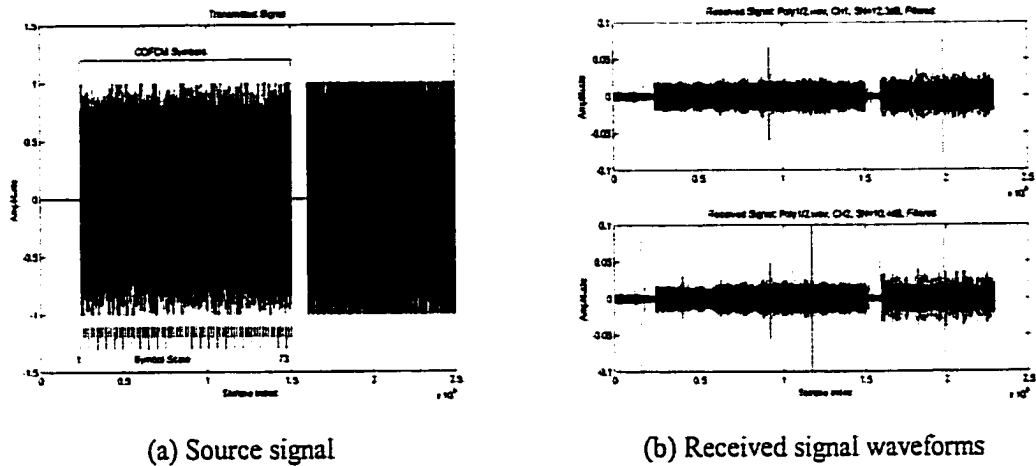


**Figure 6.16** Source and received waveforms

Except reference tones, the signaling structure for SignalEx-D is similar to that for SignalEx-C. Note that there is no reference tone in the source signal for SignalEx-D. Waveforms of source and typical received signals are shown in Figure 6.16. Note that, in SignalEx-D, there exists impulsive noise as shown in Figure 6.16b.

### 6.3.2. Receiver Signal Processing

Receive signal processing for SignalEx-D is the same as that for SignalEx-C. 30 records in total are available, but only 13 of them were analyzed. In this experiment, the sensor was not fixed, but drifting.

#### 6.3.2.1. Doppler Shift Estimation and Compensation

Because the sensor was drifting in Signal Ex-D, estimation and compensation of Doppler shift is very crucial. Our proposed method is proven to yield good results. Typical results are shown in Figure 6.17.



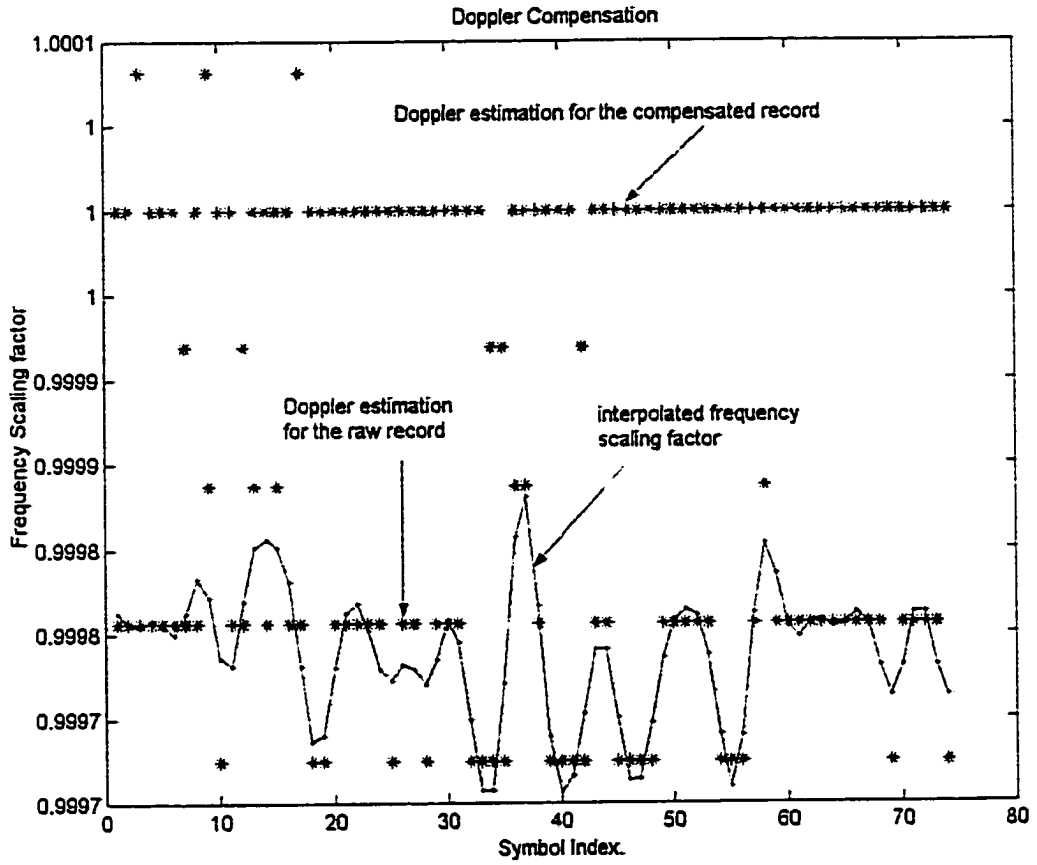
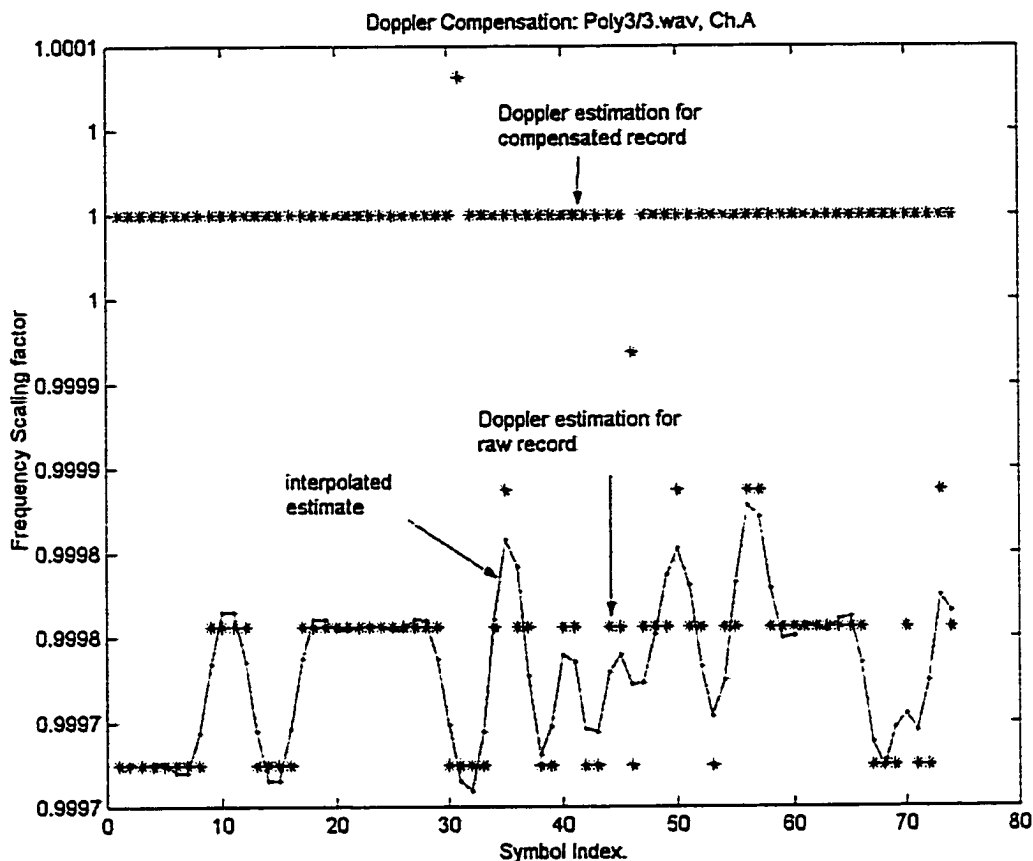


Figure 6.17 Doppler shift estimation and compensation: SNR = 12.3 dB



**Figure 6.18** Doppler shift estimation and compensation: SNR = 14.6 dB

In Figures 6.17-18, the estimated frequency shifts, before and after frequency-shift compensation, are shown in the lower and upper halves of the corresponding figures, respectively. The symbol-by-symbol frequency scaling factors (marked by '\*' in the lower halves of these two figures) are in the range of 0.9997 – 0.9999. Interpolation was performed after symbol-by-symbol estimation (see the curves in Figures 6.17 & 6.18). Doppler shift compensation was then carried out sample-by-sample using the interpolated values. After compensation, Doppler shifts are estimated again and the results are marked by '\*' in the upper halves of these two figures. 74 OFDM symbols are analyzed for each figure. Most of the Doppler shifts are compensated except 8 symbols in Fig. 6.17 and 2 symbols in Fig. 6.18.

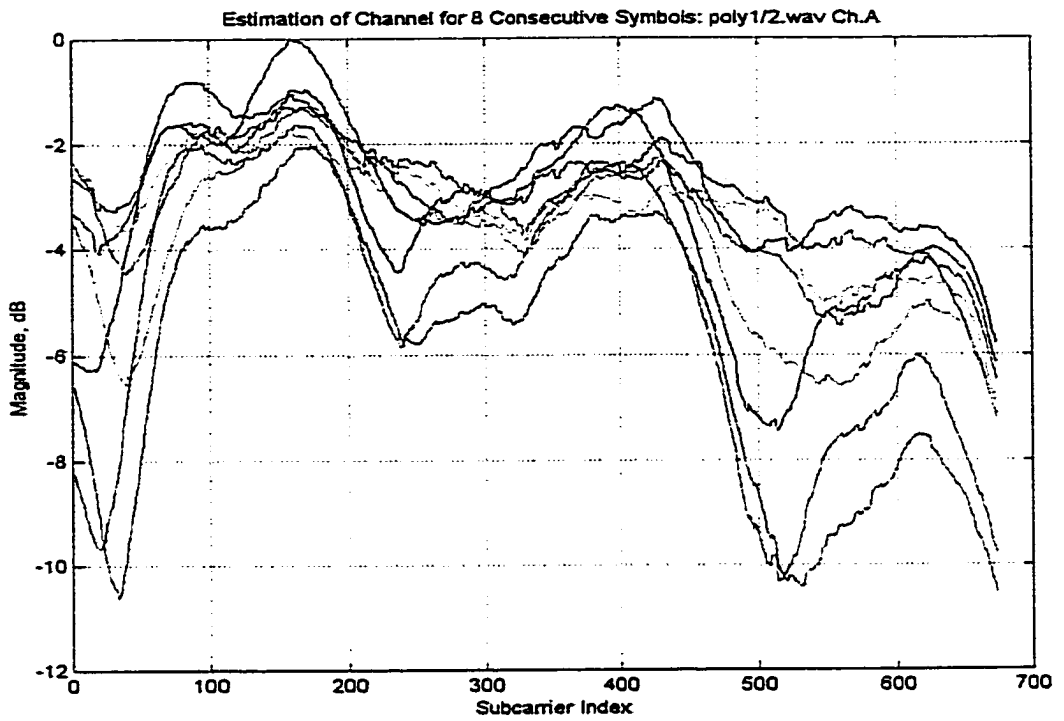


Figure 6.19 Channel frequency response: SNR=12.3dB

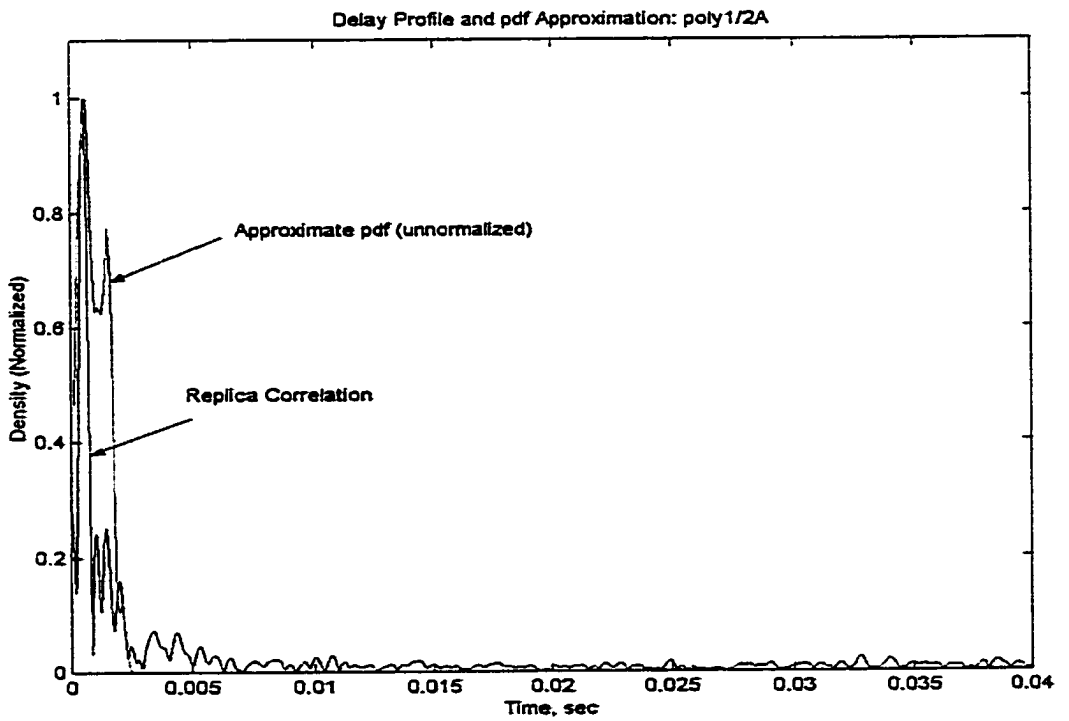


Figure 6.20 Delay profile corresponding to Figure 6.18

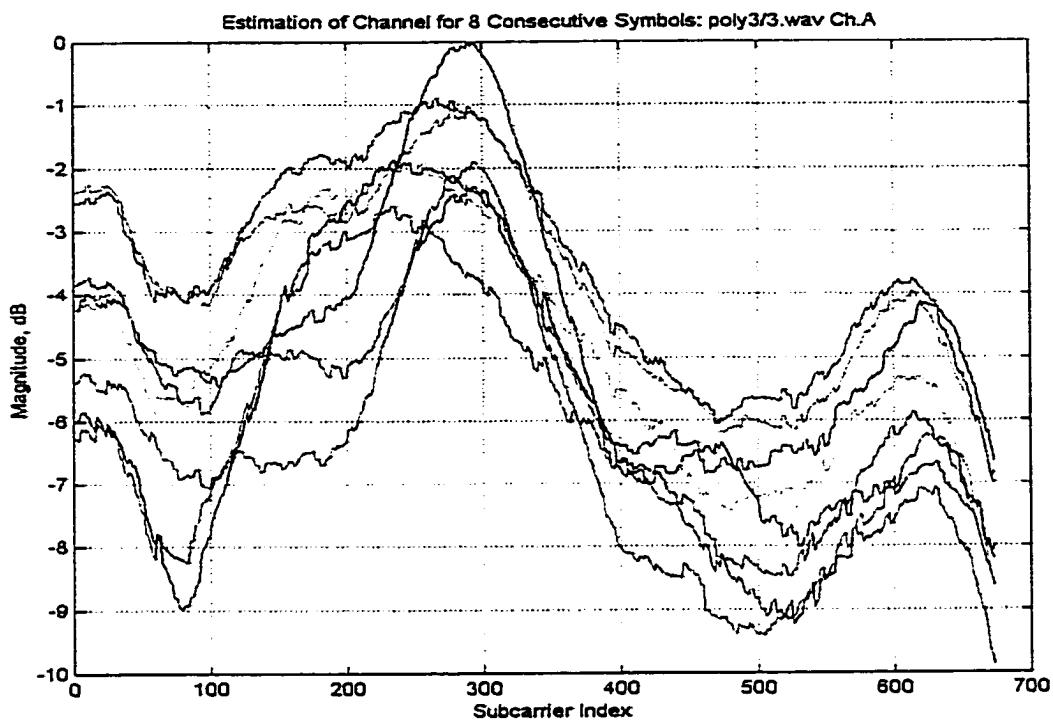


Figure 6.21 Channel frequency response: SNR = 14.6 dB

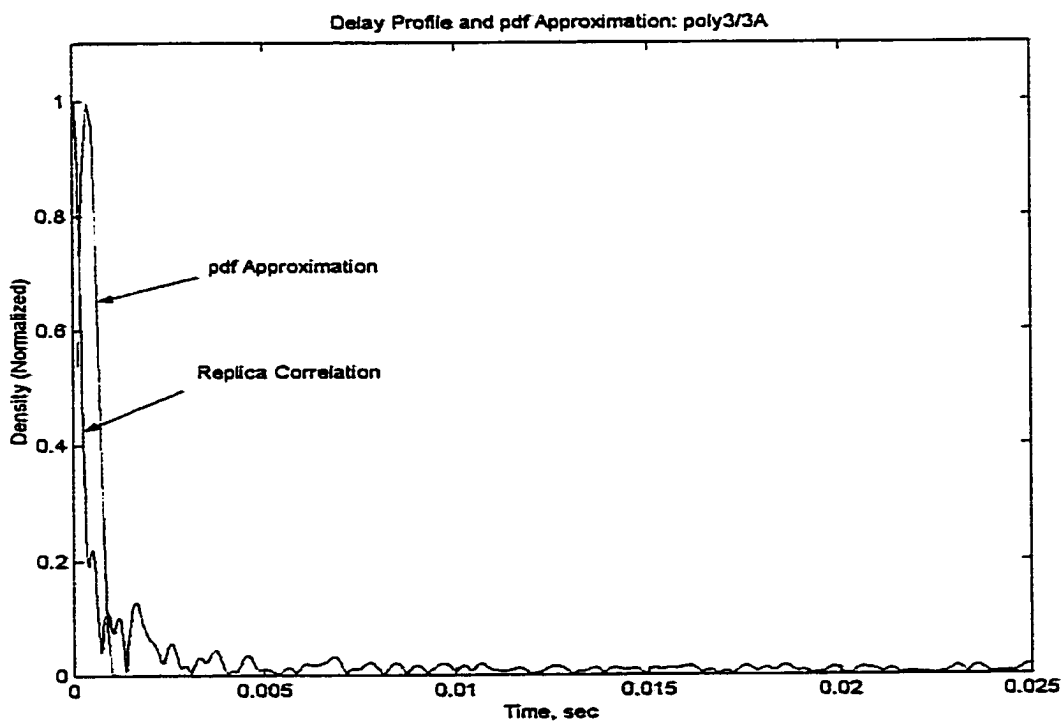


Figure 6.22 Delay profile corresponding to Figure 6.21

### **6.3.2.2. Channel Estimation and Delay Profile Estimation**

The magnitudes of channel frequency responses for subcarriers and delay profiles are shown in Figures 6.19 and 6.20 for SNR=12.3dB and in Figures 6.21 and 6.22 for SNR=14.6dB. Each plot in Figures 6.19 and 6.21 is estimated from 8 consecutive symbols. Frequency selectivity and time variation can be observed in both records. Delay profiles are obtained from the cross correlations between the transmitted and received signals. The delay profiles are used for obtaining MMSE channel estimator.

### **6.3.2.3. Constellation of Subsymbols after Equalization**

Constellations of equalized subsymbols are shown in Figure 6.23-24. Both signals were recorded at 3 km and their corresponding SNR's are about 12 dB and 15dB, respectively. There were significant Doppler shifts in these records because of the platform drifting. The effects of Doppler shifts can be eliminated using our proposed Doppler shift estimation and compensation schemes. Since there are 74 symbols in Ex-D (much more than the 21 symbols in Ex-c), the effects of Doppler spread can be compensated using our frequency-time  $2 \times 1D$  channel estimation and equalization schemes.

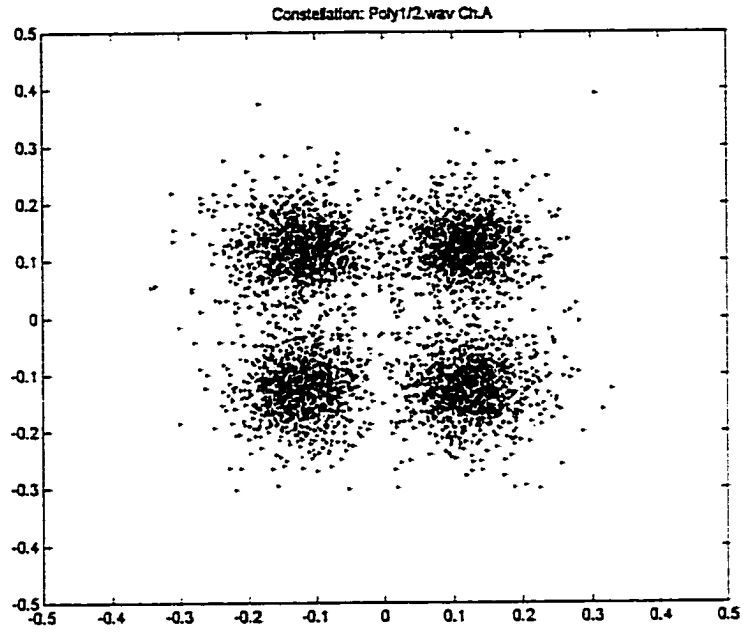


**Figure 6.23** Constellation of subsymbols after equalization 12.3 dB

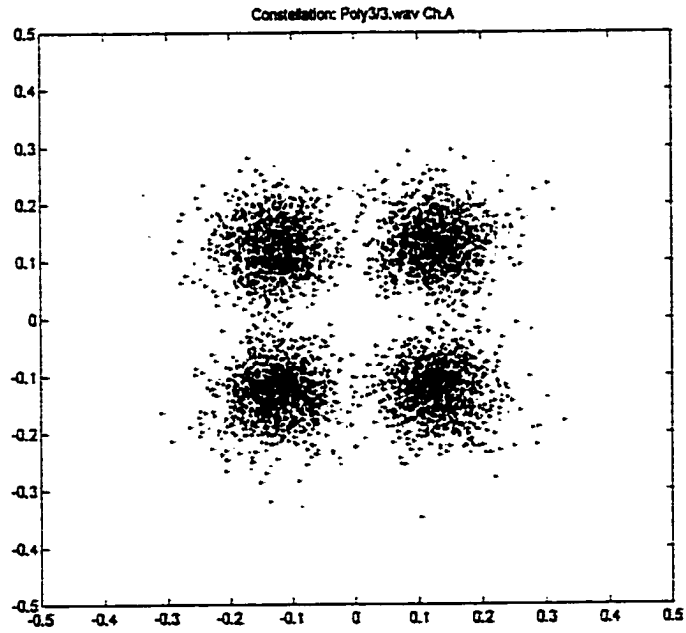


**Figure 6.24** Constellation of subsymbols after equalization: 14.6 dB

### 6.3.2.4. Bit Error Rate

BER for undecoded bits is shown in Figure 6.25. In the figure, BER decreases as SNR increases. Compensation of Doppler shift and time-frequency equalization is essential to UWA OFDM systems.

### 6.3.3. Summary for SignalEx-D

Although the channel shows high frequency selectivity and the sensor geometry was changing constantly, the induced Doppler shift was properly compensated. In addition, time-frequency equalization mitigates degradation caused by Doppler spread. BER results are very

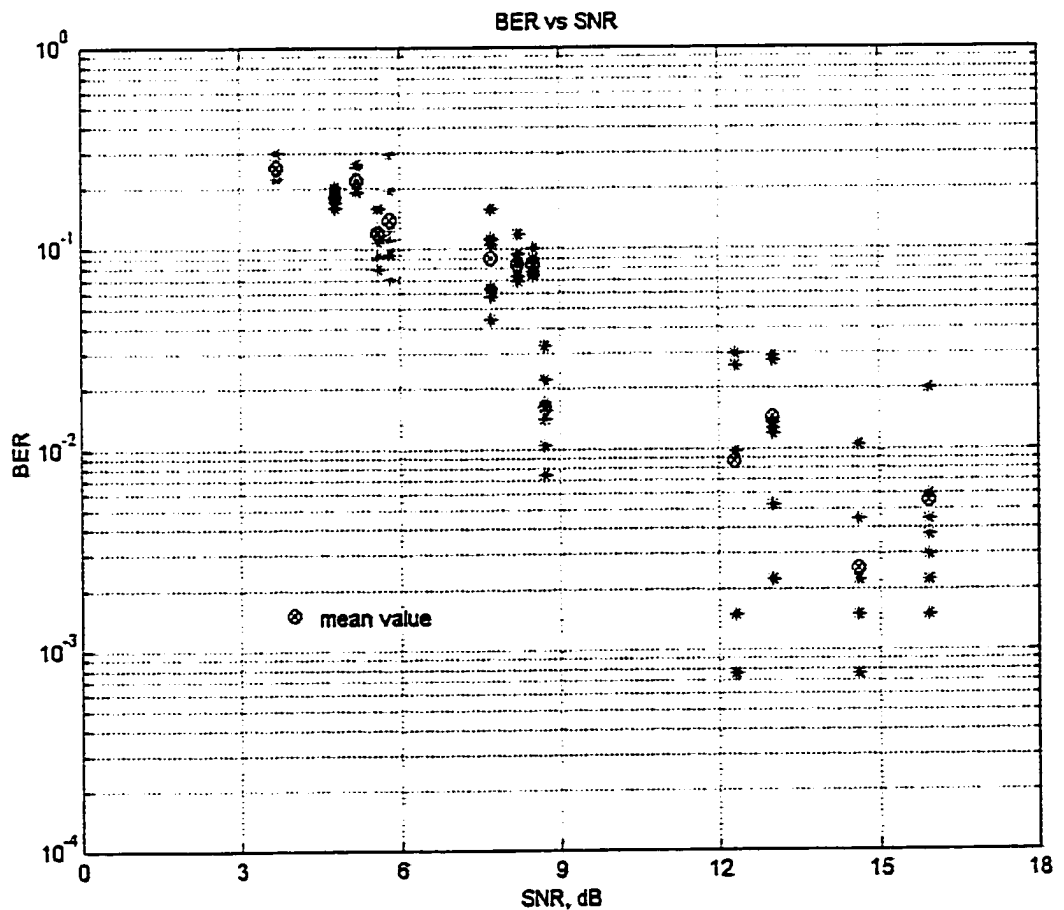


Figure 6.25 BER for undecoded bits for SignalEx-D

encouraging.

#### **6.4. Conclusion**

It was shown that OFDM is a promising signaling scheme for underwater communications through the experiment and analysis. The proposed Doppler shift estimation and compensation schemes enable OFDM underwater communications (with minimum subcarrier spacing of  $1/T$ ) to achieve BER below 1 % when SNR is higher than or equal to 15 dB. If these techniques are combined with the Doppler diversity processing, discussed in chapter 2 and 3, the underwater data communications using OFDM will be much more improved.



## References

- [1] Vincent K. McDonald, Joseph A. Rice and Chris L. Fletcher, "An underwater communication testbed for teleonar RDT&E," *Proc. IEEE OCEANS '98*, vol. 2, pp. 639–643, 1998.
- [2] Michael B. Porter, Vincent K. McDonald, Paul A. Baxley and Joseph A. Rice, "SignalEx: linking environmental acoustics with the signaling schemes," *Proc. MTS/IEEE OCEANS 2000*, vol.1, pp. 595–600, September 2000.
- [3] Vincent K. McDonald, Joseph A. Rice, Michael B. Porter and Paul A. Baxley, "Performance measurements of a diverse collection of undersea acoustic communications signals," *Proc. IEEE Oceans '99*, vol. 2, pp. 1002–1008, 1999.
- [4] J. Rice, B. Creber, C. Fletcher, P. Baxley, K. Rogers, K. McDonald, D. Rees, M. Wolf, S. Merriam, R. Mehio, J. Proakis, K. Scussel, D. Porta, J. Baker, J. Hardiman, D. Green, "Evolution of Seaweb underwater acoustic networking," *Proc. MTS/IEEE OCEANS 2000*, vol.3, pp. 2007–2017, September 2000.
- [5] Peter Hoehner, Stefan Kaiser and Patric Robertson, "Two-dimensional pilot-symbol-aided channel estimation by wiener filtering," in *Proc. IEEE ICASSP '97*, vol. 3, pp. 1845-1848, April 1997.
- [6] Ye Li, "Pilot-symbol-aided channel estimation for OFDM in wireless systems," *IEEE Trans. on Vehicular Technology*, vol. 49 No. 4, pp. 1207–1215, July 2000.
- [7] Rickard Nilsson, Ove Edfors, Magnus Sandell and Per Ola Borjesson, "An analysis of two-dimensional pilot-symbol assisted modulation for OFDM," *Proc. IEEE International Conference on Personal Wireless Communications*, pp. 71–74, 1997

- [8] Byung-Chul Kim and I-Tai Lu, "Parameter studies of OFDM underwater communications systems," in Proc. MTS/IEEE Oceans 2000, vol.2 pp. 1251-1255, Sept. 2000.
- [9] Report on SignalEx-D will be published in the near future.